POLITECNICO DI TORINO

I Facoltà di Ingegneria

Corso di Laurea in Ingegneria Aerospaziale

Tesi di Laurea Magistrale

Analisi dei flussi turbolenti attraverso la teoria delle reti complesse. Applicazione alla turbolenza omogenea isotropa

A complex network approach for the analysis of turbulent flows. Application to homogeneous isotropic turbulence.

Relatore:
Dott. Stefania Scarsoglio

Candidato:
Giuseppe Barletta

Luglio 2014

Ringraziamenti

Innanzitutto ringrazio sentitamente la professoressa Scarsoglio per il tempo dedicatomi e per avermi seguito e consigliato durante l'intero lavoro svolto: la prontezza e la precisione nei suoi interventi hanno facilitato di gran lunga il mio lavoro.

Ringrazio i miei genitori che mi sono stati sempre vicini (per fortuna non troppo!) e che mi hanno sempre sostenuto in tutte le mie decisioni. Vi voglio bene, so quanto conta questo obiettivo per voi. Per me è importantissimo rendervi felici.
Un grazie a tutti i miei parenti, specialmente alle nonne, che hanno sempre creduto in me e che mi hanno rivolto un pensiero costante nonostante la lontananza.

Maria Luisa meriterebbe un capitolo a parte! Mi sopporti (o il contrario?) in maniera costante da tanto tempo e sai benissimo che hai giocato un ruolo fondamentale in tutto ciò. Non smetterò mai di ringraziarti, sei vitale per me.

Un ultimo pensiero va a tutti i miei amici di questi 6 anni; nominarvi tutti richiederebbe un po' troppe pagine. Vi dico solo che siete stati parte importante della mia vita sino ad ora, e spero che il nostro rapporto possa durare nel tempo!

Sommario

La turbolenza è una fenomenologia comune che è presente sia in diversi fenomeni naturali come le correnti oceaniche o atmosferiche che in una ampia varietà di campi industriali o ambientali come, ad esempio, la climatologia, le reazioni chimiche, l'industria aerospaziale e la biologia.
Nonostante costituisca oggetto di studio da secoli, grazie al contributo incessante di teorie o tecniche numeriche e sperimentali, ci sono ancora parecchi aspetti inesplorati riguardanti la caratterizzazione spaziale, la predizione e il controllo della turbolenza: questa costituisce un sistema fortemente complesso a causa del suo comportamento che è random, irregolare e instazionario. La turbolenza, infatti, è non prevedibile dettagliatamente.
Ad oggi, diverse simulazioni numeriche e sperimentali sono condotte in maniera simultanea, con lo scopo di conseguire una descrizione migliore della dinamica della turbolenza. Esperimenti di laboratorio come la "grid turbulence" o simulazioni numeriche delle equazioni di Navier-Stokes come DNS, LES e RANS, sono state effettuate in maniera fruttuosa per decadi, lasciando contestualmente il campo aperto a diversi e nuovi approcci.
Questo lavoro è pensato come un approccio preliminare all'analisi di un flusso turbolento tramite metodo delle reti complesse, con l'obiettivo di ottenere una migliore comprensione della caratterizzazione spaziale e superare le limitazioni della teoria statistica classica.
La teoria delle reti complesse affonda le sue radici nella teoria dei grafi e nella fisica statistica, e costituisce un potente strumento per l'analisi di sistemi complessi formati da un grande numero di elementi che evolvono dinamicamente nel tempo. Questa teoria è stata usata con successo in diversi campi, come ad esempio sociologia, biologia, economia o informatica, mentre più recente è l'interesse della comunità di ingegneri o di climatologi. La teoria delle reti complesse è ancora oggi una teoria giovane e che continua ad espandersi, ottenendo in maniera continuativa contributi da diverse comunità di ricercatori provenienti da differenti campi di studio.
In questo lavoro ci focalizziamo sull'analisi di un campo di turbolenza forzata e isotropa, che fa parte di un database open-access di simulazioni DNS (il Johns Hopkins Turbulence Database). Dopo un'analisi preliminare svolta con i classici

strumenti tipici della dinamica della turbolenza (autocorrelazioni, funzioni di struttura e spettri di energia), cercheremo di applicare le principali definizioni e proprietà della teoria delle reti complesse.
L'obiettivo di questa analisi è quello di arricchire e contestualmente sintetizzare le informazioni provenienti dalla nascita e dalla evoluzione spaziale delle strutture presenti in un campo turbolento. Si tenga in considerazione il fatto che questa teoria viene applicata per la prima volta in uno studio di caratterizzazione di un flusso turbolento, quindi questo lavoro può essere considerato originale nel proprio campo.
La tesi è organizzata in questa maniera: nel capitolo 1 verranno sintetizzati i concetti base della turbolenza e verrà prestata particolare attenzione alla teoria di Kolmogorov e alle definizioni degli strumenti classici utilizzati per la descrizione statistica del flusso.
Nel secondo capitolo, invece, saranno riportate brevemente la storia e le proprietà della DNS insieme ad una descrizione sintetica dei metodi risolutivi alternativi come LES e RANS. Alla fine di questo capitolo sarà introdotto il database scelto per l'analisi, con qualche cenno alla fase di pre-processing.
Nel capitolo 3, verrà presentata la teoria delle reti complesse: qui verrà fornita una breve descrizione della storia e dell'evoluzione della teoria e dei suoi campi di applicazione. Dopo di ciò, saranno introdotte le definizioni analitiche e i parametri utilizzati in fase di analisi. Alla fine del capitolo verrà rivolta grande attenzione alla fase di costruzione della rete.
Il capitolo 4 costituirà il corpo principale di questa tesi e sarà diviso in due parti: la prima conterrà i risultati dell'analisi effettuata tramite i metodi statistici classici della dinamica della turbolenza, volta alla validazione del database scelto, mentre la seconda parte riguarderà l'analisi svolta tramite metodo delle reti complesse.
Il capitolo 5, infine, conterrà una sintesi delle principali proprietà e informazioni ottenute grazie al nostro lavoro, e contestualmente offrirà spunti per futuri miglioramenti perseguibili nell'affinamento di uno studio di questo genere.
Alla fine della tesi, nelle appendici, verrano mostrati i codici (scritti in linguaggio MatLab) utilizzati per il pre-processing, per l'analisi statistica e per quella con la teoria delle reti complesse.

Contents

List of Figures

Chapter 0

Introduction

Turbulence is a common phenomenology in everyday life that is present in several natural phenomena like oceanic or atmospheric currents while also finding application in a variety of industrial and environmental fields like aerospace, climatology, chemical reactions and biology, among many others.
Even if it has been a subject of study for centuries, thanks to the contribution of a variety of theoretical, numerical and experimental techniques, there are still a lot of questions regarding its characterization, prediction and control: turbulence, in fact, is a highly complex subject due to its behavior that is random, irregular and unsteady. Turbulence, eventually, is unpredictable in detail.
Nowadays, experimental and numerical simulations are conducted simultaneously in order to achieve a better description of the dynamic of turbulence. Laboratory experiments like "grid turbulence" or numerical simulations for the Navier-Stokes equations like DNS, LES or RANS have been successfully carried on for decades, while still leaving the field clear for different approaches.
This work is meant as a preliminary approach to analyze a turbulent flow through the method of the complex networks, trying to provide a better comprehension of the spatial characterization of the dynamic of turbulence and overcome the limitation of the classic statistical theory.
Complex network theory has its roots in the theory of graphs and in the statistical physics, and it is a powerful tool to analyze complex systems consisting of a huge number of elements dynamically evolving in time. This theory has been successfully used in several fields as for example sociology, biology, economics and informatics, while more recent is the interest in engineering and climate dynamics. The study of complex networks is a young and still developing area, gaining nowadays contribution from a variety of communities of researchers coming from different fields of study.
In this work we focus on the analysis of a forced isotropic turbulent field, part of an open-access database of DNS simulations (the Johns Hopkins Turbulence Database).

After a preliminary analysis fulfilled with the typical tools used in turbulence (autocorrelations, structure functions and energy spectra), we try to apply the definitions and properties of the complex network theory to the turbulent field.
The purpose of this analysis is to enrich and summarize the knowledge of the formation and evolution of spatial patterns in a turbulent field. Furthermore, the reader should take into account that the complex network theory, to the best of our knowledge, has never been used for the characterization of a turbulent flow, hence this work is original in its field.
The thesis is organized as follows: in chapter 1 the basics of the turbulence theory are summarized with a focus on the Kolmogorov theory and on the definitions of the classical tools used to provide a statistical description of the flow.
In the second chapter, instead, a review of the history and properties of the Direct Numerical Simulations are given, providing a quick description of alternative resolutions as LES or RANS, too. At the end of the chapter we introduce the database chosen for the analysis and its usage.
In chapter 3, the complex network theory is presented: a brief description of the history and evolution of the theory is provided along with an overview of the fields of applications; after that, the analytical definitions and parameters useful for our work are introduced. A first look at the main tools of the theory is given: degree centrality, weighted average topological distance along with the main concepts of network's theory are introduced here. At the end of this chapter, great attention is given to the process of building the network.
Chapter 4 contains the main part of the project, that is the analysis of the data, and it consists of two parts: the first one contains the results of the classical approach through a statistical description of turbulence, made in order to test the consistency of the dataset with the Kolmogorov theory, while the second one is about the analysis of the field with the method of the complex networks.
Chapter 5, finally, contains a synthesis of the main properties and features that we observed in the work, while also suggesting possible improvements that may be pursued in the future evolution of the application of the complex network theory to turbulence.
At the end of the thesis, in the appendices, the codes (in MatLab language) used in this work are provided. In the Appendix A the pre-processing codes are shown, while in Appendix B the ones used to build the network are provided. Appendix C contains the codes for the statistical approach, whereas in the Appendix D the MatLab scripts used in the main part of the project are shown.

Chapter 1

Basics of turbulence

Most of the flows occurring in nature or in industrial applications are turbulent. Common examples of turbulent flows are blood flow in arteries, lava flow, atmospheric and oceanic currents, the flow through pumps or turbines, and the flow in boat wakes and around aircraft-wing tips. During these observations we immediately understand the nature of a turbulent flow, that is unsteady, irregular, random and chaotic: this means that the motion of every eddy or droplet is unpredictable in detail. This chaotic behavior has been confirmed in a great number of laboratory experiments conducted during the years.
Due to the random nature of the turbulent flow we know that the fluid velocity, as other properties, varies significantly and irregularly in position and time. This problem led in the years to giving a particular attention to the statistical descriptions of the turbulent flow: this kind of description is still widely used as complementary to the DNS simulation.
Statistical approach is achieved by describing the flow in terms of some statistics, the simplest being the mean velocity field $< \mathbf{U}(x,t) >$; thanks to this model a more feasible set of equations is achieved, because statistical fields vary smoothly in position and time.

1.1 Turbulence and its properties: a brief explanation

As previously stated turbulence is a random process in which the flow is space and time dependent with a large number of spatial degrees of freedom. Turbulence is unpredictable in details, whereas statistical properties are reproducible.
The dynamic of turbulence is a process that shows the existence of a large set of scales, the smaller ones living inside the larger ones. The small scales are produced

via vortex stretching from the larger ones: this process goes on incessantly provided that the Reynolds number of the flow is sufficiently high. The larger scales extract energy from the mean flow thanks to the flow instability and transfer it to the smaller scales where it is dissipated by viscous action. The Reynolds number plays an important role in dynamic of turbulence, if it drops too low the cascade can not longer operate. The larger scales, which have a local Reynolds higher than the smaller ones, are dynamically important in the flow because they contain the major part of the turbulent energy, while the smaller scales, especially the smallest ones, show a different behavior thanks to the low Reynolds number: these scales dissipate energy as the viscous stresses act on them.
The size of the large scales is generally determined by the environment of the flow. The fine scales become smaller at larger Reynolds numbers but they are always many order of magnitude larger than the molecular mean free path: that said, we can describe a turbulent flow by continuum approximation, that is necessary for the Navier-Stokes equations because they contain derivatives.
Turbulence is rotational (it has vorticity) and intrinsically three-dimensional. Vorticity is the cause of the vortex stretching, which is the main process that guarantees the existence of the energy cascade from the larger scales to the smaller ones.
Turbulence is more diffusive than a laminar flow because of the presence of eddies of different scales: the consequences of the great diffusivity are that wall and flow shear stresses are much higher than laminar ones, the boundary layer is increased, there is a larger thermal and material transport and lower pressure drag.

1.2 The energy cascade

The concept of the energy cascade was first introduced by Richardson in 1922 [1]. Richardson suggested that the kinetic energy enters the turbulence at the largest scales of motion, and is transferred later to smaller scales by an inviscid process that stops when the smallest scales are reached: here the energy is dissipated by viscous action.
The first contribution that Richardson brought to his theory was that the turbulence is composed of eddies of different size. These eddies are a "turbulent motion" localized within a region of size l, that is at least moderately coherent over this region. A larger eddy can also contain several smaller ones and it is characterized by the lengthscale l_0 which is comparable to the flow scale L, while their characteristic velocity u_0 is of the order of the r.m.s. velocity $u' \equiv \left(\frac{2}{3}k\right)^{1/2}$, which is comparable to U (that is the charateristic velocity of the flow). Thanks to these assumptions the Reynolds number of these eddies $Re_0 \equiv u_0 l_0/\nu$ is large: the effect of viscosity are therefore small and negligible.
The large eddies are unstable and break up, transferring the energy to the smaller

eddies that undergo a similar process. Once the Reynolds number drops too low the eddy motion is stable, the process of the energy cascade stops and molecular viscosity acts to dissipate the kinetic energy.
Dissipation is at the end of the sequence, that means that the rate of dissipation, that is ε, is determined by the first process in the sequence: the transfer of energy from the largest eddies. It can be said that, consistent with the experimental observations, the dissipation rate ε scales as u_0^3/l_0, independent of ν.

1.3 The Kolmogorov's hypotheses

In 1941 Kolmogorov gave a fundamental contribution to the turbulent flow theory, advancing three hypotheses that contributed to explain several questions that still were unanswered.
The most important result discovered by Kolmogorov was the local isotropy of the small scale motions, in contrast with the general anisotropic nature of the large eddies: Kolmogorov supported this hypothesis stating that the directional biases of the large eddies are lost during the process of transferring the energy to smaller eddies. The first Kolmogorov's hypothesis hence states that at sufficiently high Reynolds number, the small-scale turbulent motions are statistically isotropic.
The second Kolmogorov's hypotesis comes directly from the first one: just as every directional information is lost during the cascade, also geometrical information are lost, hence the statistics of small-scale motions are "universal", that means similar in every high Reynolds number turbulent flow (this hypothesis is called "first similarity hypothesis"). This second hypothesis therefore states that in every turbulent flow at sufficiently high Reynolds number, the statistics of small scales have a universal form which is uniquely determined by ν and ε. Given these two parameters the characteristic length, velocity, and time scales of the so called *universal equilibrium range* can be obtained as:

$$\eta \equiv \left(\frac{\nu^3}{\varepsilon}\right)^{1/4}, \tag{1.1}$$

$$u_\eta \equiv (\varepsilon\nu)^{1/4}, \tag{1.2}$$

$$\tau_\eta \equiv \left(\frac{\nu}{\varepsilon}\right)^{1/2}. \tag{1.3}$$

Two identities can be stemmed from these definitions: the first one is that the Reynolds number of the Kolmogorov scales is approximately unitary (that implies, as known, that viscosity effects are much more important than the inertial one), the

second one is that the dissipation rate is given by:

$$\varepsilon = \nu \left(\frac{u_\eta}{\eta} \right)^2 = \frac{\nu}{\tau_\eta^2}. \tag{1.4}$$

Thanks to equations 1.1, 1.2 and 1.3, and considering that $\varepsilon \sim u_0^3/l_0$, a ratio between Kolmogorov scales and larger eddies' ones can be obtained:

$$\frac{\eta}{l_0} \sim Re^{-3/4}, \tag{1.5}$$

$$\frac{u_\eta}{u_0} \sim Re^{-1/4}, \tag{1.6}$$

$$\frac{\tau_\eta}{\tau_0} \sim Re^{-1/2}. \tag{1.7}$$

These ratios describe perfectly the behavior of small and large scales at high Reynolds number, that is the characteristics scales of the Kolmogorov eddies are of many order of magnitude smaller than the one of the largest eddies. As a consequence, there is a range of scales l that is very small compared to l_0, but still large compared to η. It may be supposed that, since the eddies in this range are larger than the Kolmogorov ones, their motion is little affected by viscosity. Hence the third Kolmogorov's hypothesis states that in every turbulent flow at sufficiently high Reynolds number, the statistics of the motions of scale l (where $l_0 \gg l \gg \eta$) have a universal form, uniquely determined by ε. This is the "second similarity hypothesis".
A new lengthscale $l_{DI} \sim 60\eta$ may be introduced, and thanks to this definition we may write the range above in the form $l_{EI} > l > l_{DI}$ (where l_{EI} splits the universal equilibrium range from the energy containing one). This is sketched in figure 1.1.

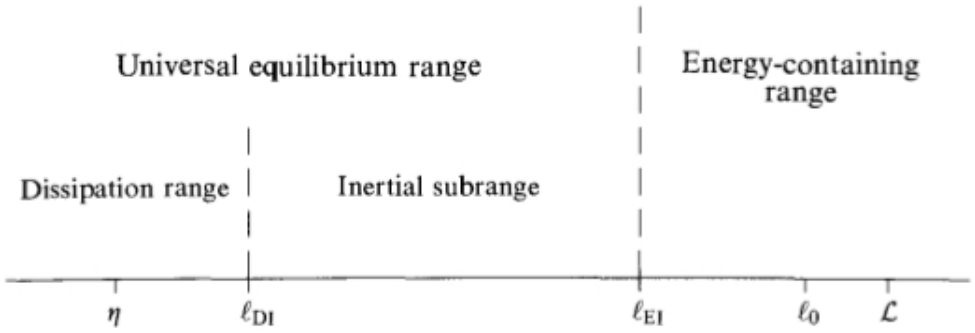

Figure 1.1: Display of the various lengthscales and ranges at a very high Reynolds number

As already said, most of the turbulent kinetic energy is contained in the larger eddies, but we still don't know how it is distributed among the eddies of different size. This study can be performed with an energy spectrum function, just as Kolmogorov did to sustain his theories.
Introducing the wavenumber $\kappa = 2\pi/l$ that corresponds to a motion of a lengthscale l, and considering that the energy in the wavenumber range (κ_a, κ_b) is:

$$k_{(\kappa_a,\kappa_b)} = \int_{\kappa_b}^{\kappa_a} E(\kappa)\, d\kappa, \tag{1.8}$$

where $E(\kappa)$ is the energy spectrum that will be considered in detail later in section 1.4.3, Kolmogorov stated that the energy spectrum in the universal equilibrium range is a function of only ν and ε, while in the inertial range it is:

$$E(\kappa) = C\varepsilon^{2/3}\kappa^{-5/3}, \tag{1.9}$$

with C universal constant for which experimental data support the value $C = 1.5$. This is the so called universal law of Kolmogorov $-\frac{5}{3}$ spectrum. An example of the energy spectrum may be found in figure 1.2, where the $-\frac{5}{3}$ power law stands out for all the energy spectra considered.

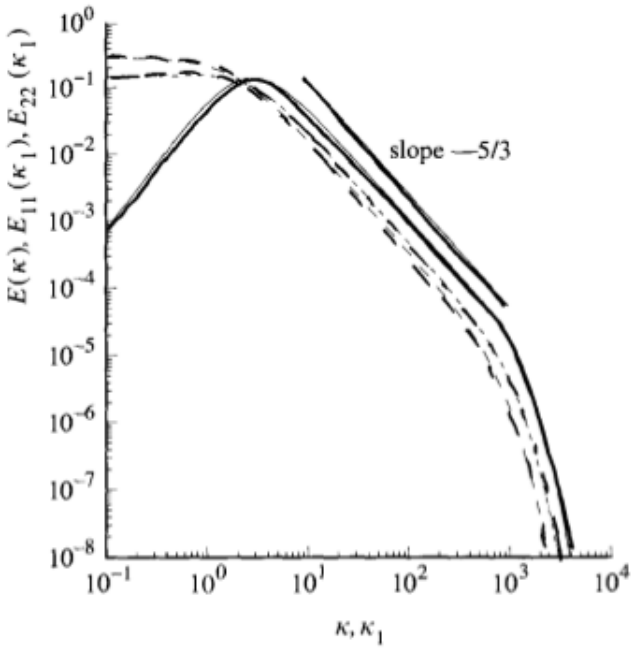

Figure 1.2: Example of Kolmogorov spectrum

1.4 Statistical analysis of turbulent flows

It has already been explained how a statistical description of a turbulent flow may be useful; in this section three of the tools used for the analysis of the present turbulent field are introduced.

1.4.1 Structure functions

As Kolmogorov did back in 1941, we consider the second-order velocity structure function: by definition it is the covariance of the difference in velocity between two points $\mathbf{x}+\mathbf{r}$ and $\mathbf{x}$, that is:

$$D_{ij}(\mathbf{r},\mathbf{x},t) \equiv < [U_i(\mathbf{x}+\mathbf{r},t) - U_i(\mathbf{x},t)]\,[U_j(\mathbf{x}+\mathbf{r},t) - U_j(\mathbf{x},t)] >, \tag{1.10}$$

where the $< ... >$ notation represents an ensemble average.
Applying the Kolmogorov's hypotheses to the above written formula and considering that all the other conditions, including for example the large Reynolds number, are satisfied, we get that $D_{ij}(\mathbf{r},t)$ is an isotropic function of $\mathbf{r}$ [2]. With δ_{ij} and $r_i r_j$ being the only second order tensor formed from vector $\mathbf{r}$, D_{ij} can be written to include D_{LL} and D_{NN}, respectively called longitudinal and transverse structure functions:

$$D_{ij}(\mathbf{r},t) = D_{NN}(r,t)\,\delta ij + [D_{LL}(r,t) - D_{NN}(r,t)]\,\frac{r_i r_j}{r^2}. \tag{1.11}$$

Choosing the coordinate system in a way that $\mathbf{r}$ is in the x_1 direction, it is obtained:

$$D_{11} = D_{LL}, \quad D_{22} = D_{33} = D_{NN} \quad D_{ij} = 0, \quad for\ i \neq j. \tag{1.12}$$

These equations, together with figure 1.3, show the significance of the longitudinal and transverse structure functions.

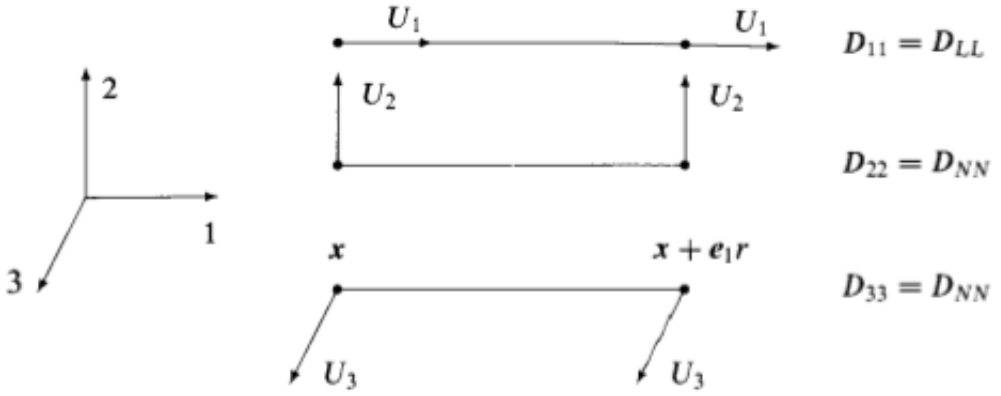

Figure 1.3: Sketch of longitudinal and transverse structure functions for $\mathbf{r} = \mathbf{e}_1 r$

If we now consider a homogeneous turbulence with zero mean velocity, we may write as a consequence of the continuity equation:

$$\frac{\partial}{\partial r_i} D_{ij}(\mathbf{r}, t) = 0, \tag{1.13}$$

equation that applies also to a case of local homogeneity. Thanks to this result equation 1.11 becomes a new one in which the transverse structure function is uniquely determined by the longitudinal one:

$$D_{NN}(r, t) = D_{LL}(r, t) + \frac{1}{2} \frac{\partial}{\partial r} D_{LL}(r, t). \tag{1.14}$$

Then, in isotropic turbulence $D_{ij}(\mathbf{r}, t)$ is determined by the single scalar function $D_{LL}(r, t)$.
Applying the first Kolmogorov similarity hypothesis for $\mathbf{r} \ll L$, D_{ij} is furthermore uniquely determined by the quantities ε and ν; there is a universal non-dimensional function $\hat{D}_{LL}(r/\eta)$ such that

$$D_{LL}(r, t) = (\varepsilon r)^{2/3} \hat{D}_{LL}(r/\eta), \tag{1.15}$$

where the quantity that multiples $\hat{D}_{LL}$ is used to make D_{ij} non-dimensional. Taking into account the second similarity hypothesis, that is the one for large r/η ($L \gg r \gg \eta$), D_{LL} is independent of ν and is given by

$$D_{LL}(r, t) = C_2 (\varepsilon r)^{2/3}, \tag{1.16}$$

where C_2 is a universal constant.
Thanks to the above formula the transverse structure function is:

$$D_{NN}(r, t) = \frac{4}{3} D_{LL}(r, t) = \frac{4}{3} C_2 (\varepsilon r)^{2/3}, \tag{1.17}$$

with D_{ij}:

$$D_{ij}(\mathbf{r}, t) = C_2 (\varepsilon r)^{2/3} \left(\frac{4}{3} \delta_{ij} - \frac{1}{3} \frac{r_i r_j}{r^2} \right). \tag{1.18}$$

Thus, in the inertial subrange ($L \gg r \gg \eta$) the Kolmogorov hypotheses are sufficient to determine the second-order structure function.
Different set of experimental data show the behavior of the second order structure function and its scaling in the inertial subrange and in the viscous one ([3] and [4]), while in figure 1.4 second order velocity structure predictions of the Kolmogorov hypothesis in the inertial range have been tested by Saddoughi and Veeravalli [5]. The horizontal lines show the predictions of the hyoptheses, while the dots are the experimental data: the inertial subrange shows how the experimental observations

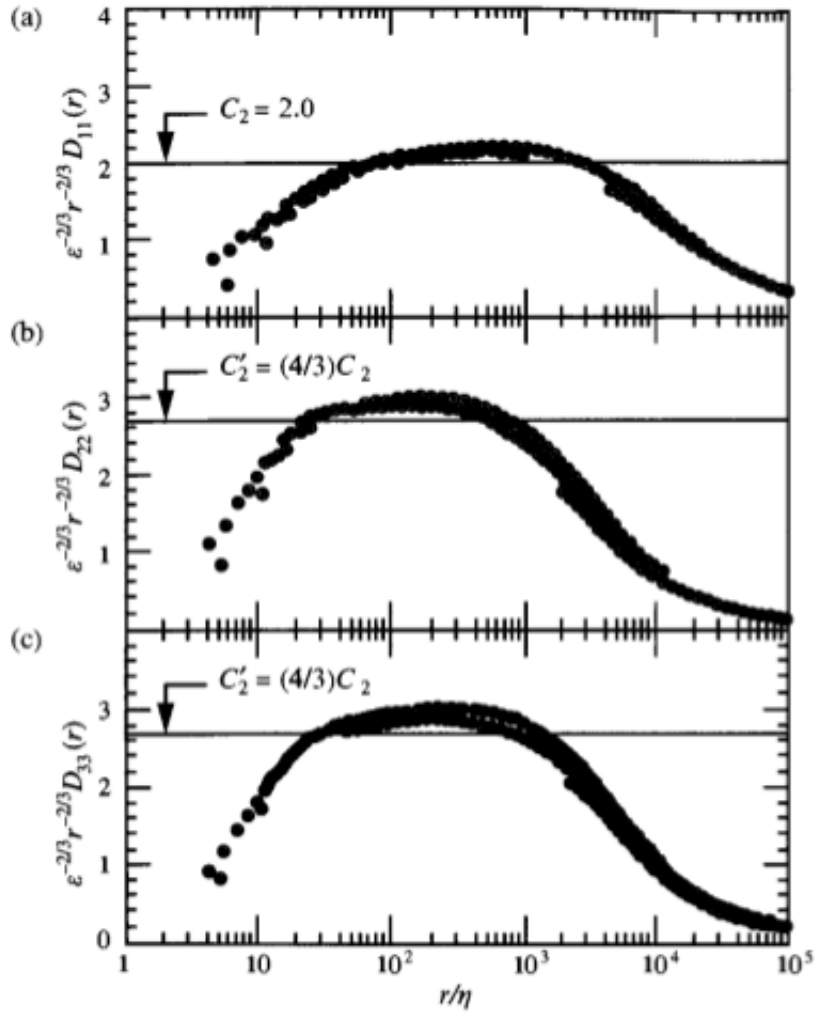

Figure 1.4: Second order velocity structure functions in an high Reynolds number boundary layer. Experimental data provided by Saddoughi and Veeravalli (1994).

provide support for the hypotheses made by Kolmogorov (while the universality of the constant C_2 has yet to be proved). The third order velocity structure function is:

$$D_{LLL}(r,t) =< \left[u_1(\mathbf{x}+\mathbf{e}_1 r,t) - u_1(\mathbf{x},t)\right]^3 >, \tag{1.19}$$

which, after some mathematics involving the Kàrmàn-Howart equation (Pope, page 202 [2]), becomes the Kolmogorov Equation

$$\frac{3}{r^5}\int_0^r s^4 \frac{\partial}{\partial t} D_{LL}(s,t)\, ds = 6\nu \frac{\partial D_{LL}}{\partial r} - D_{LLL} - \frac{4}{5}\varepsilon r. \tag{1.20}$$

In locally isotropic turbulence the time dependent term on the left side is zero, while the viscous one is negligible in the inertial subrange. This leads to the useful result of the $-4/5$ Kolmogorov law for the third order structure function:

$$D_{LLL}(r,t) = -\frac{4}{5}\varepsilon r. \tag{1.21}$$

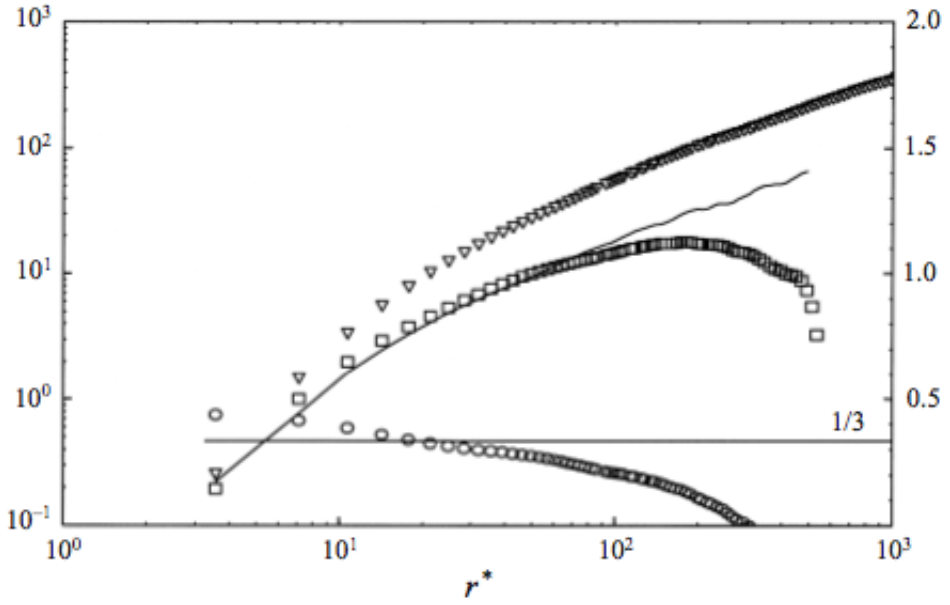

Figure 1.5: Third order velocity structure function ($\bigtriangledown$) with r scaling. Experimental data provided by Romano and Antonia.

1.4.2 Autocorrelation functions

Starting from the definition of the two-point correlation

$$R_{ij} \equiv < u_i(\mathbf{x}+\mathbf{r},t)\, u_j(\mathbf{x},t) >, \tag{1.22}$$

in case of homogeneity and zero mean velocity, r.m.s. and ε , the above formula is independent of x. At the origin is:

$$R_{ij}(0,t) = < u_i u_j > = u'^2 \delta_{ij}. \tag{1.23}$$

Just as previously done with the second order structure function D_{ij}, a consequence of the isotropy is that R_{ij} may be expressed in terms of two scalar functions $f(r,t)$ and $g(r,t)$, respectively called longitudinal and transverse autocorrelation functions:

$$R_{ij}(\mathbf{r},t) = u'^2 \left(g(r,t)\,\delta_{ij} + [f(r,t) - g(r,t)]\,\frac{r_i r_j}{r^2} \right), \tag{1.24}$$

that, considering $\mathbf{r} = \mathbf{e}_1 r$, becomes

$$\begin{aligned} R_{11}/u'^2 &= f(r,t) =< u_1(\mathbf{x}+\mathbf{e}_1 r,t)\,u_1(\mathbf{x},t) > / < u_1^2 >, \\ R_{22}/u'^2 &= g(r,t) =< u_2(\mathbf{x}+\mathbf{e}_1 r,t)\,u_2(\mathbf{x},t) > / < u_2^2 >, \\ R_{33} &= R_{22}, \qquad R_{ij} = 0, \qquad for\ i \neq j, \end{aligned} \tag{1.25}$$

Longitudinal and transversal autocorrelation functions are non-dimensional with $f(0,t) = g(0,t) = 1$, and in isotropic turbulence the two point correlation $R_{ij}(\mathbf{r},t)$ is completely determined by the longitudinal autocorrelation function, that is because:

$$g(r,t) = f(r,t) + \frac{1}{2} r \frac{\partial}{\partial r} f(r,t)\,. \tag{1.26}$$

In the last part of this section some of the results found in literature will be shown. These results will be useful when, in chapter 4, the chosen turbulent field will be analyzed.

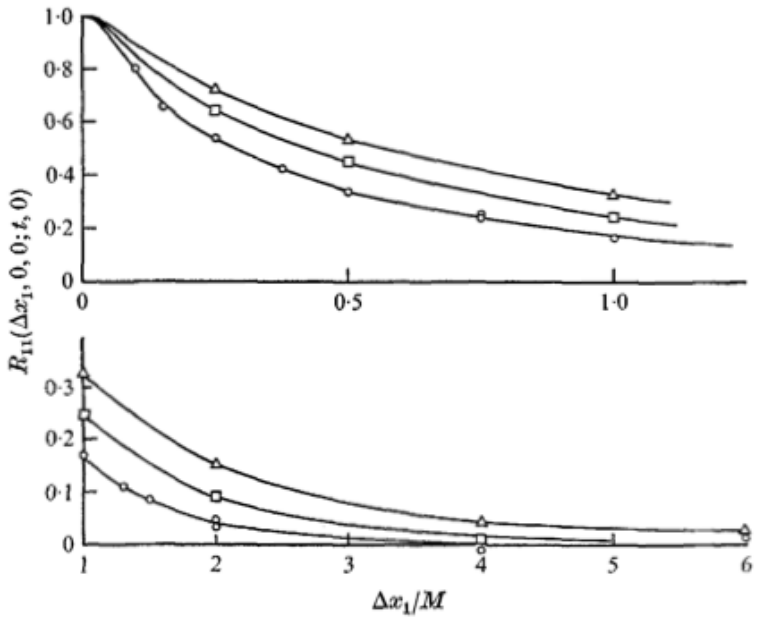

Figure 1.6: Downstream evolution of the longitudinal autocorrelation function for a grid-generated turbulence. Comte-Bellot 1971

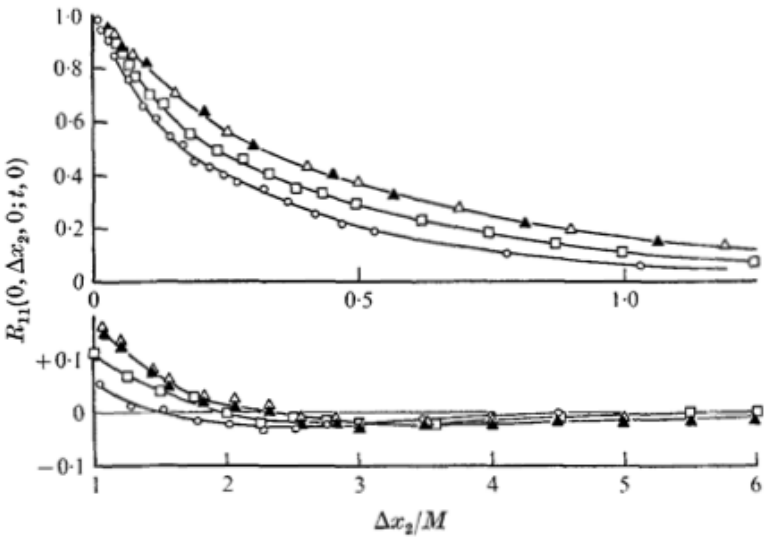

Figure 1.7: Downstream evolution of the transversal autocorrelation function for a grid-generated turbulence. Comte-Bellot 1971

In figure 1.6 the longitudinal autocorrelation function from the experimental data obtained by Comte-Bellot and Corrsin [6] is shown, while in figure 1.7 the transverse autocorrelation function it is shown. Giving a closer look at the figures we see that the transversal autocorrelation function decays more rapidly than the longitudinal one, reaching negative values for high values of $\Delta x/M$ (that is $\mathbf{r}/M$ with M as the grid mesh in the experiment), while the longitudinal autocorrelation function mantains itself positive for the whole domain. This behavior has been confirmed by Townsend [7] as it can be seen in figures 1.8 and 1.9. Townsend in his work considered two kind of turbulence, one with eddies of the same size and the other one with a wide spectrum of eddies' sizes. The results, shown in figure 1.8 and 1.9, confirm what we saw in figures 1.6 and 1.7, furthermore introducing the concept that the initial curvature of the autocorrelation function may be an indication of which kind of eddies are to be considered. Taking a closer look at the figures, we see that the one-dimensional correlation functions are smooth in the case of eddies of the same size, while they show a locally high curvature in the second case.

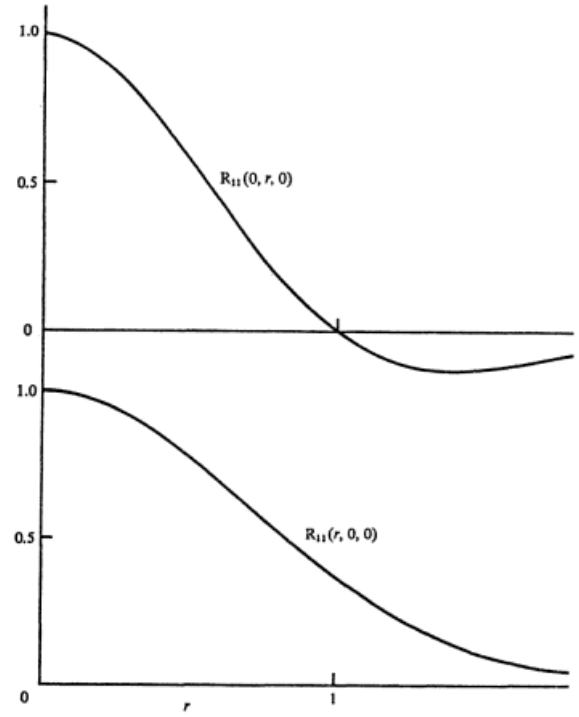

Figure 1.8: Correlation functions for isotropic turbulence with eddies of the same size. Townsend

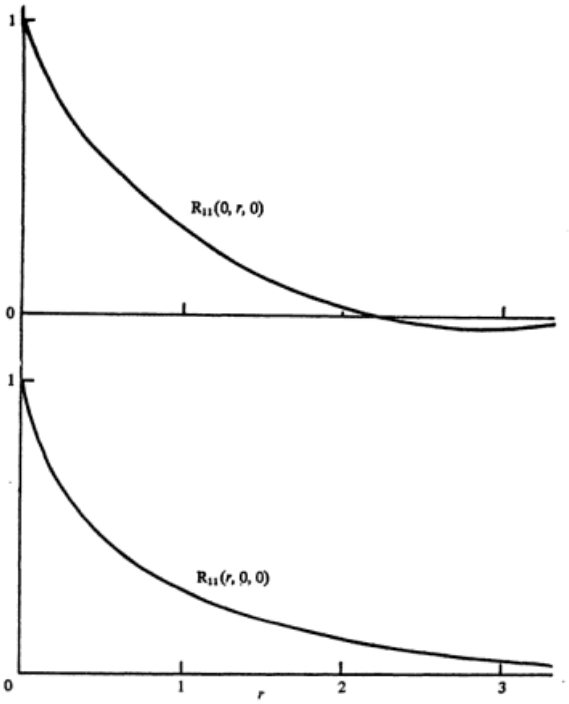

Figure 1.9: Correlation functions for isotropic turbulence with eddies of a wide range of sizes. Townsend

Thanks to the definitions of the longitudinal and transverse autocorrelation function, two distinct longitudinal and transverse lengthscales may be defined. Starting from the longitudinal autocorrelation function we may obtain longitudinal integral scale that is:

$$L_{11}(t) \equiv \int_0^\infty f(r,t)\, dr, \tag{1.27}$$

and is a characteristic of the larger eddies. In isotropic turbulence, taking into account the transverse autocorrelation function, L_{22} may be defined as half of L_{11}. In general:

$$L_{22}(t) \equiv \int_0^\infty g(r,t)\, dr. \tag{1.28}$$

Another lengthscale may be introduced: this is the Taylor microscale λ that can be seen as the characteristic dimension of the smallest dynamically significant eddies of the flow. It may be obtained after performing some mathematics involving the Taylor series expansion of f or g around the origin, with the final formula being:

$$\lambda_f^2(t) = -\frac{2}{f''(0,t)}, \tag{1.29}$$

while the transversal one is:

$$\lambda_g(t) = \left[-\frac{1}{2}g''(0,t)\right]^{-1/2}. \tag{1.30}$$

1.4.3 Spectral Analysis

In this work the one and three dimensional spectra will be considered. For a deeper examination on velocity spectra the work of Pope may be taken into account [2]. Starting from the definition of longitudinal and transverse autocorrelation functions 1.25, the equation for the one-dimensional spectra $E_{ij}(\kappa_1)$ is defined as twice the one dimensional Fourier transform of R_{ij}:

$$E_{ij}(\kappa_1, t) \equiv \frac{1}{\pi}\int_{-\infty}^\infty R_{ij}(e_1 r_{1,t})\, e^{-ik_1 r_1} dr_1. \tag{1.31}$$

Pope shows that in isotropic turbulence the one-dimensional spectra may be calculated starting from the energy-spectrum function $E(\kappa)$, that is, after some mathematics:

$$E_{11}(\kappa_1) = \int_{-\infty}^\infty \int \frac{E(\kappa)}{2\pi\kappa^2}\left(1 - \frac{\kappa_1^2}{\kappa^2}\right) d\kappa_2 d\kappa_3, \tag{1.32}$$

while the transverse counterpart is determined by E_{11} only:

$$E_{22}(\kappa_1) = \frac{1}{2}\left(E_{11}(\kappa_1) - \kappa_1 \frac{dE_{11}(\kappa_1)}{d\kappa_1}\right). \tag{1.33}$$

That said, in isotropic turbulence energy spectrum function is

$$E(\kappa) = -\kappa \frac{d}{d\kappa} \frac{1}{2} E_{ii}(\kappa). \tag{1.34}$$

An example of the behavior of the three-dimensional and one-dimensional spectra has already been provided in figure 1.2, in which the solid line represents $E(\kappa)$ while dashed lines are $E_{11}(\kappa)$ and $E_{22}(\kappa)$. As previously explained, in the center of the wavenumber range (that is the inertial subrange), the $-5/3$ power law introduced in equation 1.9 may be observed.

All of these results, equations and figure included, will be taken into account in a latter analysis of the validation of the chosen turbulent field with the Kolmogorov theory.

Chapter 2

Database and DNS description

A lot of papers and articles have been dedicated in the recent past to the DNS subject (for a review see [8], [9]), that is an argument of recent interest and still going development, thanks to the improvement of computing performances. In this chapter, after a brief introduction of the Direct numerical simulation method, the database chosen to accomplish our objective will be introduced.

2.1 The DNS method

In the past years turbulence has been a subject of interest for the community of researchers; this interest grew constantly because of the complexity of the argument, due to the nature of turbulence that is to possess a mixture of order, chaos and a wide range of length and time scales, as already explained in the previous chapter. This complex behavior is a consequence of an apparent simple set of equations, that is the Navier-Stokes one: non linearity, large number of degrees of freedom, sensitivity to flow conditions are just some of the causes of this problem.
We know that an analytical solution to even the simplest of the turbulent flows does not exist: a complete description of the flow, with space and time dependance, can be achieved only by numerical resolutions. These numerical resolutions are termed DNS, that stays for "direct numerical simulations".
The main feature of the DNS method is to solve the Navier-Stokes equations numerically and without the use of any turbulence model. This means that this method can solve the flow for the whole range of spatial and temporal scales. Starting from the smallest dissipative scales and up to the integral scale, all the spatial scales of the turbulence must be solved in the computational mesh.
DNS approach was born in 1971 and since then it developed along the progress of computational machines. In early years isotropic, incompressible and homogeneus flows could be computed: first of all, for example, a pioneering project of computing

a 32^3 grid point mesh was achieved [10], and since then it has been observed that the complexity of the flow analyzed noticeably increased (in 2007 the N^3 achieved was the 4096^3 of forced turbulence on the Earth Simulator), even if their Reynolds numbers were still low. DNS grew also as a research tool for flows that cannot be easily produced in laboratory because of their geometry (finite difference schemes and finite element method helped in this process); in fact, while the laboratory experiments are limited by geometrical flow problems, DNS is not because geometry can be "easily" manipulated by CAD softwares. On the contrary, DNS, as already said, cannot reach extremely high Reynolds numbers whereas a laboratory's experiment can.
All of the improvements that made DNS a better method have been accompanied by a significant improvement in computer hardware. It can be easily imagined that some of the hardware requirements for a fine DNS resolution, as for example large memory storage and personal computer's power, were improved significantly only in the last few years, finally contributing to the refinement of the DNS method.
DNS is still an unrivalled approach in the level of description provided, however it's important to notice that computational cost and time are still very high, and this is the major issue of this method. Minor problems that were solved in the long process of defining DNS method were numerical issues as spatial resolution, time advancement and definition of boundary conditions. For compressible flows, shock waves posed sever challenges to the method, too.
DNS has been labelled in the past as a brutal-force solution to the Navier-Stokes problem, but later it has been considered as a powerful research tool and a complement to the experiments made in laboratory.
At these days the contribution of direct numerical simulations to turbulence have been impressive even if some of their limits have not been yet overcome. DNS is being brightly used today for experiments with low-medium Reynolds number, but it is a method that is always open to evolution thanks to, for example, the use of parallel and high-performance computing that in the future may help to achieve results for more realistic turbulence conditions.
As previously stated, DNS is limited to flows with moderate Reynolds number, that is why DNS is a research and validation tool rather than a method for engineering design. While being still used for the resolution of the NS equations at all scales, different methods were explored in order to reduce one of the main cons of the DNS (that is the computational cost). Some of them are listed below:

- **RANS: Reynolds-Averaged Navier-Stokes simulation**:
  In this method, ensemble averaged flow variables are computed, while all the fluctuations are modelled with a turbulence model. This method is at low computational cost: in fact if only the main flow is simulated, the characteristic time scale will be much larger than the Kolomogorov ones, hence it is not

required time spacing.
There are some drawbacks, too: even with a cheaper computational cost the RANS method fails in providing a lot of information like velocity and pressure fluctuations. The major problem is the quest for an appropriate closure model: this may be obtained either via *turbulent viscosity hypothesis* or via *modelled Reynolds-stress transport equations*: several constant values must be defined for every simulation.

- **Large-Eddy simulation**:
  There is another approach for overcoming both the difficulties of DNS and RANS: in a LES (Large-eddy simulation) a spatial scale separation is applied, so that medium and larger scales are normally computed with a DNS while the small scales are treated separately. The main distinction between LES and RANS is that in the first there is a *spatial filtering* while in RANS there is a *temporal filtering*. Different types of filters may be applied and they affect the method directly because, after applying at the NS set of equation this filter, a new *anisotropic residual-stress tensor* has to be modelled. A closure is needed here too, with the most common one being the eddy viscosity type sub-grid closure. The problem in this method is determining the value of the *eddy viscosity* itself: different choices were proposed during the years, like Smagorinsky model or Germano's one. The main inconvenient of adopting the Smagorinsky model was that a single value of the problem's constant was not suitable for achieving consistent results in different types of flow; Germano instead tried to adjust dynamically the constant to the local structure of the flow [11]. Damping functions are needed too: subgrid-scale stresses do not vanish at the boundaries of the domain.

2.2 The Johns Hopkins Turbulence Database

The dataset that we chose for this work is a resolved DNS of a forced isotropic turbulent field being part of a database that contains two more datasets (a MHD DNS and a fully developed turbulent flow in a channel) [12]. The database was made with the purpose of creating a comprehensive data archive, providing the users the ability to explore a multi-terabyte database thanks to a feasible interface [13]. This interface makes possible the interaction between the database and a computational program running on a user's personal computer. Data may be obtained whenever needed, and may be used to perform further analysis on the local machine of the user. Some useful codes, written in Matlab or FORTRAN language, are provided to facilitate the user in downloading and processing data.
This database demonstrated compliance with our criteria, as well as other researchers'

needs too. The list of the publications made thanks to this database is hence long and it includes, among others, the works listed below:

- In 2010 Gungor and Mengon worked on a new hybrid approach for two-scale model for large eddy simulation of wall-bounded flows [14].

- In 2010 Yu and Meneveau studied Langrangian time correlations values of velocity and pressure gradient, in order to achieve collapse of the correlation functions after reaching the inertial-range [15].

- In 2012 Wu and Chang published a paper for a study of rank-ordered multi-fractal analysis of the probability distributions in fluid turbulence, in order to provide a natural connection between the rank-ordered spectrum and the idea of one-parameter scaling for monofractals [16].

2.2.1 Dataset of a forced isotropic turbulence DNS

As previously said, we chose to analyze a forced isotropic turbulent field for our project. The dataset we chose, part of the bigger Johns Hopkins Turbulence Database, comes from a data simulation made by the Johns Hopkins University of Baltimore in collaboration with the Peking University in Beijing, China.
The data is from a 1024^3 periodic grid simulation, made by using a pseudo-spectral parallel code. Integrating factor is used for time integration of the viscous term, that hence was done analytically. The other terms are integrated using a multi-step method, that is the second-order Adams-Bashforth scheme one, while the nonlinear term is written in vorticity form. The simulation is de-aliased using a phase-shift and a $2\sqrt{3}/3$ truncation. Energy is injected by keeping constant the total energy, in a way that their wave-number magnitude $|k|$ is less or equal to 2. After the simulation has reached the statistical stationary state, 1024 frames of data including the three components of the velocity vector and the pressure are generated and stored in the multi-terabyte database. The duration of the stored data is about one large-eddy turnover time T_L.
The domain of the field is a 2π x 2π x 2π cube, that is a range of x_1, x_2 and x_3 of [0,2π]. Viscosity ν is 0.000185 and the simulation time-step $\Delta t = 0.0002$. Data are stored every 10 DNS time-steps, so they are separated by a $\delta t = 0.002$. Time is stored between $t = 0$ and $t = 2.048$. There was another dataset available for download, a finer one made for testing purposes, that acquired the data every single time step (and not every 10 step as the one we chose) for t between [0.0002,0.0198]. Some of the main characteristics of the field, and respective formulas, are listed below. They are time averaged over $t = 0$ and $t = 2.048$.

- Distance between nodes:

$$d = \frac{2\pi}{1024} = 0.006136. \tag{2.1}$$

- Total kinetic energy:

$$E_{tot} = \left\langle \sum_k \frac{1}{2}\hat{\mathbf{u}} \cdot \hat{\mathbf{u}}^* \right\rangle_{time} = 0.695. \tag{2.2}$$

- Dissipation:

$$\varepsilon = \left\langle \sum_k \left(\nu\kappa^2 \hat{\mathbf{u}} \cdot \hat{\mathbf{u}}^*\right) \right\rangle_{time} = 0.0928. \tag{2.3}$$

- R.m.s. velocity:

$$u' = \sqrt{\left(\frac{2}{3}\right) E_\kappa} = 0.681. \tag{2.4}$$

- Taylor micro-scale

$$\lambda = \sqrt{\frac{15\nu u^2}{\varepsilon}} = 0.118. \tag{2.5}$$

- Reynolds at the Taylor scale:

$$Re_\lambda = \frac{u\lambda}{\nu} = 433. \tag{2.6}$$

- Kolmogorov length scale:

$$\eta = \frac{\nu^{3/4}}{\varepsilon^{1/4}} = 0.00287. \tag{2.7}$$

- Kolmogorov time-scale:

$$\tau_\eta = \sqrt{\frac{\nu}{\varepsilon}} = 0.0446. \tag{2.8}$$

- Integral scale:

$$L = \frac{\pi}{2u^2} \int \frac{E(\kappa)}{\kappa} d\kappa = 1.376. \tag{2.9}$$

- Large eddy turnover time:

$$T_L = \frac{L}{u'} = 2.02. \tag{2.10}$$

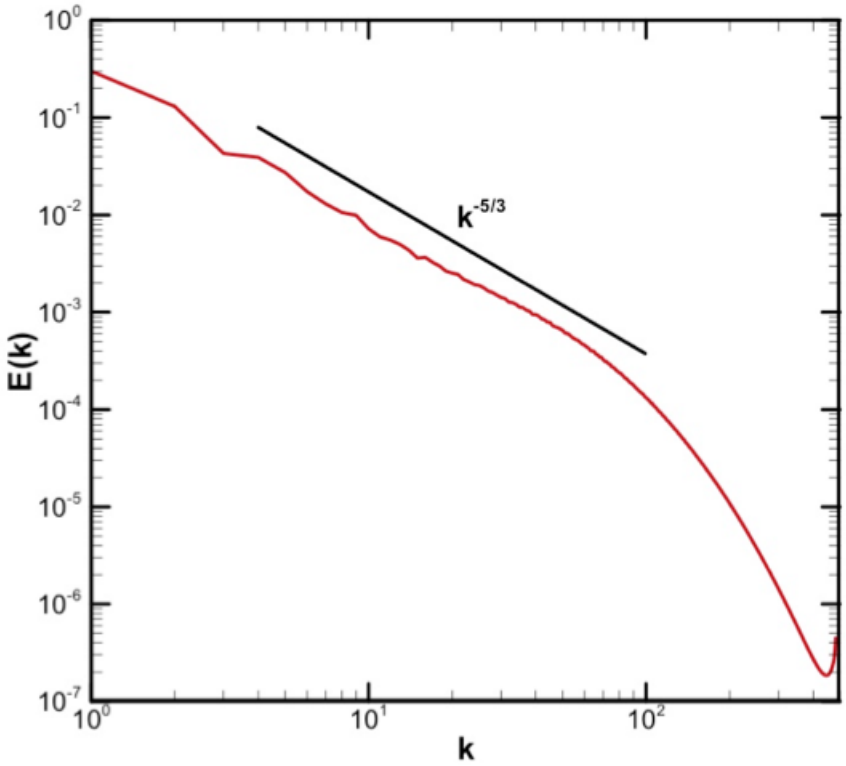

Figure 2.1: Radial kinetic energy spectrum, averaged in time t = [0,2.048]

In figure 2.1 the radial kinetic energy spectrum of the dataset is shown: as it can be seen, the scaling of the $-5/3$ Kolmogorov law is represented too for the inertial subrange. We observe that the scaling applies also for smaller k values, and that is because of the forcing that acts on bigger scales.
In figure 2.2 it is shown the time scale of the total kinetic energy which, as previously explained, is injected in a way that the wave-number magnitude is less or equal 2. The dashed part of the line stands for the time before the acquiring of the data in the database, that is before reaching a statistically stationary state. Data corresponding to the database are represented by the solid line. The same thing applies for the figure 2.3, in which the time series of the Taylor scale Reynolds is represented.
In figures 2.4 and next, time evolution of the velocity vectorial field is shown for a two-dimensional grid (800x800) at a z section equal to z=512. The arrows show the velocity vectors, while the colormap show the evolution of the z component of the velocity. Six different timesteps are shown, in order to provide an entire view of the evolution of the field.

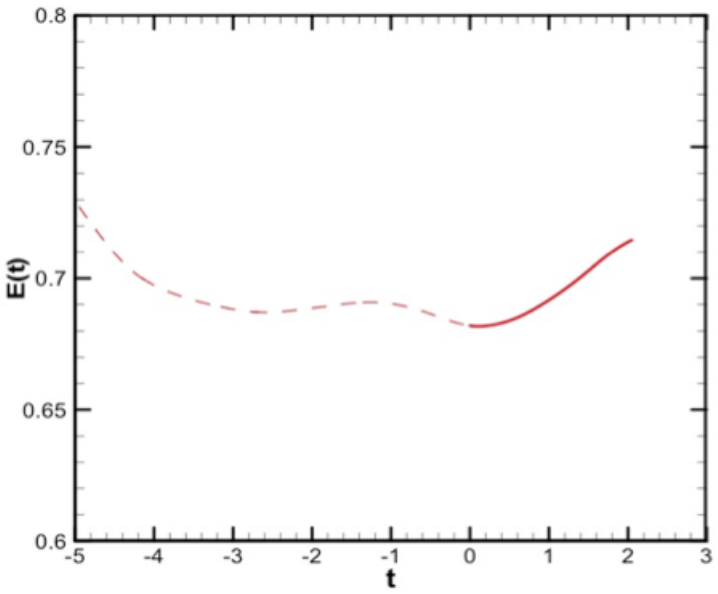

Figure 2.2: Time series of the total kinetic energy

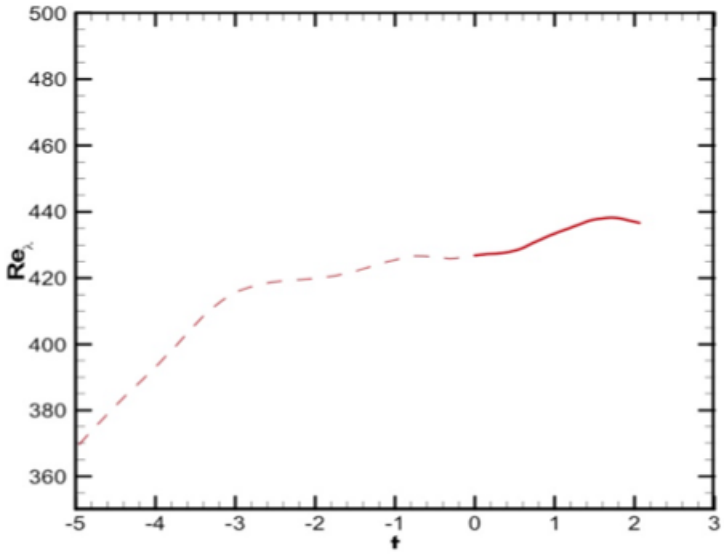

Figure 2.3: Time series of the micro-scale Reynolds number

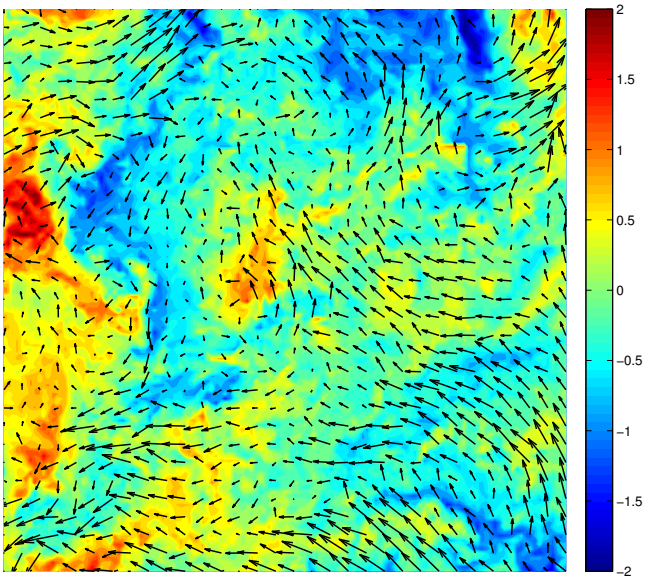

Figure 2.4: 800 x 800, z=512 grid: colormap indicates value of the z component of velocity, while vectors indicate velocity. Timestep $t = 1$

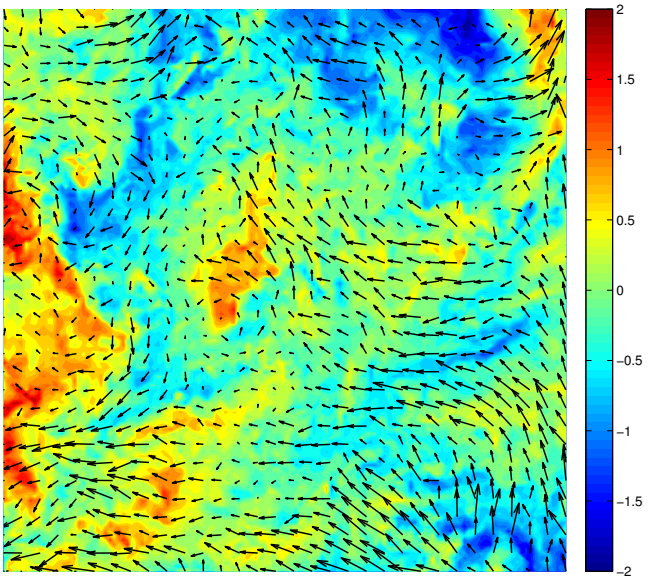

Figure 2.5: 800 x 800, z=512 grid: colormap indicates value of the z component of velocity, while vectors indicate velocity. Timestep $t = 200$

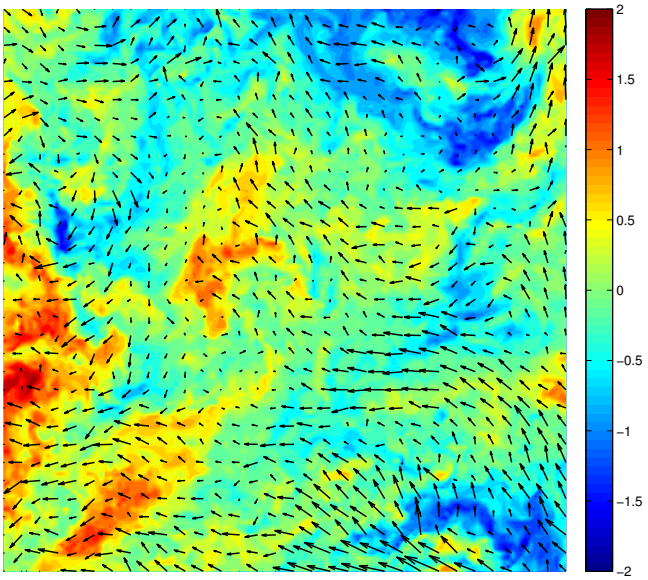

Figure 2.6: 800 x 800, z=512 grid: colormap indicates value of the z component of velocity, while vectors indicate velocity. Timestep $t = 400$

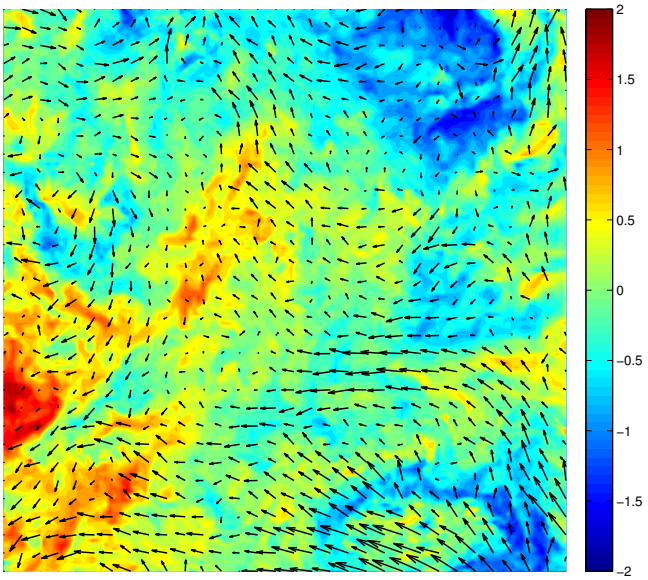

Figure 2.7: 800 x 800, z=512 grid: colormap indicates value of the z component of velocity, while vectors indicate velocity. Timestep $t = 600$

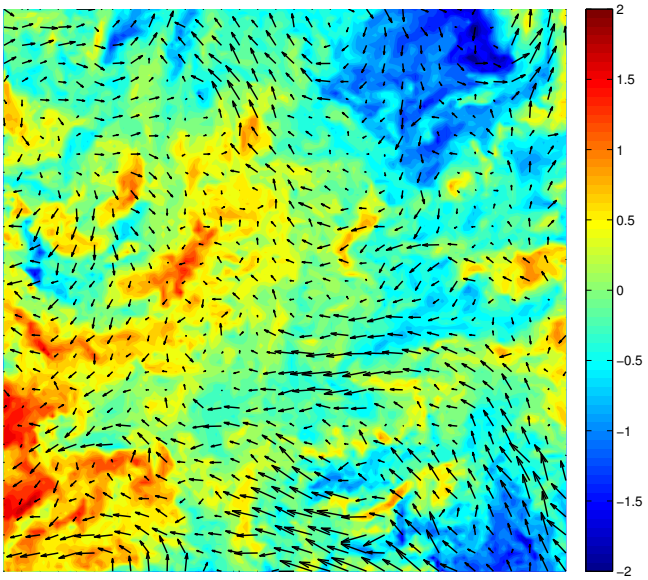

Figure 2.8: 800 x 800, z=512 grid: colormap indicates value of the z component of velocity, while vectors indicate velocity. Timestep $t = 800$

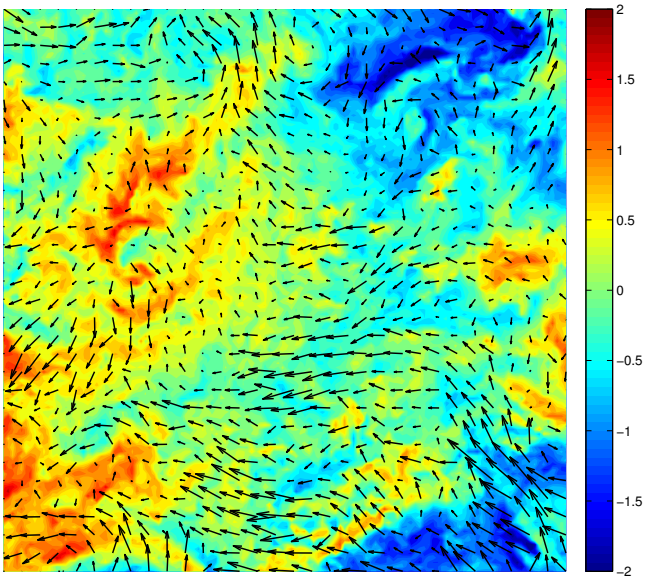

Figure 2.9: 800 x 800, z=512 grid: colormap indicates value of the z component of velocity, while vectors indicate velocity. Timestep $t = 1000$

In figures 2.10, 2.11, 2.12, 2.13 and 2.14 the time evolution of a small portion of the energy field is shown and is taken as an example. This portion, in particular, is a small circle with a diameter of 65 cells circa centered around the node placed at coordinates (280,280). The colorbar shows the magnitude of the value of the kinetic energy.

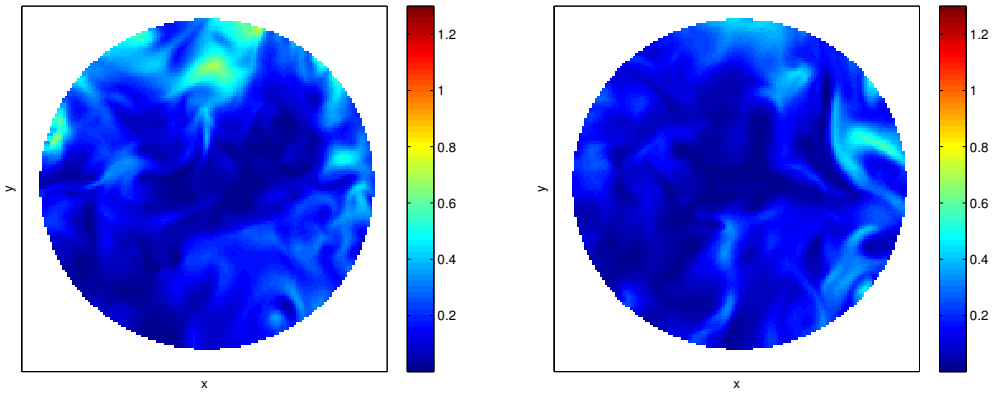

Figure 2.10: Time evolution of the kinetic energy of a field centered around the node 280x280. Timesteps 100 and 200.

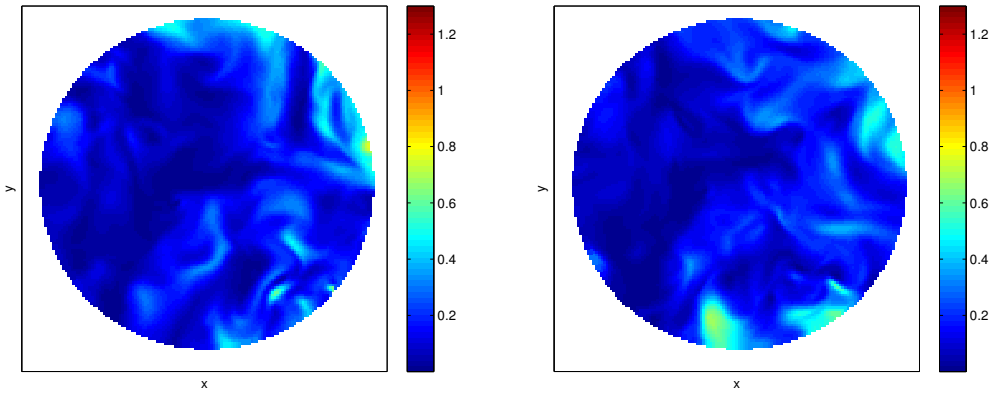

Figure 2.11: Time evolution of the kinetic energy of a field centered around the node 280x280. Timesteps 300 and 400.

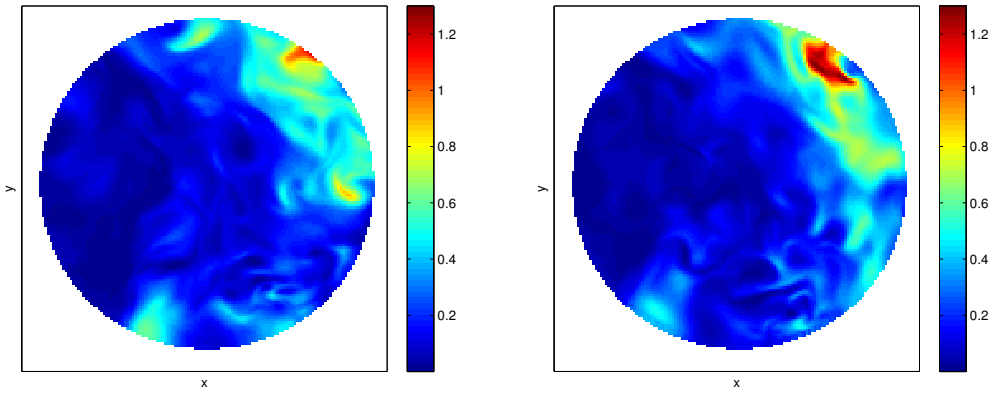

Figure 2.12: Time evolution of the kinetic energy of a field centered around the node 280x280. Timesteps 500 and 600.

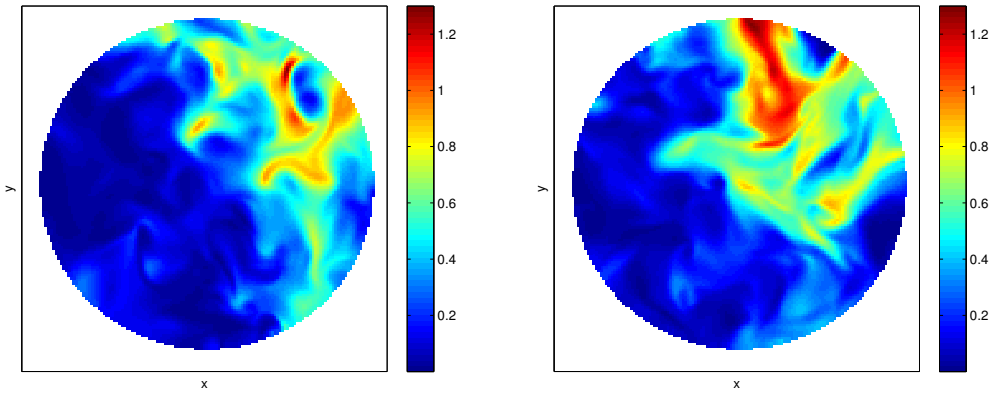

Figure 2.13: Time evolution of the kinetic energy of a field centered around the node 280x280. Timesteps 700 and 800.

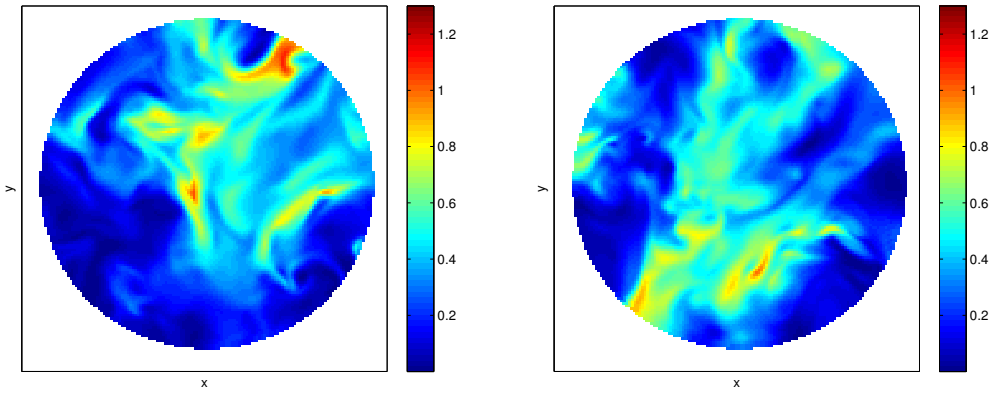

Figure 2.14: Time evolution of the kinetic energy of a field centered around the node 280x280. Timesteps 900 and 1024.

2.2.2 Data acquiring and pre-processing

To acquire the data from the database, a simple procedure was followed; we chose to use the section "Download Data Cutout" from the website, because it was more suitable for our work. The layout of the downloading section is represented in figure 2.15. After filling in an authorization token, obtained thanks to a website operator,

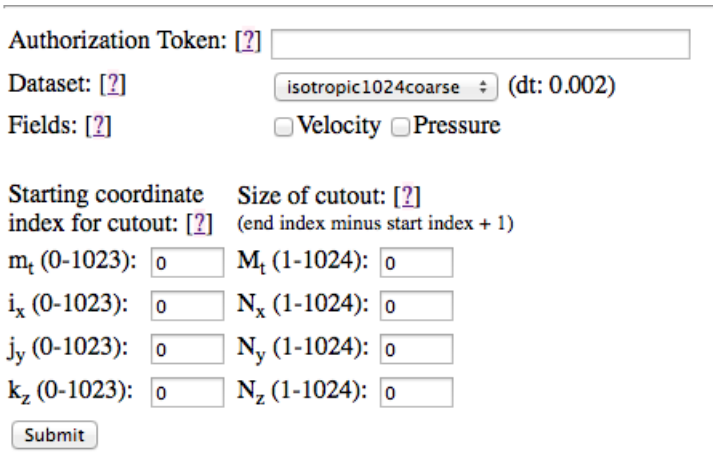

Figure 2.15: Layout of the data cutout section

dataset and field of interest is to be chosen. The data cutout section layout is very suitable to download portions, in space and time, of the field: the user is able to insert starting coordinates in the three directions and in time, and the size of the

cutout. An output was generated in a Hierarchical Data Format, that is a .h5 extension.
During the downloading process, due to some limitation of the database's server, it was possible to download cutouts of dimension equal to 800 x 20 x 1, hence 40 cuts were needed in order to fulfill our request to create a grid of 800 x 800 x 1. In particular, for our analysis, two grids were downloaded: the first one at the half of the z direction (we will refer to that as the $z = 512$ grid), the second one at $z = 212$. The grid were downloaded starting from $x = 112$ and $y = 112$ for a size of 800 in every of the two directions. Other smaller parts of the domain were then downloaded to provide a better understanding of the evolution of the parameters along the z direction too. Every part was downloaded in its integrity, composed hence of the whole 1024 temporal steps.
A MatLab code was then created to extrapolate from the .h5 files the three components of velocity, plus to compute the kinetic energy. This code, which may be seen in Appendix A.1, gave as outputs several .mat files containing matrices of dimensions 800 x 200 x 1024, which were then cut in order to manage smaller parts of the domain (for example 200 x 200 grids, as we will see in section 3.4).

Chapter 3

Complex network theory

Networks are all around us, the world wide web, social species, neural networks or highways and subways systems are just some of the many examples that may be provided: we are part of a network of social relationships, too. The most natural approach used to describe these systems is, of course, a network structured one. A network, in fact, is made of nodes that represent dynamical units, while the links between them stand for their "relationships": thanks to their simple nature, hence, great part of the systems of the world may be represented as networks.
With the always more appealing power of modern computers, network analysis grew constantly as one of the main instruments to describe real system properties.

3.1 The network approach: an historical introduction

The study of networks was conceived as a branch of discrete mathematics known as "graph theory", which was introduced firstly by the Swiss mathematician Euler in its Konigsberg bridge problem (1736): this problem consisted in finding a way to cross every bridge of the prussian city of Konigsberg exactly once. Since its birth this theory witnessed many developments and achieved a lot of results, providing answers to many practical questions (e.g. the "four colors theorem" or the "Hamiltonian path problem"). While actively used in a series of mathematical problems, only in the early years of the 20th century the theory became an important instrument to analyze social problems as communication and relationships between people. The social field in fact was the main one in which the theory of networks had its roots.
While network theory established itself as one of the main instruments for these problems, a new branch of it grew constantly, thanks to a renewed interest in research and, especially, thanks to the increased computing power: this was the "complex network analysis".

The study of the complex networks, which are networks whose structure is complex, irregular, and dynamically evolving in time, was meant as an instrument for systems with thousands or millions of nodes. This flurry of activity was triggered at the end of the 20th century by the pioneering works of Strogatz, Barabàsi and Albert ([17], [18]) which showed glimpses of the large possibilities of this kind of analysis. The appeal of this theory therefore was so strong that the physics' community became the principal actor in its growth.
During the last decades a lot of works were published in order to define global properties of the complex network theory ([19], [20]): these works contributed in distancing this new theory from the graph one. Graph theory in fact demonstrated itself as no longer suitable for real life systems, while still widely used in informatics and mathematics. Complex network theory, instead, established itself as the intersection between graph theory and statistical mechanics, hence assuming more popularity thanks to its flexibility and its natural reliability in representing virtually any discrete system.
Complex network theory is still a young and active area that is developing at fast pace: more and more fields of study, as for example engineering and biology, are being explored at the moment thanks to a huge researching activities that spread across many countries in the world.

3.2 Complex network: a brief survey of the applications

The theory introduced in this chapter had a huge impact in a lot of areas of study. The success of it could be imputed to contributing to new theoretical approaches and to satisfactory applications to real world problems [21].
As previously explained, one of the fields where this theory gained his major achievements is the social one: relationships among people have been crucial to guide cultural and economic evolution since ancient times. Social networks have been studied in a quantitative and primitive way for 3 centuries, but just in the last decades the analysis of empirical data grew as one of the main instruments for understanding social issues. Some of the most important concept of the complex network theory were conceived in the social field: the "small world" effect, which emerged from the famous Milgram social experiment about six degrees of separation, it's just one of the examples [22]. Since its first applications in the social field, a lot of different aspects of social communities were explored thanks to this theory: sports [23], sexual relations, migration [24], collaborations, terrorism [25] and folklore are just few of the areas of applications. This constant growth in analyzing social problems with this theory is at the moment still running thanks to larger and larger available

databases of real world data (e.g blogs or social networks). Communication network, in fact, had a huge impact on the theory, overcoming the practical difficulties of mapping the interactions between people thanks to the advent of Internet and mobile communications [26]. The World Wide Web has been widely analyzed with the complex network theory whereas being so difficult to map completely due to its depth and its constant evolution [27].
Another field in which the complex network theory excelled is the biological one. Modeling biological systems such as metabolic pathways, interacting proteins or genetic networks may be performed with this theory. By using complex network theory, a lot of properties of biological systems have been discovered in the recent years, including power law connectivity distributions, small-world properties, motif and community structures [28]. Furthermore, the crucial concepts needed to understand biological systems as emergence, robustness and modularity, are also ingredients of the general complex networks theory. Thanks to the network approach to biological problems, the theory has been useful in medicine too, due to the possibility of applying these concepts to understand disease's principles and their spreading [29], [30].
Networks have been used also to describe economic phenomena: industrial production, wealth spreading [31], tourism, trade [32] and currency are just some of the subjects that can be easily represented by discrete systems. Financial market, for example, is a highly complex evolving system that may be studied thanks to a network representation [33].
One of the recent fields to be analyzed thanks to the complex network theory, is the one of the Earth sciences: the study of earthquake's spatial distribution, for example, may be done in a form of network [34]. Climate networks' studies arose too, in which systems representing climate issues vary in a complex way: every node of the network represents cells of a grid that covers the whole globe, while connections among them represent the time correlation coefficient [35], [36].
All these different applications converged in the recent years to the engineering field. The complex network approach started to spread itself among the community of engineers, with some ideas still developing while others already realized. Transportation networks, for example, are already being analyzed thanks to this theory that helped to understand movement of people around the world. Airports [37], railways and subways network are just few of the examples of experiments carried out successfully.
Eventually, complex networks have been a topic of conferences in different fields since its birth, and while its principles are already well defined, more will be done with its endless possibilities and constant growth.

3.3 The structure of complex network: properties and definitions

In this section just few of the concepts of the complex network theory will be introduced. As previously explained the theory is still developing itself at a fast pace, gaining contribution from a variety of fields of studying, this means that new definitions and properties of complex networks are surfacing constantly. Therefore in this section we will limit the list of parameters and definitions to the ones we used in this work.
A complex network may be represented as a graph which consists of two sets N and L, such that $N \neq 0$ and L is a set of pairs of elements N. We call the elements of N as nodes (or vertices, or points), while the elements of L are named links (or edges, lines). In an unordered graph the order of links is not important, whereas in an ordered one links are defined by their direction, too.
In a graph nodes may be drawn as dots linked with lines: how these dots and lines are drawn is irrelevant because the only thing that matters is if a pair of nodes form a link or not. Two nodes that form a link are referred to as *adjacent* (or neighbouring), a single node cannot be linked to himself (i.e. there are not loops in the network), and two nodes cannot be linked by more than one links (no multiple edges).
Networks may be divided into two sub-categories: unweighted ones and weighted

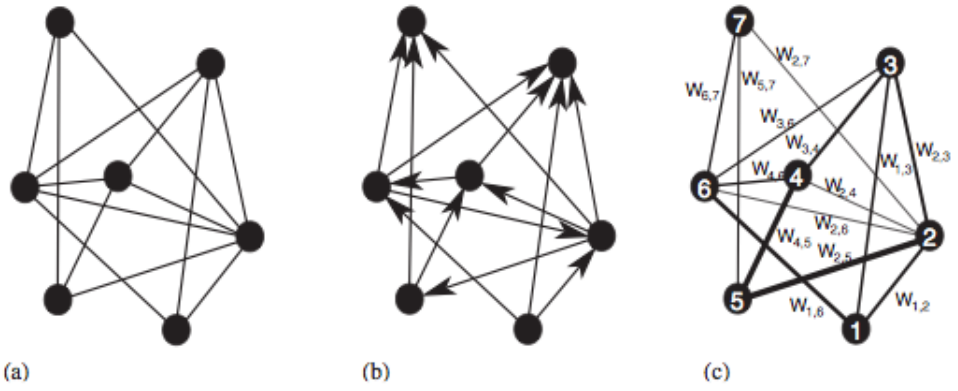

Figure 3.1: Graphical representation of a undirected (a), a directed (b), and a weighted undirected (c) graph with N = 7 nodes and K = 14 links.

ones. Unweighted networks are networks in which there is an homogeneity in intensity of links. Weighted networks, instead, present large heterogeneity in the capacity and the intensity of the connections, therefore are more suitable for the usage in real

world problems.
Another important concept of this theory is the one of reachability of two different nodes. Two nodes that are not adjacent may not be reachable from one to the other but through an alternative *walk*, that is a different sequence of nodes and edges that begins and finish with the two starting nodes: a trail is a walk in which no edge is repeated, while a path is a walk in which no node is visited more than one time. The *shortest path* concept is therefore one of the main concept of the complex network theory: it is the walk of minimal length between two nodes.
A graph is connected if, for every pair of different nodes, there is a path between them, otherwise it is unconnected (or disconnected). In this work we will deal with undirected, unweighted and connected networks.
It's useful to introduce a matricial representation of a graph: this can be achieved with the *adjacency matrix* (or *connectivity*). An adjacency matrix is a N x N matrix in which every entry a_{ij} is equal to 1 if nodes i and j are adjacent, i.e. when the link l_{ij} exists, and zero otherwise. The adjacency matrix has a diagonal that contains 0 (that means that there aren't any self-loops) and it is symmetric for undirected graphs:

$$A_{ij} = \begin{cases} 1 & \text{if } i \text{ and } j \text{ are linked,} \\ 0 & \text{if } i \text{ and } j \text{ are not linked.} \end{cases} \tag{3.1}$$

Some important parameters that are going to be analyzed in this work are about to be introduced. The *degree centrality* of a node is defined as:

$$k_i = \frac{\sum_{j=1}^{N} a_{ij}}{N-1}, \tag{3.2}$$

with N number of nodes. The degree centrality gives the number of the nodes adjacent to the node i, normalized over the total number of possible neighbors $N-1$.
Thanks to the definition of degree centrality, the *degree distribution* $P(k)$ may be introduced too: it defines the fraction of nodes having a value of the degree centrality k. In other words, the degree distribution is the probability that a node in a network is connected to k other nodes.
The *weighted average topological distance* of a node is here defined as:

$$\overline{D}_i = \frac{\sum_{j \in nn(i)} d_{ij}}{N_{ci}} \frac{N-1}{N_{ci}}. \tag{3.3}$$

In these equation d_{ij} is the shortest path length between the two nodes i and j, that is the minimum number of edges that have to be crossed from the node i to the node j, while $nn(i)$ is the complete set of all the nodes adjacent to i. N_{ci} is the number of the neighbors of the node i, and it satisfies the condition $N_{ci} \in [1, N-1]$. The

ratios at the right member of equations 3.3 have different meaning: the first one measure the topological distance between the node i and the N_{ci} nodes adjacent to it, while the second one is a weight coefficient that indicates how strongly the node i is connected to the rest of the graph. This notation is quite different from the classic *average topological distance* definition which is:

$$\overline{d}_i = \frac{\sum_{j \in nn(i)} d_{ij}}{N-1}. \tag{3.4}$$

The two definitions are different in the case of a graph with disconnected components, while are equal for a connected one. In our work, since we are dealing with connected networks, the values of weighted average topological distance and average topological distance will be the same. A large value of the weighted average topological distance $\overline{D}_i$ means that the node is far from the rest of the network. In general, most of the nodes that show larger degree centrality values, have smaller values of weighted average topological distance.
Introducing Γ_i that is the set of first neighbors of the node i, a formula indicating the *local clustering coefficient* may be given:

$$C_i = \frac{e\left(\Gamma_i\right)}{\frac{k_i(k_i-1)}{2}}. \tag{3.5}$$

In this equation $e\left(\Gamma_i\right)$ is the number of edges connecting the vertices within the neighborhood Γ_i, and $k_i\left(k_i-1\right)/2$ is the maximum number of edges in Γ_i. A *global clustering coefficient* may be introduced too as:

$$\overline{C} = \sum_{i=1}^{N} \frac{C_i}{N}. \tag{3.6}$$

The local and global clustering coefficients are parameters that indicate the probability that two neighbors of a given node are also adjacent: the local coefficient is characteristic for a given point, while the global one indicates a general network's behavior.
The *betweenness centrality* of a node is defined as:

$$BC_k = \sum_{i,j \neq k} \frac{\sigma_{ij}\left(k\right)}{\sigma_{ij}}, \tag{3.7}$$

where σ_{ij} represents the number of shortest paths that connect nodes i and j while $\sigma_{ij}\left(k\right)$ is the number of shortest paths from node i to node j crossing node k. The betweenness centrality value is high for a node k which is crossed by a large number of shortest paths, which means that the node k may be considered an

important mediator of information for the network. Betweenness centrality and clustering coefficient are connected to each other: a node important in mediating information will probably have an high value of clustering coefficient. A large part of the networks analyzed showed that higher values of degree centrality mean higher values of clustering and betweenness coefficient, while smaller values of the weighted average topological distance. This is not always true, but it can be considered as a general behavior of the systems analyzed.

3.4 Building the network

In this work we decided to analyze two-dimensional portions of the three-dimensional domain. Starting from the 800 x 800 grid, different cuts were made in order to explore the downloaded two-dimensional grids.
First of all, a bigger grid of 200 x 200 nodes was cut, centered around the node of reference (0,0). For every node we had a temporal series for the energy (or for one of the three components of velocity). For this grid a code was written to select a circle of ray $r = 0.4$ (which corresponds to 65 nodes circa) centered around the node (0,0). After the selection of the 13333 nodes included in the circle, correlations in time between every couple of nodes of the network were computed. Three matrices are stored after the code ran: one for the values of correlations between all the nodes, and the other two for the coordinates of every node. The code is shown in Appendix B.1.

After the first selection of nodes, a second one has to be done in order to reach the definitive network form. In this code (Appendix B.2) the main input (other than the correlations matrix and their coordinates) to be inserted is the τ value, which is the threshold value of the correlation that we are going to consider. Along with this mathematical condition, two more geometrical conditions are considered in order to avoid results biased by the geometric position of each node (graphically represented in figure 3.2). Eventually a link between two nodes i and j may be taken into account if:

- $R_{ij} > \tau$ with R_{ij} time correlation value.
- At least one between nodes i and j lies inside the circumference with ray $r = 0.2$ and centered in (0,0);
- The physical distance between nodes i and j is less or equal to 0.2.

With this selection, every node included in a circumference with ray $r = 0.2$ and center (0,0) has a well-defined region of influence where links with other nodes may occur. Every node included in this circumference has the same potential number of links. The output of the code B.2 will give two vectors representing the coordinates

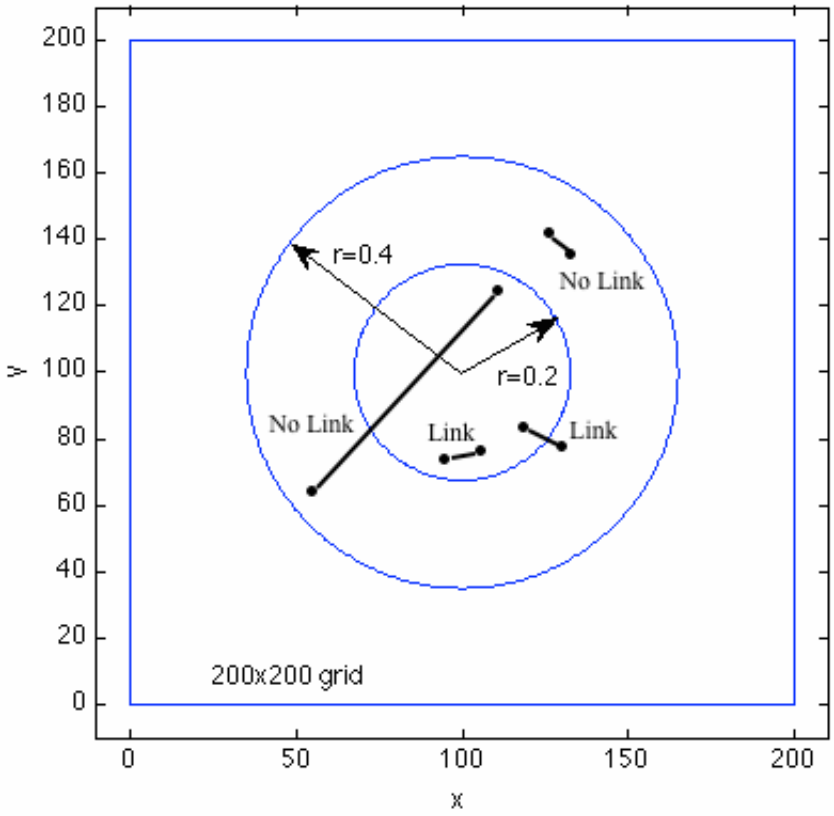

Figure 3.2: 200 x 200 starting grid, Circles of ray $r = 0.4$ and $r = 0.2$

of the active links, and a matrix of adjacency in which two values, 1 or 0, represent an active link or an inactive one. In so doing, the resulting network is undirected (A is symmetric) and unweighted (all the values above the threshold correspond to $A_{ij} = 1$). The selection of the threshold is a non-trivial aspect of building a network and is here mutuated for convenience from the climate network ([35], [38] and [39]). Since we are primarily interested in highlighting strong correlated connections, we consider two different threshold values, namely $\tau = 0.5$ and $\tau = 0.9$. For example, the network corresponding to the circumference centered in (280,280) at $z = 512$ shows with $\tau = 0.5$ a number of active links equal to $n = 5688943$ and a number of nodes equal to $N = 10451$. With $\tau = 0.9$ we have instead $n = 379581$ and $N = 4848$. A graphical representation of the nodes with the two threshold values is reported in figures 3.3 and 3.4 (edges between nodes are not reported due to the complexity of the figure). As expected, the network with lower τ has a wider spatial

extension than with higher τ.

The choice of the size of the domain of interest is linked to the Taylor scale, as

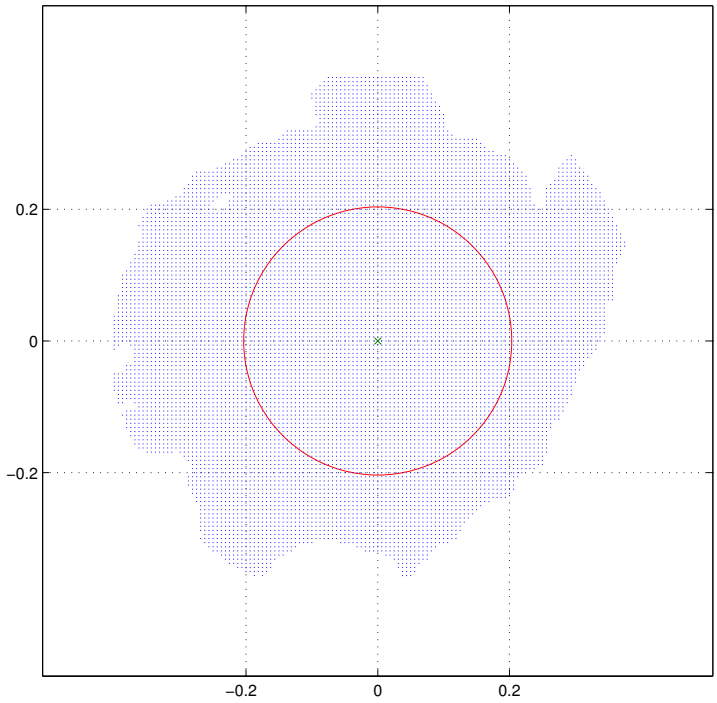

Figure 3.3: Network for the circumference centered in (280,280) at $z = 512$, $\tau = 0.5$. The network has N=10451 nodes and n=5688943 links.

we are mainly interested in what happens at scales of this order or smaller (Kolmogorov scales), where the spatial correlation is high. The autocorrelation function $f(r)$, computed in section 4.1.2, shows that the correlation remains considerably high even when the Taylor scale ($\lambda = 0.118$) is exceeded, therefore we almost doubled the Taylor scale in defining the domain of interest. In fact, the region we focus on for the following considerations is a circumference with ray $r = 0.2$.

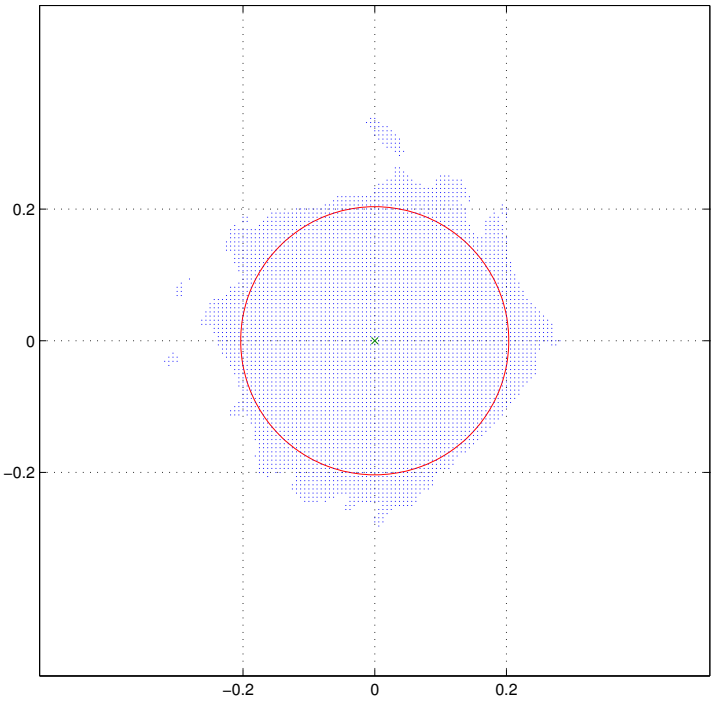

Figure 3.4: Network for the circumference centered in (280,280) at $z = 512$, $\tau = 0.9$. The network has N=4848 nodes and n=379581 links.

Chapter 4

Analysis of the turbulent field

In this chapter a deep review of all the results obtained in this project will be given. First of all the field that we extracted from the database will be analyzed with the classic methods of the dynamic of turbulence. We introduced these methods in chapter 1 where we defined several statistic tools that will help us in this process. These results will be compared with some literature's results and scaling, in order to test the consistency of the flow with the hypotheses of Kolmogorov.
After this classic analysis, a more original one will be pursued thanks to the instruments of the complex network theory. Several results, following the definitions introduced in chapter 3, will be shown with the purpose of drawing conclusions from this preliminary analysis.
The reader should take into account that this work is original in its field, hence there is not a counterpart of the results to be found in literature in order to make a comparison with.

4.1 A classic statistical approach

4.1.1 Structure functions scaling

First of all the structure functions are going to be analyzed. We chose to analyze second order structure functions for all the three components of the velocity.
As previously explained in chapter 1 equation 1.10, the second order structure function is the ensemble average of the product of the difference between velocities. Three second order structure functions will be shown here, computed thanks to code C.1 and scaled with the Kolmogorov hypoteses applied for the structure functions in section 1.4.1. In the process of computing the second order structure functions we chose to do an average value in time of a number of 1024 timesteps (when the field is

statistically stationary): the functions were averaged in space starting from a number of 160 samples over each direction. The graphs are drawn with logarithmic axes in order to have a better understanding of the Kolmogorov scaling in the inertial range.
In figure 4.1 the longitudinal second-order structure function (that is D_{LL} that we introduced before) is shown: as previously explained in equation 1.16 this function in the inertial range should be proportional to $r^{2/3}$, up to a multiplicative costant. Because of the isotropic characteristic of this field, in fact, this scaling is followed in the inertial range ($L \gg r \gg \eta$). The green line in the figure represents the temporal average of the functions, while the curve sheaf in the background is composed of every temporal step. The same scaling applies for the transversal second-order

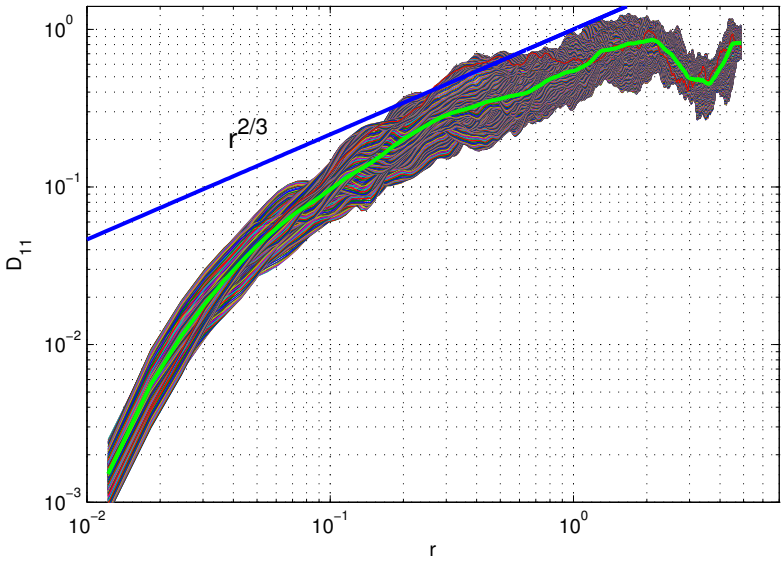

Figure 4.1: Longitudinal second-order structure function D_{11}. Kolmogorov scaling with $r^{2/3}$.

structure function: equations 1.12 and 1.17 show that $D_{22} = D_{33} = D_{NN}$ with D_{NN} scaled in the inertial subrange as $r^{2/3}$ (that is because, in isotropic turbulence, D_{NN} could be completely computed starting from D_{LL}). In figures 4.2 and 4.3 the two transversal second-order structure functions are shown. The Kolmogorov scaling applies also in these cases, but in a less clear way than the longitudinal function case.
In both the longitudinal and transversal second-order structure function the behavior far from the inertial sub-range is similar to what we expected: the curve diverges significantly from $r^{2/3}$ for $r \to \eta$ and for $r \to L$, hence distancing itself from the

Kolmogorov scaling.

The third-order structure function, instead, was computed thanks to the code in

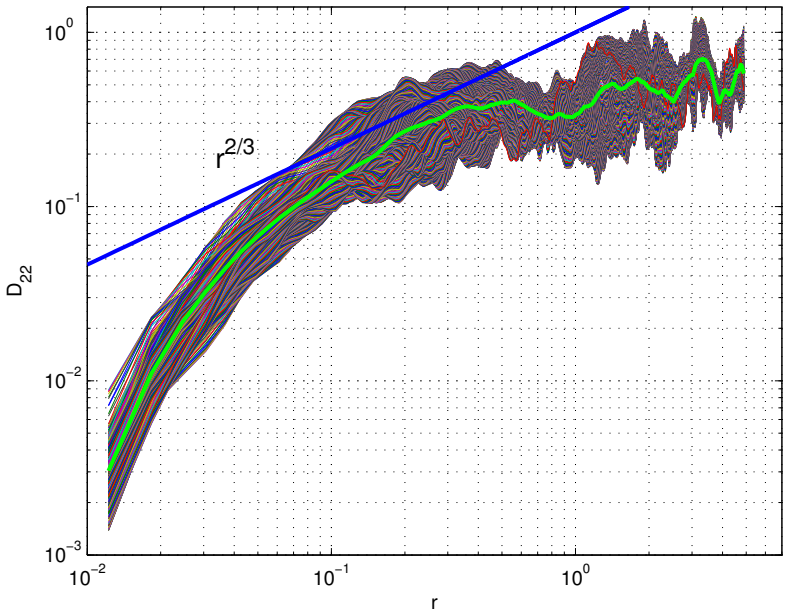

Figure 4.2: Transversal second-order structure function D_{22}. Kolmogorov scaling with $r^{2/3}$.

Appendix C.2. We chose to compute this only for the D_{111}, that is for the first component of velocity, averaged over 160 samples and then averaged in time (as we did for the second-order one). The characteristic equation for the D_{111} comes directly from the D_{LLL} introduced in equation 1.19, and it is scaled in the inertial subrange as r as we explained in equation 1.21. In this case the scaling is correct once again, and the curve in figure 4.4 shows the same global behavior that we saw for the second-order functions.

To achieve better results and in order to get smoother curves, the number of samples should have been increased: due to the machine computational power, in fact, we used just 160 samples. We could have used more samples, for example taken from different grids, and not only the $z = 512$ one as we did.

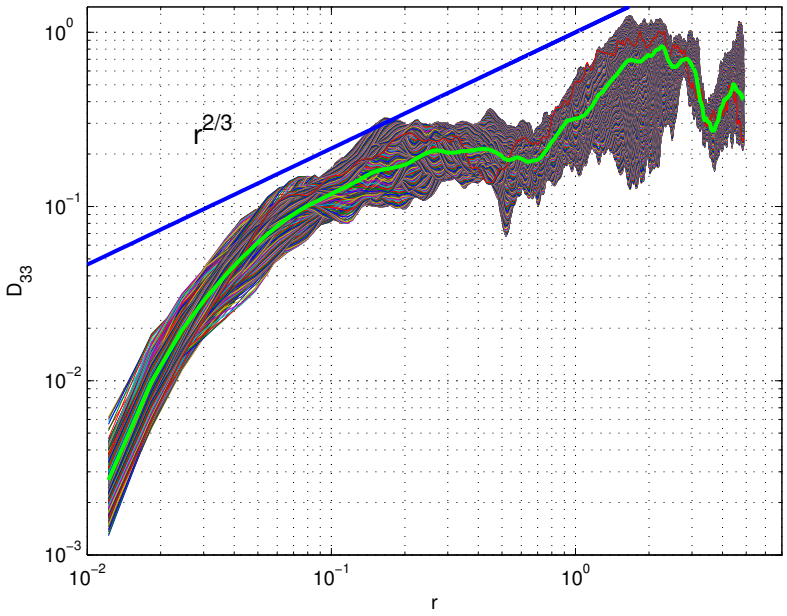

Figure 4.3: Transversal second-order structure function D_{33}. Kolmogorov scaling with $r^{2/3}$.

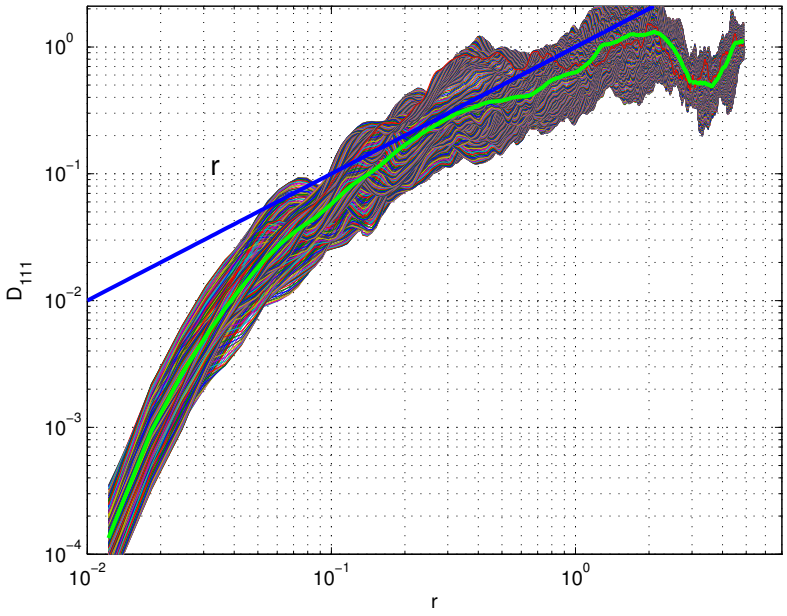

Figure 4.4: Longitudinal third-order structure function D_{111}. Kolmogorov scaling with r.

In figures 4.5, 4.6, 4.7 and 4.8 the structure functions averaged in time for both the grids $z = 212$ and $z = 512$ are showed, along with the their Kolmogorov scaling. As expected, in the inertial subrange the trend scales exactly as the Kolmogorov formulas for both the functions. Outside the inertial subrange, however, the trends are slightly different: this happens expecially for $r \to L$.

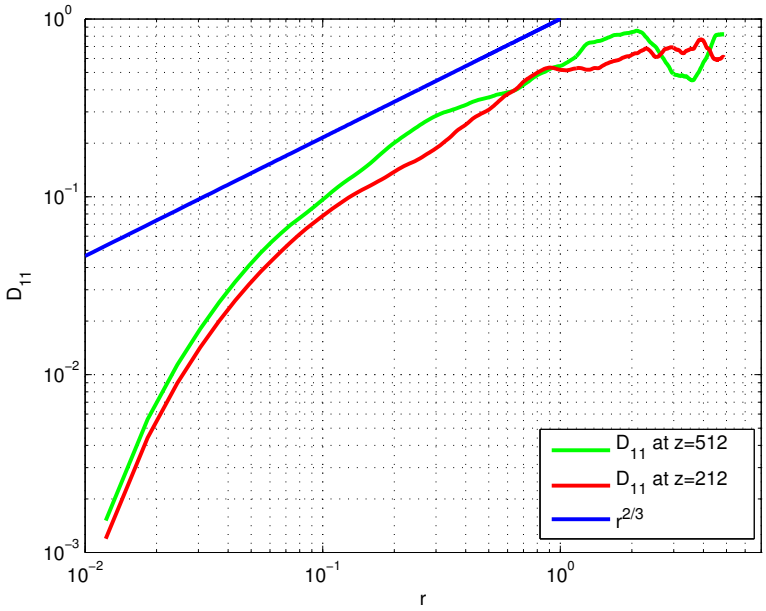

Figure 4.5: Longitudinal second-order structure function D_{11} for both the grids $z = 212$ and $z = 512$. Kolmogorov scaling with $r^{2/3}$.

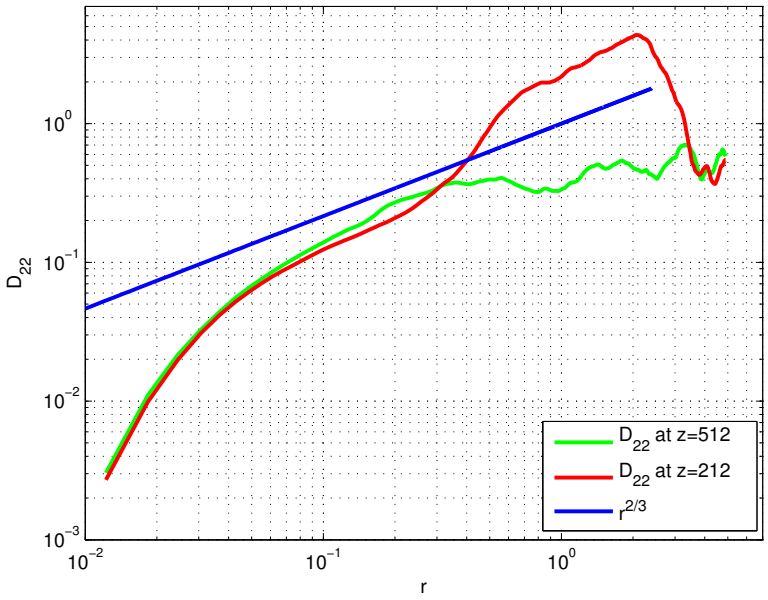

Figure 4.6: Transversal second-order structure function D_{22} for both the grids $z = 212$ and $z = 512$. Kolmogorov scaling with $r^{2/3}$.

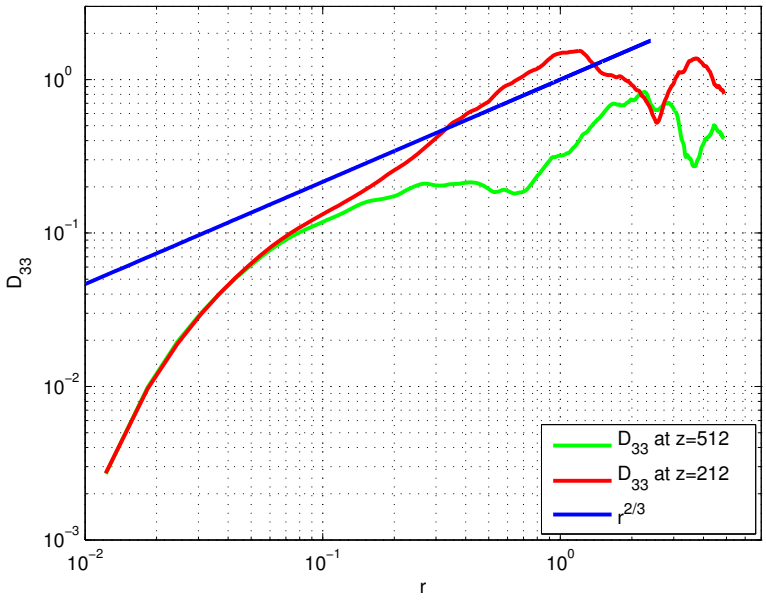

Figure 4.7: Transversal second-order structure function D_{33} for both the grids $z = 212$ and $z = 512$. Kolmogorov scaling with $r^{2/3}$.

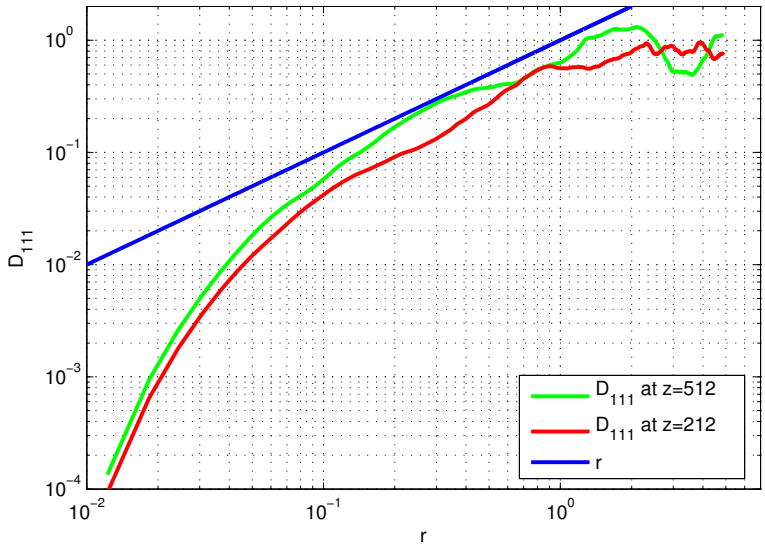

Figure 4.8: Longitudinal third-order structure function D_{111} for both the grids $z = 212$ and $z = 512$. Kolmogorov scaling with r.

4.1.2 Auto-correlation functions

In this section we will analyze some important statistical quantities which may be compared to several different results found in literature regarding the isotropic turbulent flow. We introduced the quantities of interest in section 1.4.2, providing some interesting results from different works and authors.
For all the quantities that we analyzed in this section we used the same number of samples that we used before for the structure functions, that was 160 samples averaged in spaces, and then averaged once again in time. The green curve stays for the final result, while in the background 1024 temporal steps are shown.The samples are taken from the grid $z = 512$ if not specified otherwise.
First of all the two-point correlation function in x direction R_{11} (equation 1.22) is going to be shown. This function indicates how much velocities in two different points distanced by **r** are correlated, and it's quite important because from that we may calculate the energy spectrum and the autocorrelation function. We expect the two point correlation to drop significantly for increasing distances r.
As we can see in figure 4.9 in fact the two-point correlation function drops significantly in a short range of r, reaching values near to zero when we approach the range $r \to L$.

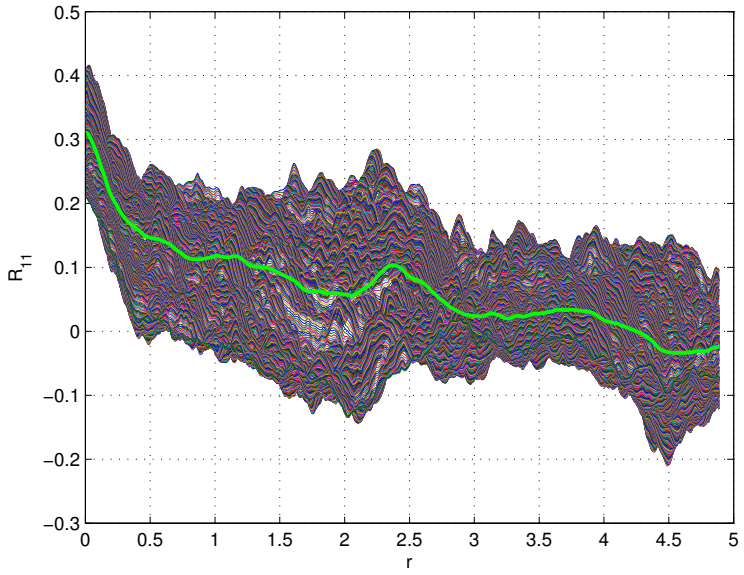

Figure 4.9: Two-point correlation function R_{11}.

The two-point correlation is useful when computing the longitudinal autocorrelation function $f(u)$ that has been defined in equations 1.25 along with its transversal

counterpart for the second component of the velocity $g(v)$. In this case the two auto-correlation functions are defined in this way:

$$\begin{aligned} f(u) &=< u(\mathbf{x}+\mathbf{e}_1 r,t)\, u(\mathbf{x},t) > / < u(0)^2 >, \\ g(v) &=< v(\mathbf{x}+\mathbf{e}_1 r,t)\, v(\mathbf{x},t) > / < v(0)^2 > . \end{aligned} \tag{4.1}$$

Figures 4.10 and 4.11 show the two above autocorrelation functions and as usual the two curves decrease in a way that can be compared to literature results reported for examples in Comte-Bellot's work in figures 1.6 and 1.7. The two longitudinal autocorrelation functions drop to zero at an $r \sim 2$, and after this value they diverge due to spurious effects, periodic boundary conditions and limitation in samples number; in particular the transversal one should reach negative values for bigger values of r, but this is not the case for $g(v)$ probably due to the limitation of samples. Characteristic in these cases is the behavior for smaller r values that confirm the fact that we are describing an isotropic turbulent flow, hence showing the universal behavior for smaller scales.
The codes used to compute the two autocorrelation functions are shown in Appendix C.3 and C.4, with the first one containing the two-point correlation R_{11}, too.

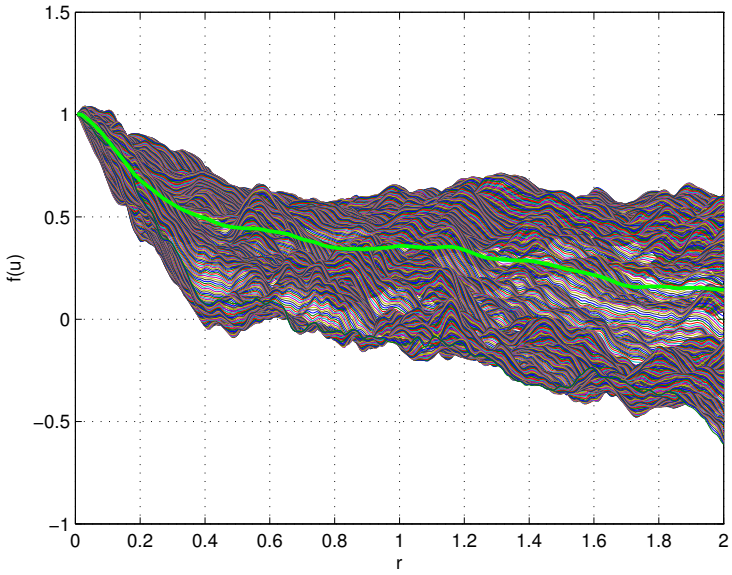

Figure 4.10: Longitudinal autocorrelation function $f(u)$.

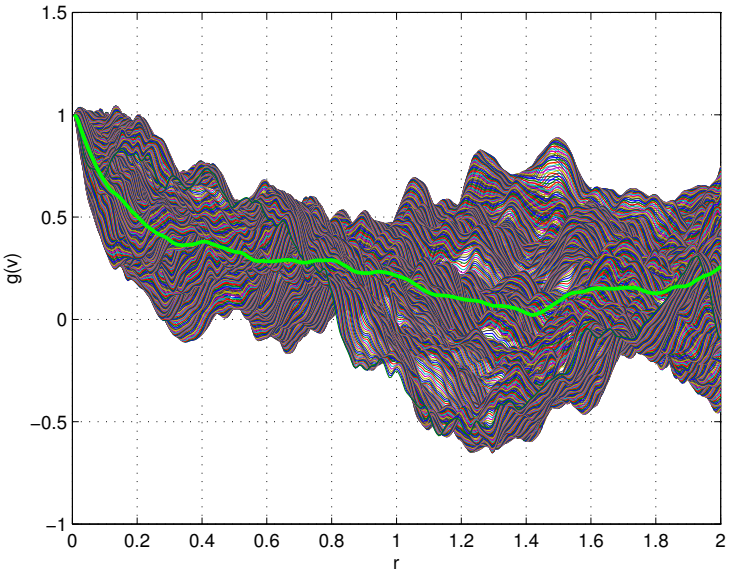

Figure 4.11: Transversal autocorrelation function $g(v)$.

In figures 4.12 and 4.13 (computed thanks to codes in Appendix C.5 and C.6) the two autocorrelation functions, longitudinal for v and transversal for u, are showed. The definitions here are:

$$\begin{aligned} f(v) &= < v(\mathbf{x} + \mathbf{e}_2 r, t)\, v(\mathbf{x}, t) > / < v(0)^2 >, \\ g(u) &= < u(\mathbf{x} + \mathbf{e}_2 r, t)\, u(\mathbf{x}, t) > / < u(0)^2 > . \end{aligned} \tag{4.2}$$

In this case, while decreasing as the autocorrelation functions we have seen before, the behavior of the transversal function may be observed more vividly: as we saw in the work of Comte-Bellot in figure 1.7 and in the one of Townsend in figure 1.9, the transversal autocorrelation function reach negative values for bigger r. Spurious effects and number samples affect instead the curve trend of $f(v)$.

Furthermore, thanks to Townsend work that we described in section 1.4.2 we may compare these results with ones in figures 1.8 and 1.9, hence stating that, due to the form of longitudinal autocorrelation functions that are not smooth but decrease rapidly, we are in presence of a wide range of eddies. This is confirmed, for example, from the flow visualizations provided in figure 2.4 and next.

To complete the discussion in figures 4.14 and 4.15 the autocorrelation functions for the grid at $z = 212$ are showed too. As we can see the evolution is slightly different from the one of the grid $z = 512$, but even though the trend is different for increasing values of r, we are more interested in what happens at small values of the

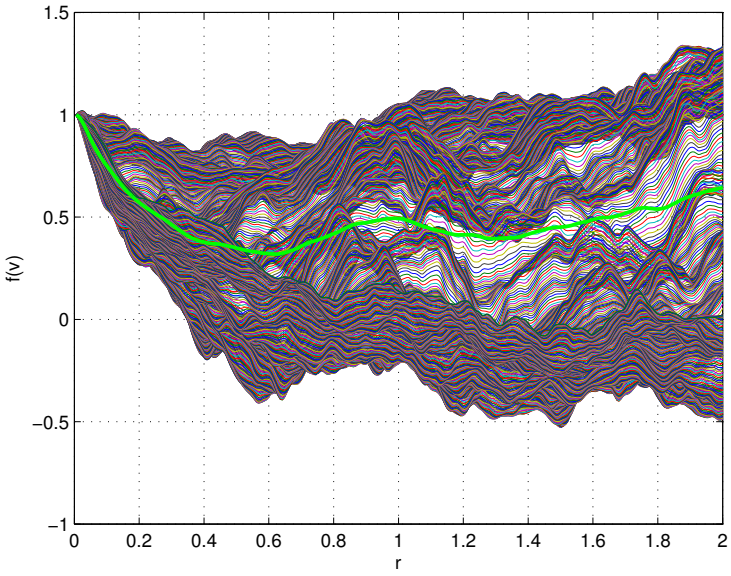

Figure 4.12: Longitudinal autocorrelation function $f(v)$.

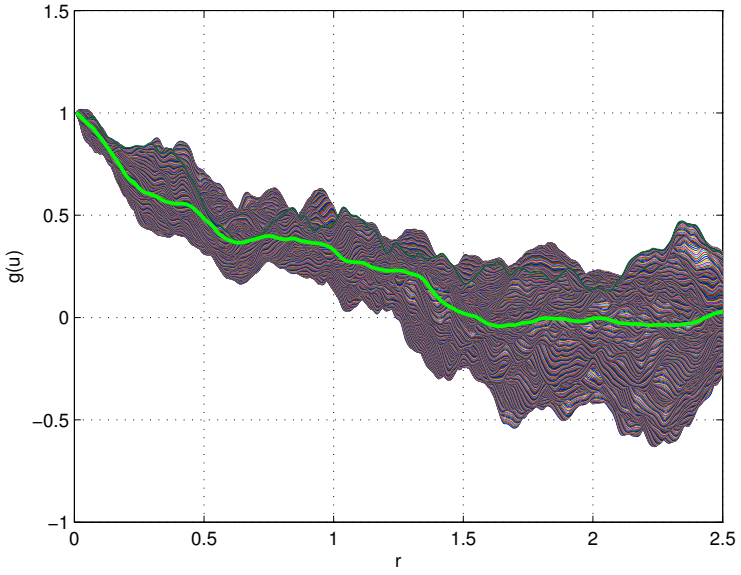

Figure 4.13: Transversal autocorrelation function $g(u)$.

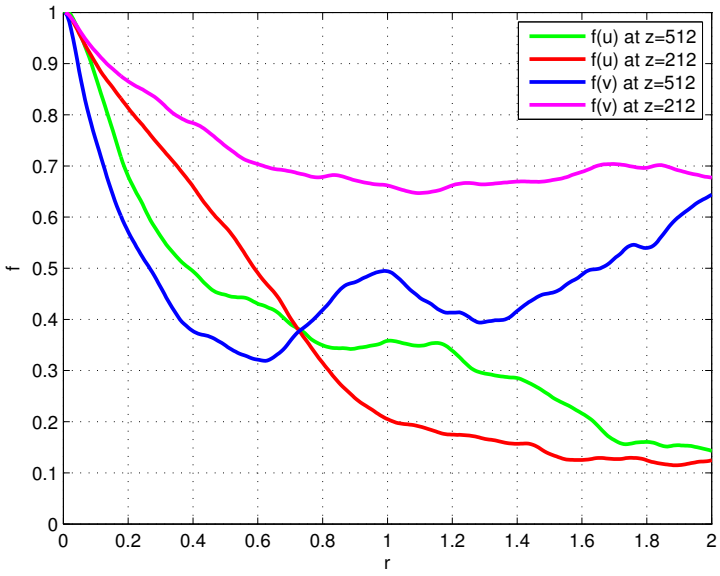

Figure 4.14: Longitudinal autocorrelation functions for $z = 212$ and $z = 512$.

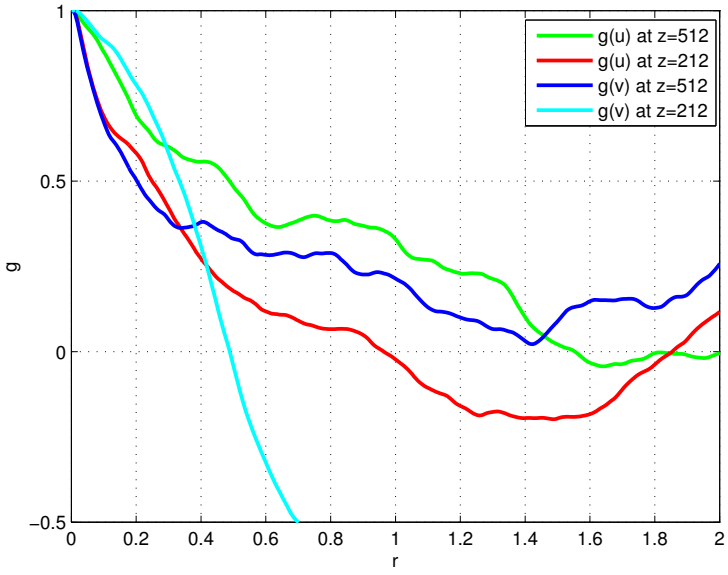

Figure 4.15: Transversal autocorrelation functions for $z = 212$ and $z = 512$.

distance because of the hypotheses of Kolmogorov: here the evolution of these functions is the same, hence the isotropy for the smaller scales of the field is confirmed once again. In order to achieve better results a comprehensive average of both grid should be performed.
The transversal autocorrelation functions $g(u)$ and $g(v)$ may be also calculated analytically thanks to the definition provided in equation 1.26 and code in Appendix C.7, that derives from the isotropic hypotesis and starts from the curves obtained for the longitudinal autocorrelation functions $f(u)$ and $f(v)$. The two figures 4.16 and 4.17 show that in the range of smaller r these analytically derived curves are similar to the ones provided in figures 4.13 and 4.11, while for bigger values of r they diverge and oscillate significantly due to the their definition that involves a derivative. The similarity applies especially for $g(v)$. Hence this definition is right for a very high number of samples and for smaller values of r, that is in the isotropic range.

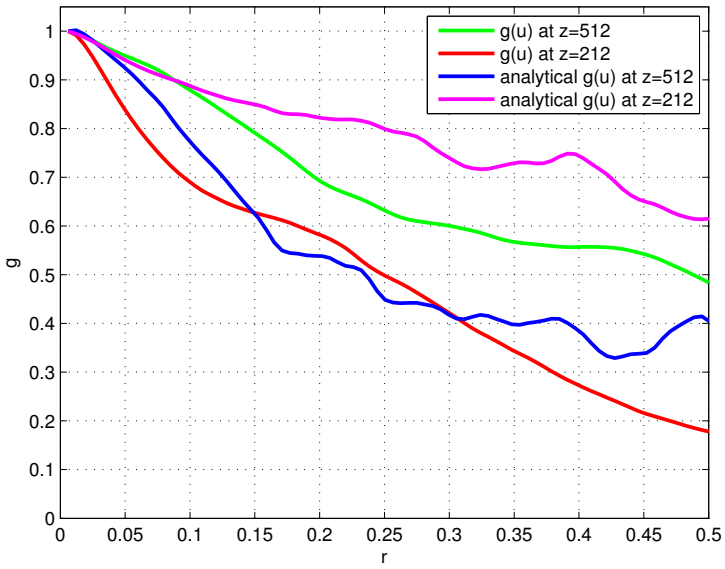

Figure 4.16: Transversal autocorrelation function $g(u)$, including the one derived from the analytical definition.

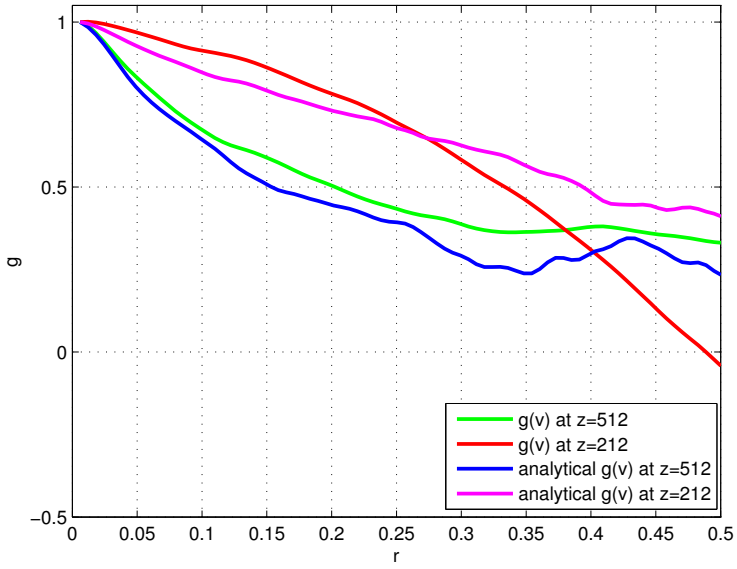

Figure 4.17: Transversal autocorrelation function $g(v)$, including the one derived from the analytical definition.

4.1.3 Energy Spectrum

The last tool that we used to analyze the isotropic turbulent flow is the spectrum of energy, that is how the energy is divided between the whole wavenumber range. We introduced the definitions in section 1.4.3.
In figures 4.18 and 4.19 the two one dimensional spectrum, derived from the R_{11} and R_{22}, are shown and confronted with the $-\frac{5}{3}$ Kolmogorov law for the inertial subrange. These results clearly support the provided scaling, and that is because we are taking into account an isotropic field. Furthermore it may be observed how the Kolmogorov scaling extends also to smaller values of the wavenumber: this is due to the forcing that acts on bigger scales.
The code used to compute this two one-dimensional spectra is shown in Appendix C.8.

In figure 4.20 the 3D spectrum is shown. This was computed thanks to code Appendix in C.9 that followed the definition provided in equation 1.34. The reader should take into account that this definition is an approximation due to the isotropic characteristic of the field and that contains a derivative inside: this is the main reason of the oscillations that the $E(k)$ curve has. To reduce this oscillations a bigger number of samples could have been used.

In figure 4.21 all the spectra computed are shown together along with the Kol-

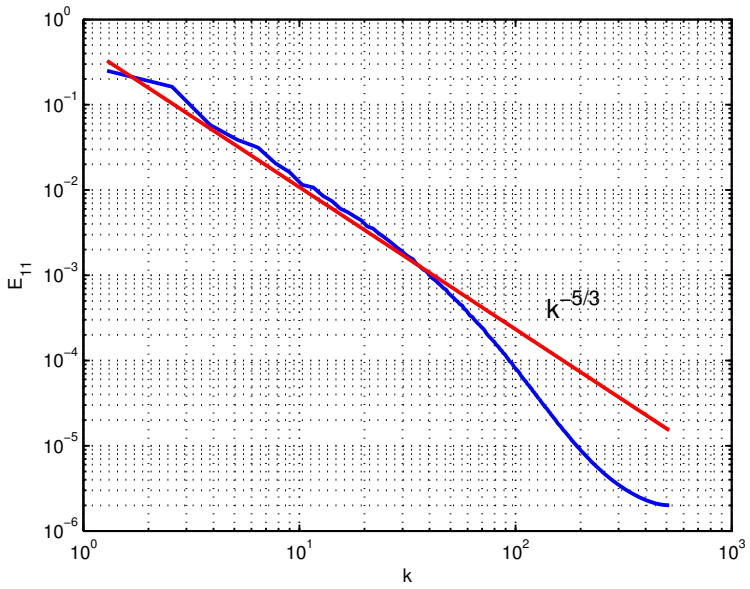

Figure 4.18: Spectrum derived from R_{11}, E_{11}.

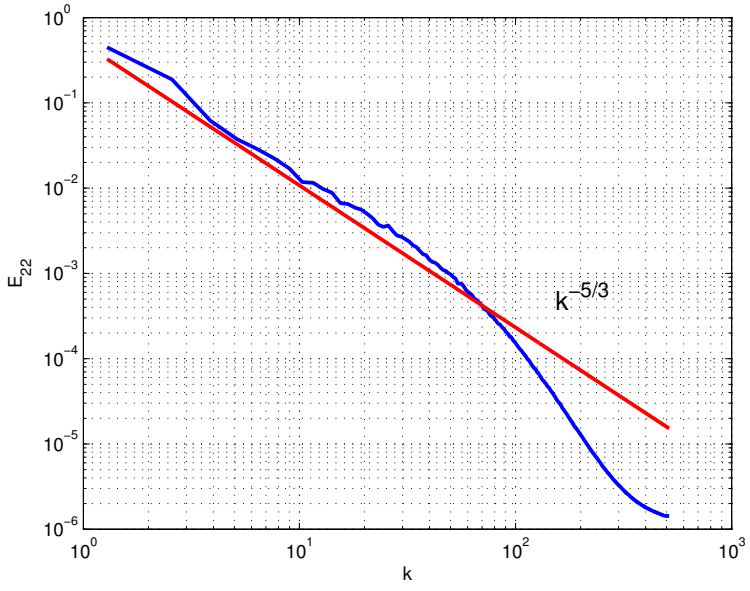

Figure 4.19: Spectrum derived from R_{22}, E_{22}.

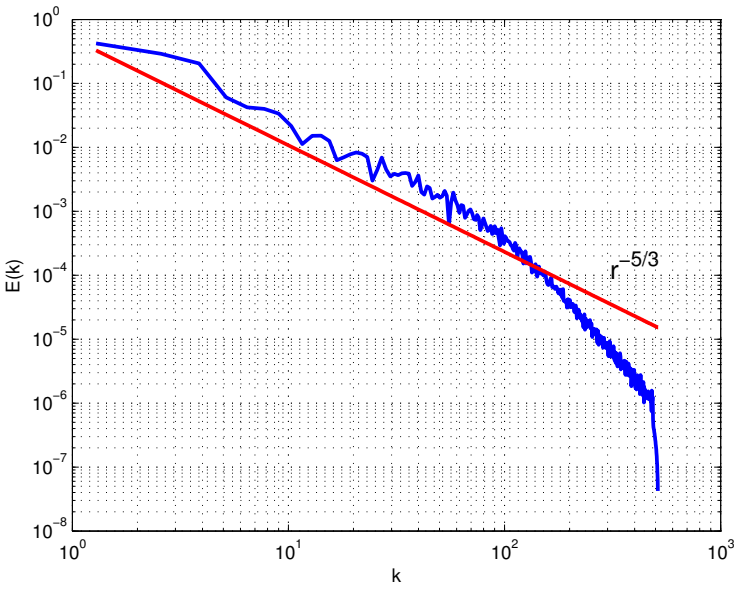

Figure 4.20: 3D Spectrum derived $E(k)$.

mogorov scaling, as a comparison with the figure 1.2, while in figure 4.22 the spectra computed thanks to the samples of the $z = 212$ grid are showed (the trend is obviously similar to the ones taken from the $z = 512$ grid).

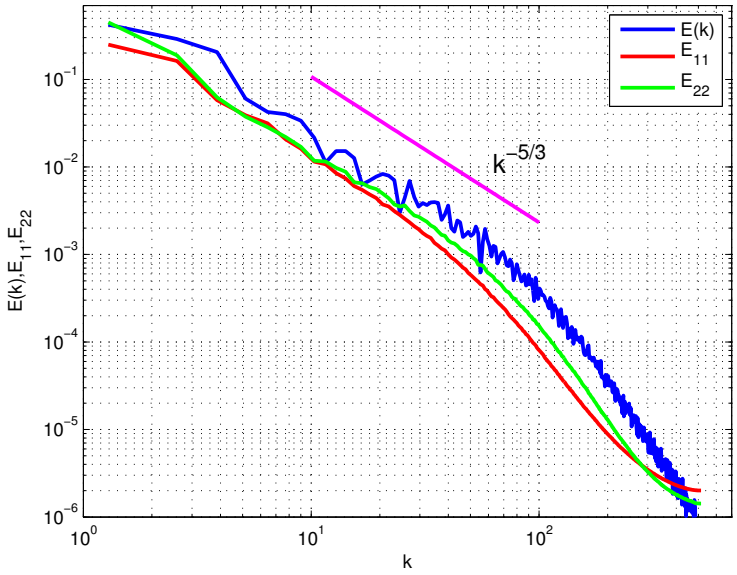

Figure 4.21: Spectra $E(k)$, E_{11}, E_{22} for the $z = 512$ grid.

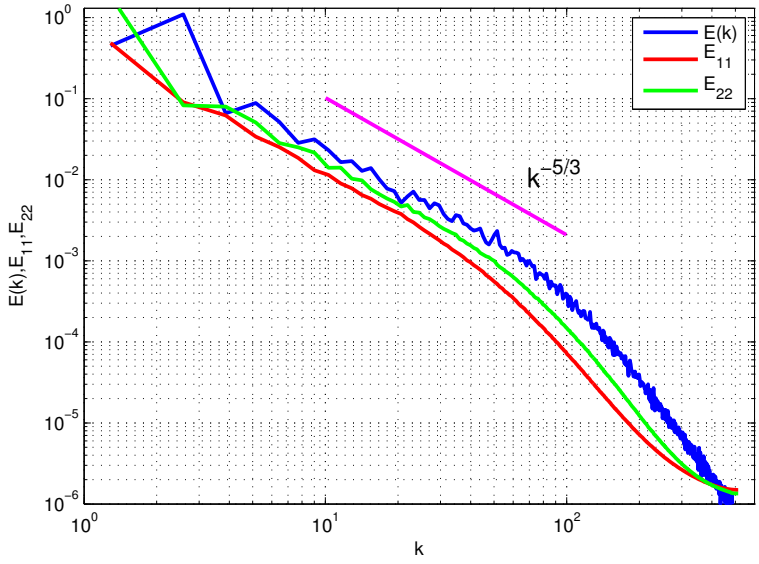

Figure 4.22: Spectra $E(k)$, E_{11}, E_{22} for the $z = 212$ grid.

4.2 A complex network analysis

In this section the key part of the work is going to be analyzed. We will look through a big number of results that we obtained, computed thanks to the definitions introduced in chapter 3.3 and a variety of codes that will be specified in the Appendix. First of all, a quick look at some figures will be given, introducing the graphics counterpart of the definitions of chapter 3.3; after that a deeper analysis of the most interesting structures that we found will be provided. We chose to display only the networks that showed interesting patterns or structures and to omit the remaining part, that consisted in a variety of networks similar to each other, in which spatial homogeneity was found.
As previously explained in the 3.4 "Building the network" section, every graph represents a circle of a ray of ~ 33 nodes, centered around a node located in one of the two 800x800 grids at $z = 512$ and $z = 212$. Every figure contains a colorbar that indicates the magnitude of the parameter that we are looking at. The networks are created starting from the time evolution of the kinetic energy values and computing their correlations, if not specified otherwise.

4.2.1 Differences between $\tau = 0.5$ and $\tau = 0.9$

During the process of building the network in code B.2 a value of the correlation limit had to be specified. This threshold of course affects directly the results in a way that may be understood better looking at the next figures.
First of all, the value of τ affects deeply the geometry of the network; in figures 4.23 and 4.24 the networks obtained for the two values of τ are shown. These circumference are centered in (200,600) and are located in the grid at $z = 512$. In these figures every point represents a node that has at least one link "switched on": of course the number of nodes (and consequently of links) in the figure 4.23 is a lot higher than the one of figure 4.24. In the case of a threshold $\tau = 0.5$ we have 9378 nodes and 1313722 links, while for $\tau = 0.9$ there are 3862 nodes and 38770 links. Geometry is different too: the network extends itself farther in the first case than in the second one. It's clear that, due to rapid decay of the correlation values, every node has nearer neighbors if higher is the value of the threshold value τ, and this reflects itself in the topology of the network.
Figures 4.25 and 4.26 show a comparison between the values of the degree centrality for the networks that we introduced in precedent figures. We remember that the degree centrality is the number of links that a node has, normalized over the total number of possible neighbors. The definition of the degree centrality was provided in equation 3.2 while its computational code is in Appendix D.1. The result of the comparison between the two limit values of correlations is obvious: while the location of the nodes with a higher value of the degree centrality in the network is

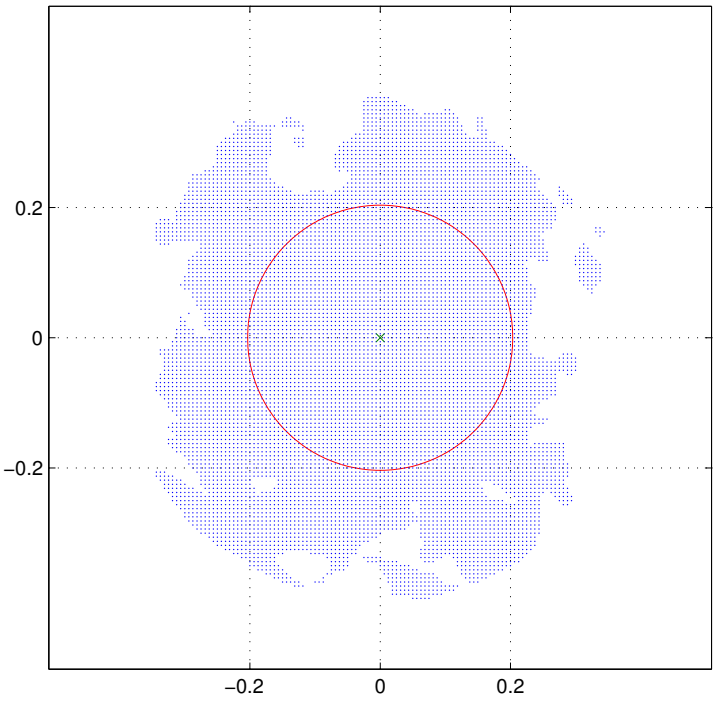

Figure 4.23: Network for the circumference centered in (200,600) at $z = 512$, $\tau = 0.5$.

almost the same, the structures of the most correlated nodes are more extended in space when τ is lower. The values (local values and mean value of the network) of the degree centrality are certainly different of some order of magnitude, and that is because choosing a value of $\tau = 0.9$ means to cut a whole range of nodes with a smaller correlation, hence the degree centrality is smaller too.
The weighted average topological distance is affected deeply by the value of τ. We introduced the definition of this quantity in equation 3.3 stating that the larger it is, the further is the node from the rest of the network: we mean distant in a topological sense, not in a geometrical one. The computational code used to evaluate the weighted average topological distance is shown in Appendix D.2.
Obviously a bigger value of the threshold τ, that means a smaller number of links for a particular node, implies a bigger weighted average topological distance at the same time: hence we should always expect bigger values of the weighted distance if the network shows low values of degree centrality. Figures 4.27 and 4.28 are shown as an example of the comparison between two networks at different τ for the weighted

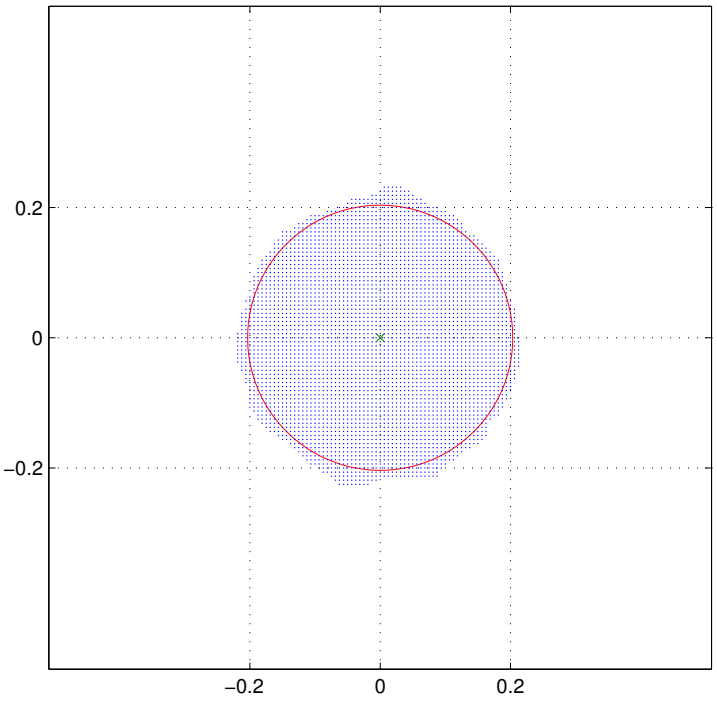

Figure 4.24: Network for the circumference centered in (200,600) at $z = 512$, $\tau = 0.9$.

average topological distance. It may be observed that the values reached are quite different, and the geometrical features are different too: the networks built with a value of $\tau = 0.9$ tend to show often a zone in which the values of the weighted distance are small and quite uniform, and this zone is located around the center of the network. This happens because, taking into account the threshold value $\tau = 0.9$, few links are still switched on and they connect nodes that are physically close: there is uniformity in space (values of the parameters vary slowly between close nodes) that interests the central part of the network. This behavior is evident especially in less connected networks, that is the one with small mean values of the degree centrality.

The same subject may be analyzed comparing the results of the betweenness centrality and local clustering coefficient, introduced in equations 3.7 and 3.5 respectively. The betweenness centrality, that is a value that indicates how much a node is a mediator for the information in a network (that is how many paths cross it), is computed with code in Appendix D.3, while the local clustering coefficient, that is the probability that two nodes linked with another are at their time adjacent,

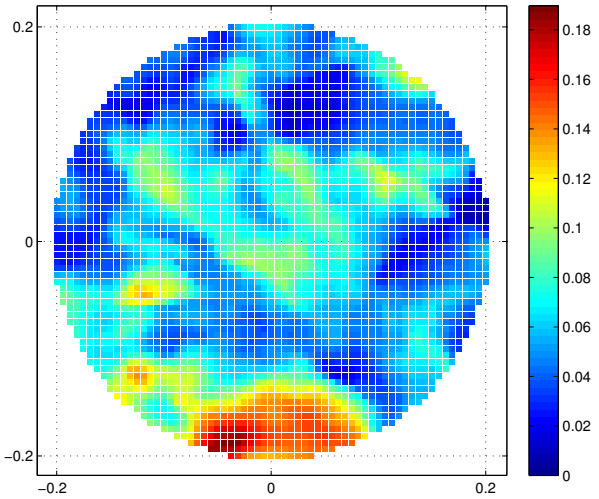

Figure 4.25: Comparison of the degree centrality for the (200,600) circumference at $z = 512$, $\tau = 0.5$.

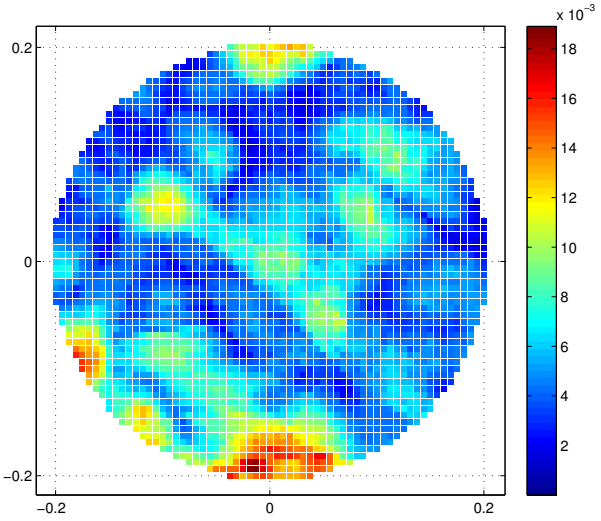

Figure 4.26: Comparison of the degree centrality for the (200,600) circumference at $z = 512$, $\tau = 0.9$.

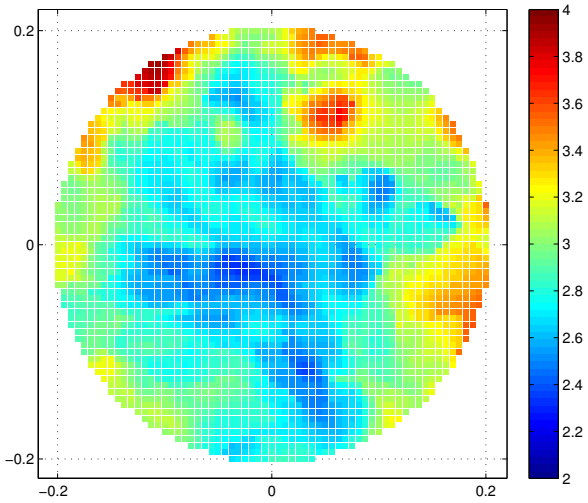

Figure 4.27: Comparison of the weighted average topological distance for the (200,600) circumference at $z = 512$, $\tau = 0.5$.

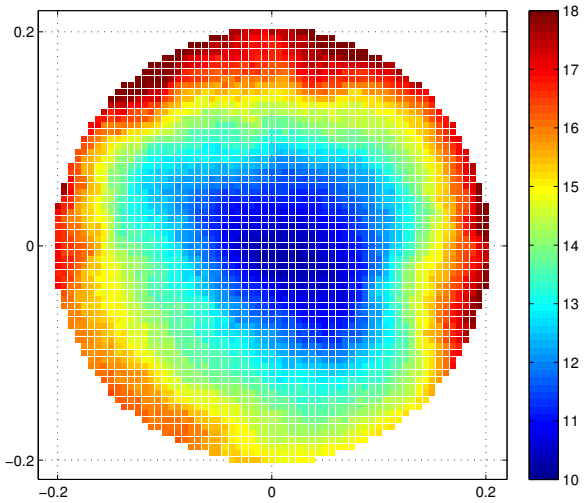

Figure 4.28: Comparison of the weighted average topological distance for the (200,600) circumference at $z = 512$, $\tau = 0.9$.

is computed with the code shown in Appendix D.4.
Figure 4.29 shows the betweenness centrality for the $\tau = 0.5$ network of the same circumference we have analyzed before for the other parameters, while 4.30 considers the same network but for $\tau = 0.9$. It stands out that in case of a lower correlation

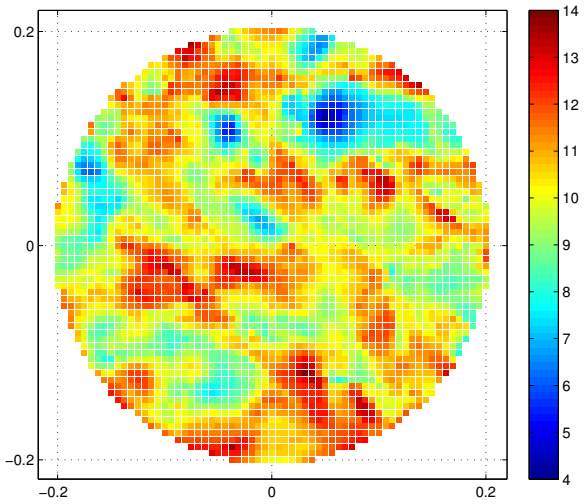

Figure 4.29: Comparison of the betweenness centrality for the (200,600) circumference at $z = 512$, $\tau = 0.5$.

limit a pattern is well defined, and on the contrary for $\tau = 0.9$ very spotted and heterogeneous values are present: this typical behavior will stand out expecially for network with smaller values of degree centrality, as we will see later. Changing the value of τ from 0.5 to 0.9 the values' range stays the same, but of course there are fewer nodes that have bigger values of betweenness centrality. These nodes are important in the network because they generally show high values of degree centrality and smaller values of weighted average topological distance, too.

The same concept applies also for the local clustering coefficient shown in figures 4.31 and 4.32. We already explained how the concepts of betweenness centrality and local clustering are in a certain sense similar: we expect in fact that if a node has a high value of the betweenness centrality, it has a high local clustering coefficient, too. This behavior happens in general for the major part of nodes. This similarity doesn't apply correctly if we focus on the change of the correlation limit values τ: we observed before how a node with a high value of the betweeness centrality for $\tau = 0.5$ will probably have a high value for $\tau = 0.9$. This is not always meant to happen if we consider the local clustering coefficient because, by increasing the threshold

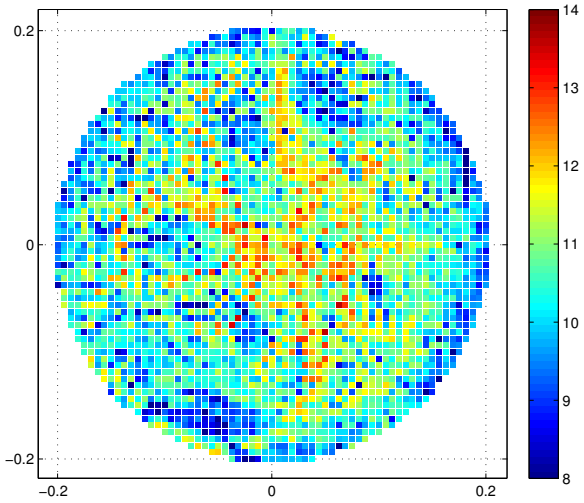

Figure 4.30: Comparison of the betweenness centrality for the (200,600) circumference at $z = 512$, $\tau = 0.9$.

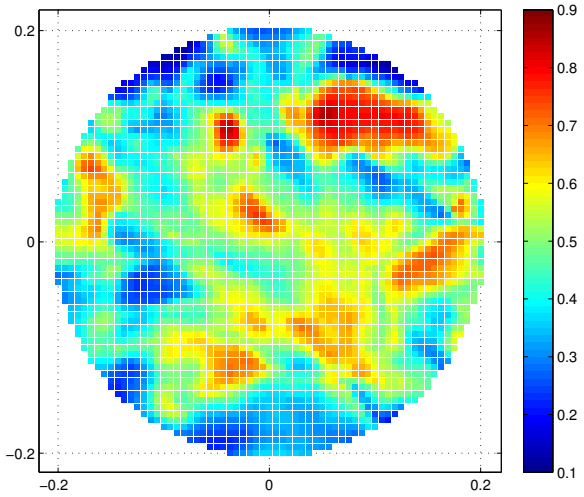

Figure 4.31: Comparison of the local clustering coefficient for the (200,600) circumference at $z = 512$, $\tau = 0.5$.

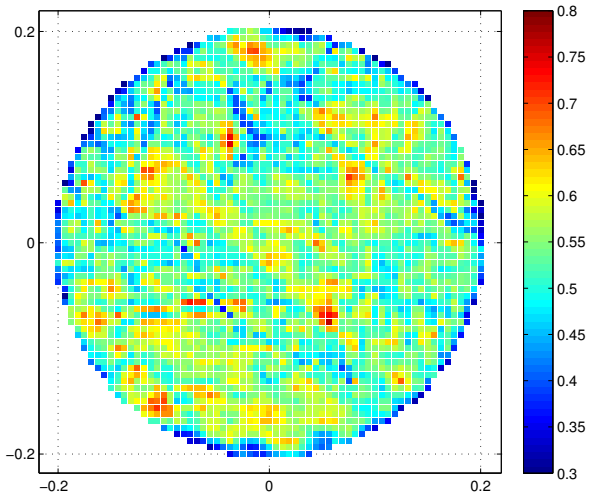

Figure 4.32: Comparison of the local clustering coefficient for the (200,600) circumference at $z = 512$, $\tau = 0.9$.

value, we cut a lot of links in a way that if two nodes adjacent to a third one were neighbors, they may not be anymore linked to each other. As a consequence, the $\tau = 0.9$ network does not substantially maintain any of the patterns revealed by the $\tau = 0.5$ network.
Taking a closer look at these figures we see that the same pixelated pattern that we observed in figure 4.30 stands out also in the case of local clustering coefficient: this is a general behavior observed for networks with smaller degree centrality values.
From now on the major part of this analysis will focus on the case of $\tau = 0.9$, hence we are going to consider only the strongest correlations between the nodes of the network.
In the next sections a quick look to some of the most interesting structures found in the two grids $z = 212$ and $z = 512$ will be given; after that the focus will be on one of these structures that will be analyzed deeply.

4.2.2 Analysis of the grid $z = 212$

As already explained in section 3.4, two 800x800 grids were downloaded in order to find some interesting patterns in the domain. The two grids were analyzed in their integrity, creating 80 cuts circa that consisted in 80 circumferences for each section. In this chapter, some of the most interesting circumferences of the section

$z = 212$ will be analyzed mainly in terms of the degree centrality and the weighted average distance, which are the most meaningful measures of the network theory. A sketch of the location of the networks analyzed in this section is provided in figure 4.33. Out of ~ 80 circumferences that were analyzed at this z, we found at least 10 networks with interesting patterns and high values of the degree centrality; the rest of the circumferences, instead, showed homogeneity in space and small values of the degree centrality.

Figure 4.34 shows a network centered around the node (230,230) in the grid $z = 212$.

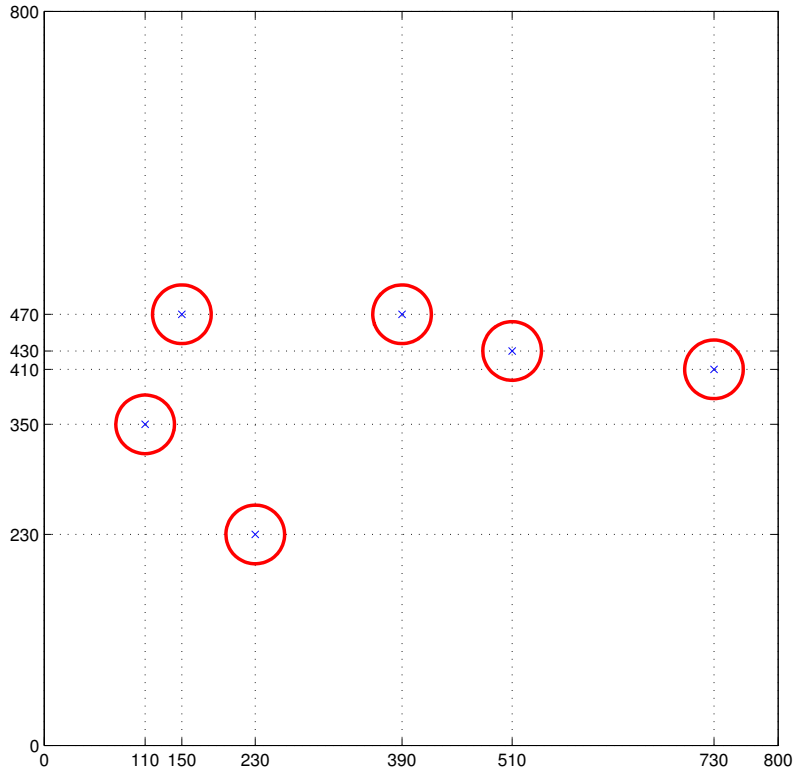

Figure 4.33: Sketch of the circumferences analyzed at $z = 212$

The degree centrality is two order of magnitude higher than the one showed in the example provided in figure 4.26, whereas still lower than some values that we found in our analysis. The streaky pattern that we observe in this figure is typical of networks with a low-medium value of the degree centrality, and it goes against what we would have expected in a case of isotropic field: one of the brightest results in

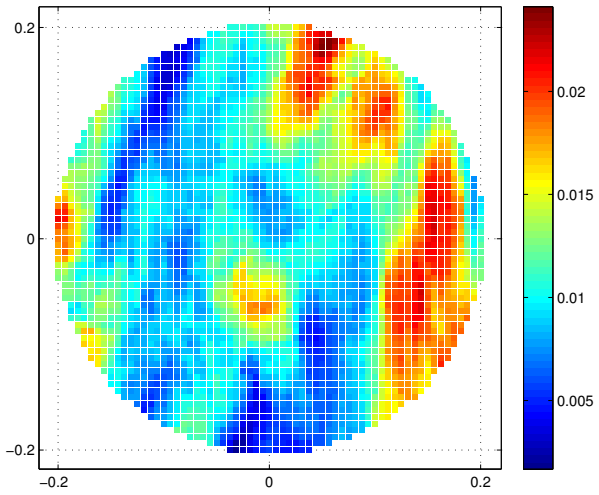

Figure 4.34: Degree centrality for the circumference centered in (230,230) at $z = 212$, $\tau = 0.9$.

our project is that there isn't isotropy in the network's pattern, even if the flow considered is an isotropic one.

Figure 4.35 shows, for the same network, the evolution of the weighted average topological distance. Due to the fact that the values of the degree centrality are not particularly high, the values of the weighted topological distance are of course high, because every node tends to be topologically far from the rest of the network.

The streaky pattern that we observed in figure 4.34 is confirmed in figure 4.36 where another network with degree centrality values similar in order of magnitude is shown. The streaks break down when there are few nodes with high values of degree centrality and the rest of the network with quite low and uniform values, as shown in figure 4.37, where a circumference centered in (150,470) displays a low mean degree centrality value.

While exploring the $z = 212$ grid we found some interesting structures that consisted of nodes with a high degree centrality value: these nodes are referred to as *supernodes*. This is the case of the circumference centered in (110,350) that has $N = 4172$ nodes and 376685 active links: this network is showed in figure 4.38 while the degree centrality plot is in figure 4.39. This network is interesting because is one of the few having small structures consisting of supernodes, while the major part of the networks with high values of degree centrality show structures contained in a range of 10-40 nodes circa.

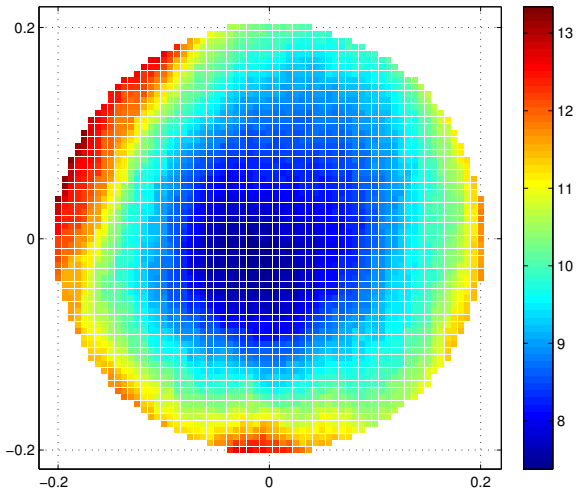

Figure 4.35: Weighted average topological distance for the circumference centered in (230,230) at $z = 212$, $\tau = 0.9$.

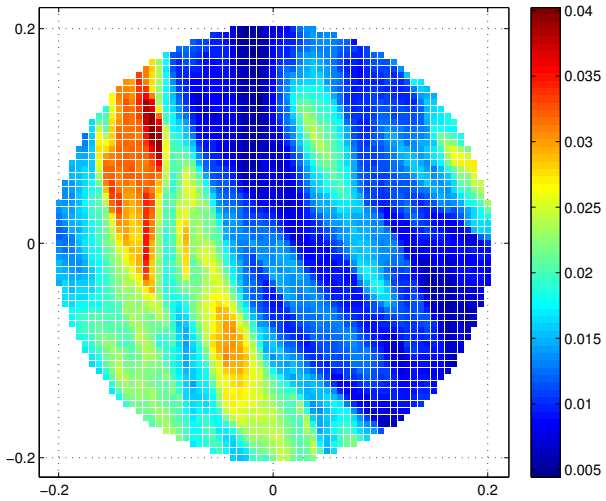

Figure 4.36: Degree centrality for the circumference centered in (390,470) at $z = 212$, $\tau = 0.9$.

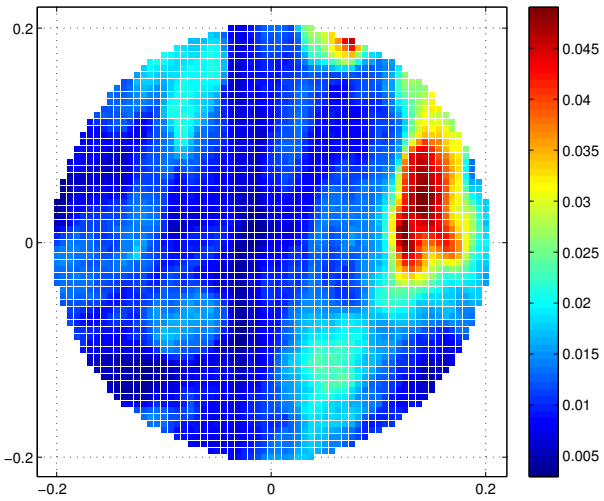

Figure 4.37: Degree centrality for the circumference centered in (150,470) at $z = 212$, $\tau = 0.9$.

In figure 4.40 the supernode (120,344) is highlighted along with its active links. This is one of the nodes with a higher value of the degree centrality in the network showed in figures 4.38 and 4.37. Its degree centrality is 0.1172, while its active links are 551. Once again it may be observed that there is not an isotropic behavior in the trend of the correlations, hence the links are distributed differently in every direction.
In figure 4.41 a node with smaller degree centrality (0.0365 with 172 links) is showed. Comparing the two graphs 4.40 and 4.41 we see that the directional biases are lost when we pass from a node with an high degree centrality value to a node with a smaller one: that said, the fewer the links of a node are, the more similar the correlations in every direction are.

Figure 4.42 shows the weighted average topological distance for the same network: as we expected, the smaller values of this parameter are located in the nodes corresponding to higher values of degree centrality (supernodes shown in fig. 4.39 are represented by dark blue regions in fig. 4.42). In this network the weighted average topological distance in medially smaller than in other networks.

For the sake of completeness the graphs for betweenness centrality and local clustering coefficient are showed too (figures 4.43 and 4.44). The patterns are more defined than the ones of figures 4.30 and 4.32, and that is because the network has high values of degree centrality.

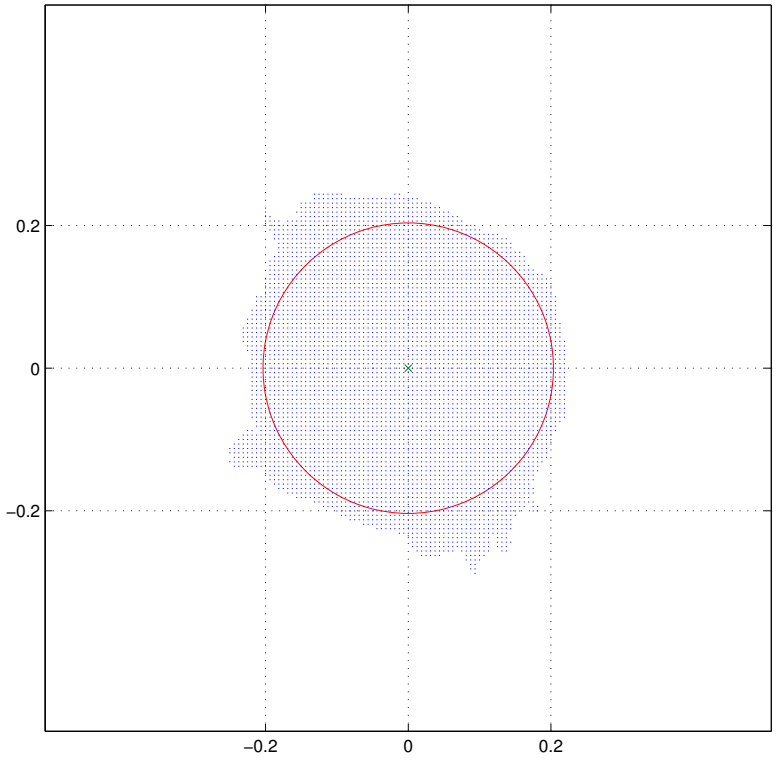

Figure 4.38: Network for the circumference centered in (110,350) at $z = 212$, $\tau = 0.9$.

Taking a closer look to the betweenness centrality, we observe that there is not a particular connection between the structures present here with the ones of the degree centrality graph: an exception has to be done to the structure around the node (120,344) that we highlighted in figure 4.40. This structure has high values of the betweenness centrality and at the same time high values of degree centrality too, whereas showing small values of local clustering coefficient.
In this network, on the contrary of what happens in other networks with smaller values of degree centrality, the similarity between the patterns of the betweenness centrality and local clustering coefficient doesn't stand out.

While exploring the $z = 212$ grid, different structures were found showing a wide range of degree centrality values. In figure 4.46 a structure with very high values of degree centrality is shown: this network (figure 4.45) consists of 6600 nodes and 1629967 links, and represents an agglomeration of highly correlated nodes, probably

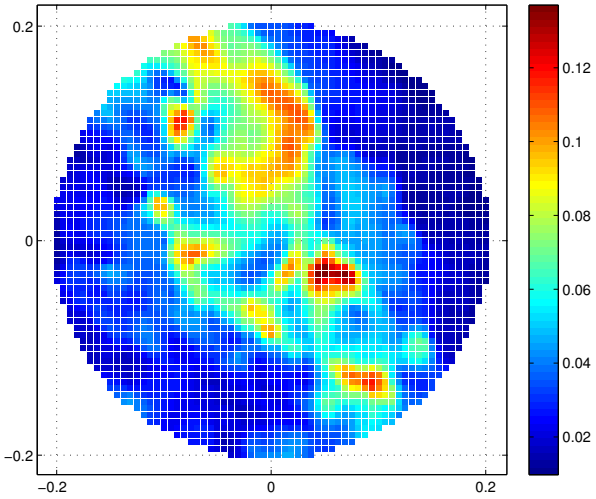

Figure 4.39: Degree centrality for the circumference centered in (110,350) at $z = 212$, $\tau = 0.9$.

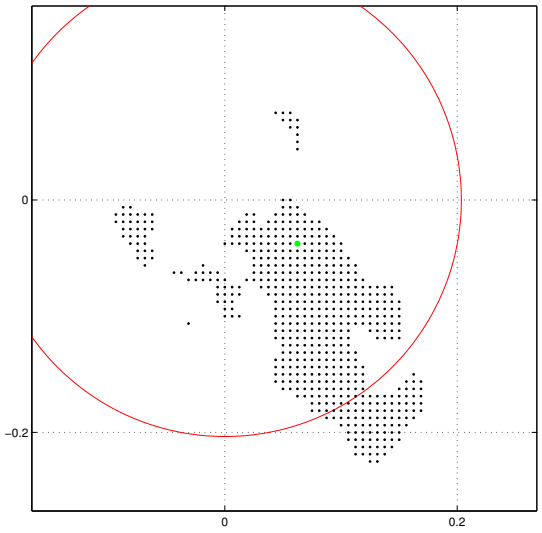

Figure 4.40: Node (120,344) and its 551 active links. $z = 212$, $\tau = 0.9$.

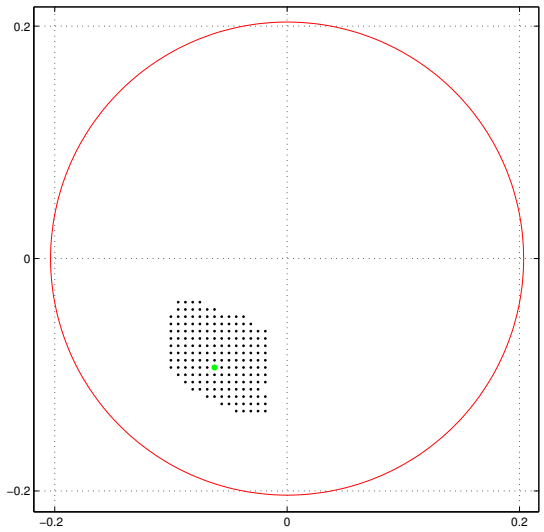

Figure 4.41: Node (100,335) and its 172 active links. $z = 212$, $\tau = 0.9$.

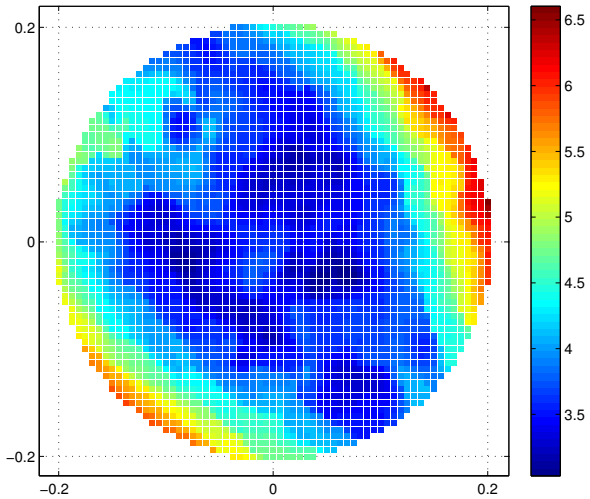

Figure 4.42: Weighted average topological distance for the circumference centered in (110,350) at $z = 212$, $\tau = 0.9$.

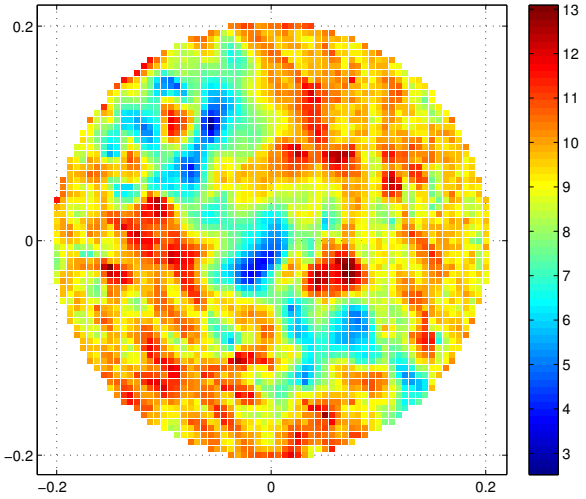

Figure 4.43: Betweenness centrality for the circumference centered in (110,350) at $z = 212$, $\tau = 0.9$.

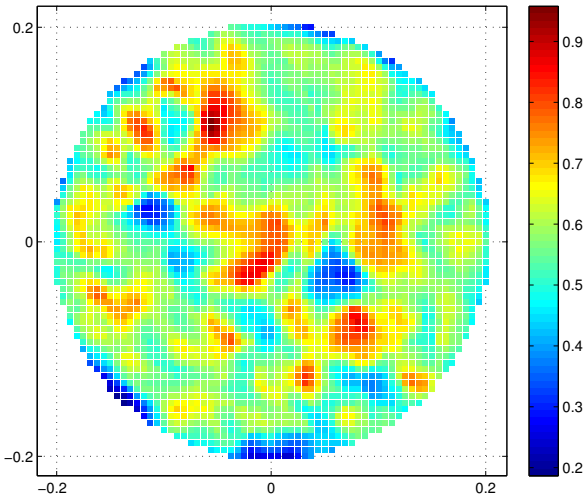

Figure 4.44: Local clustering coefficient for the circumference centered in (110,350) at $z = 212$, $\tau = 0.9$.

due to a presence of a very energetic eddy. Figure 4.47 shows the central node of the network, that is the one located at (510,430). This node has a degree centrality value of 0.2731 and a number of active links of 1802. This is definitely one of the supernodes with the highest value of the degree centrality in the domain.

In figure 4.48 another interesting structure of the $z = 212$ grid is shown: this

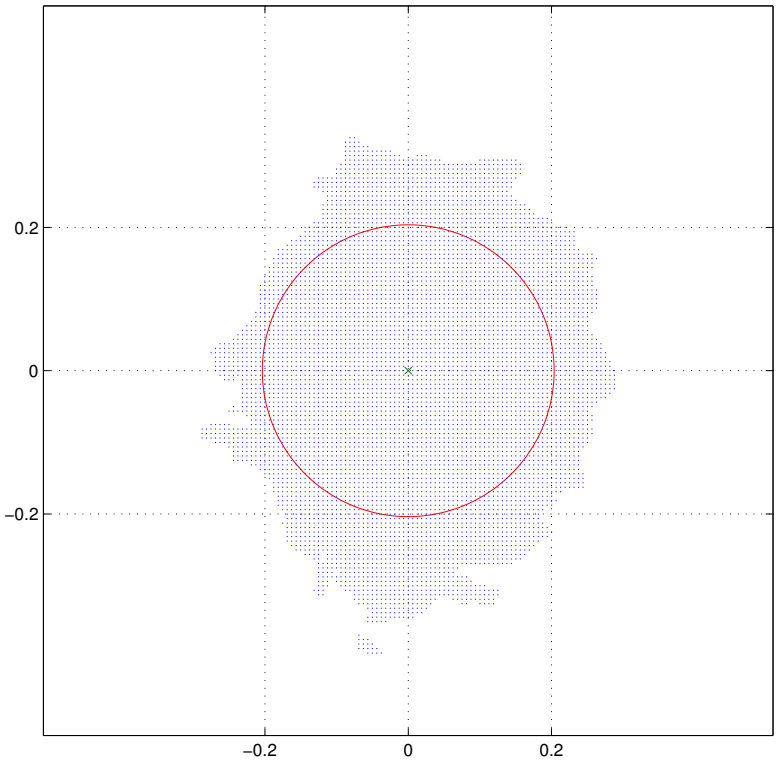

Figure 4.45: Network for the circumference centered in (510,430) at $z = 212$, $\tau = 0.9$.

time we are in presence of a big structure with great heterogeneity in the degree centrality values. For this network the supernode located in (727,416) is shown in figure 4.49. Once again we observe that there isn't isotropy in the correlation trend.

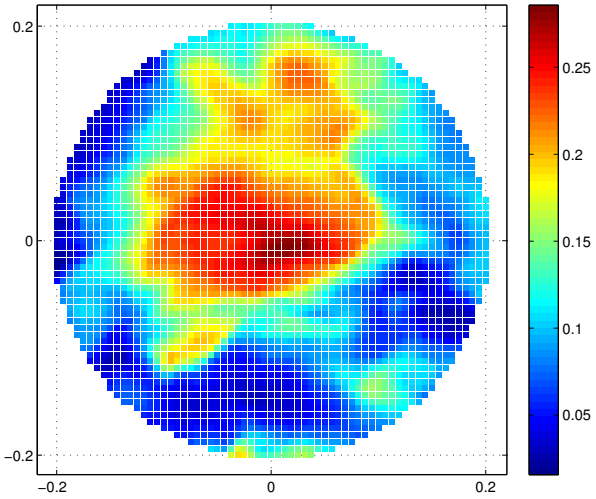

Figure 4.46: Degree centrality for the circumference centered in (510,430) at $z = 212$, $\tau = 0.9$.

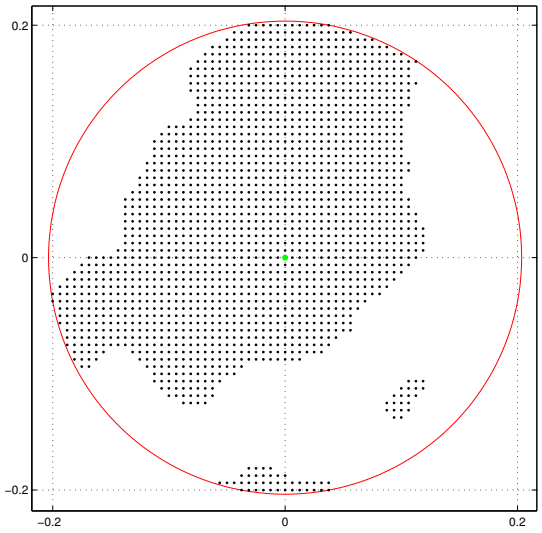

Figure 4.47: Node (510,430) and its 1802 active links. $z = 212$, $\tau = 0.9$.

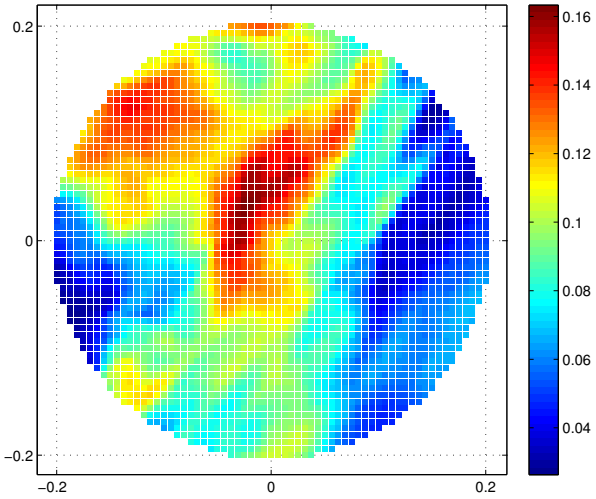

Figure 4.48: Degree centrality for the circumference centered in (730,410) at $z = 212$, $\tau = 0.9$.

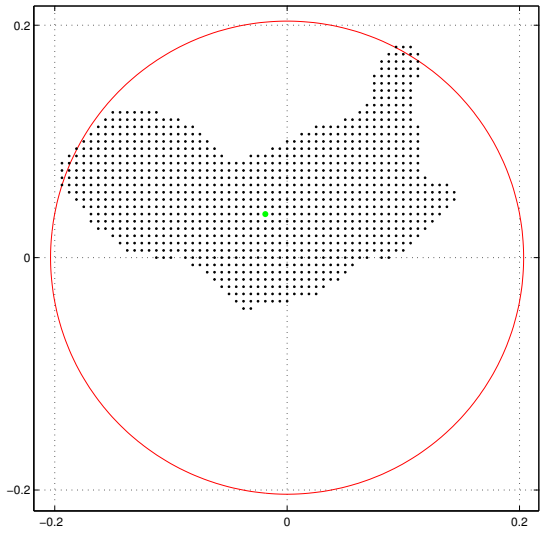

Figure 4.49: Node (727,416) and its 1032 active links. $z = 212$, $\tau = 0.9$.

4.2.3 Analysis of the grid $z = 512$

The $z = 512$ was explored in the same way that we did for the $z = 212$. Several interesting structure, of course different in dimensions, shape and magnitude, were found in this grid: out of 80 cuts we found circa ten interesting networks, hence confirming the trend of the $z = 212$ grid. In this section an overview of the main results will be provided while in the next section a deeper analysis of a particular network located in this grid will be given.
First of all, as previously did for the $z = 212$ grid, a graphical sketch of the location of the circumferences here analyzed is provided in figure 4.50.

Figures 4.51 and 4.52 show the degree centrality and weighted average topological

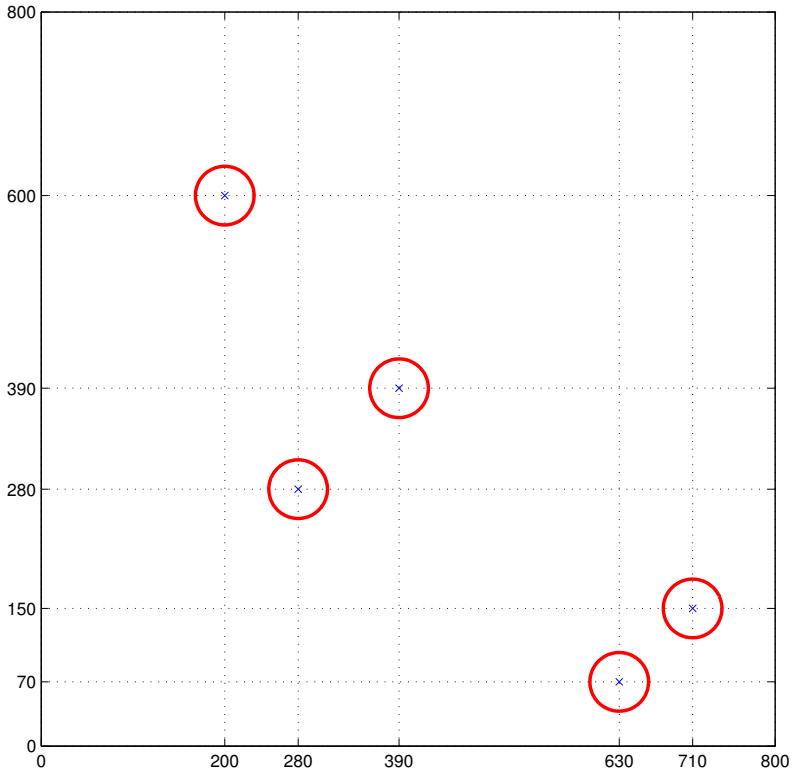

Figure 4.50: Sketch of the circumferences analyzed at $z = 512$

distance for a circumference centered in the node (390,390). In this configuration there aren't any interesting structures with high values of degree centrality, and of course the values of the weighted average topological distance is medially high

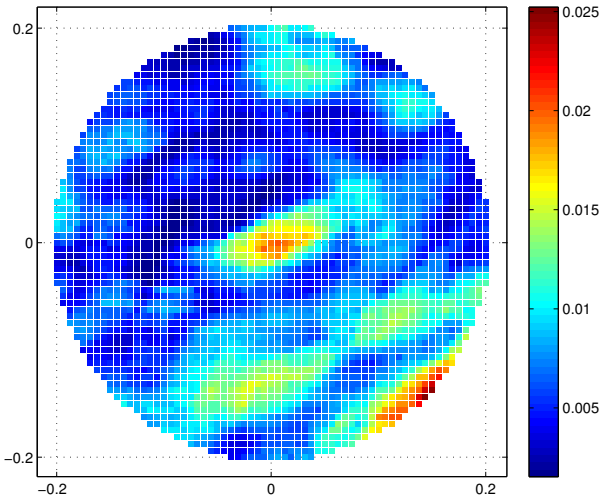

Figure 4.51: Degree centrality for the circumference centered in (390,390) at $z = 512$, $\tau = 0.9$.

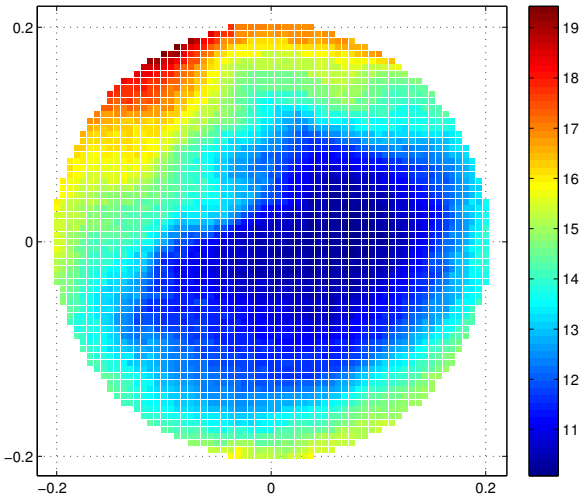

Figure 4.52: Weighted average topological distance for the circumference centered in (390,390) at $z = 512$, $\tau = 0.9$.

and quite uniform: due to the fact that the nodes are not strongly correlated, the weighted average topological distance is high. Even though we are in presence of a network with small values of correlations, the link between the plot of the degree centrality and the one for the weighted average topological distance stands out: in figure 4.52 in fact there is a zone in which the values of the parameters are low, and that corresponds to the zone in figure 4.51 where there is an agglomeration of nodes with higher degree centrality compared with the rest of the network.
A more correlated network is shown in figure 4.53. In this case the values of the degree centrality are higher because we have a network with 3962 nodes and 92448 links. The weighted average topological distance is showed as well in figure 4.54: the values are obviously smaller than the circumference located in (390,390). Also in this case the correspondence between the graph of the degree centrality and the one of the weighted average topological distance is straightforward: the structure that has the higher values of the degree centrality in figure 4.53 has the smaller values of weighted average topological distance in figure 4.54.
Comparing the values of the network centered in (710,150) with the ones of the network seen before and centered in (390,390) we observe once again that when a network tends to show high values of the degree centrality, it shows small values of the weighted average topological distance too: the network centered in (390,390) has a peak in the degree centrality value of 0.025 while the one centered in (710,150) has a peak of 0.045 and consequently the values of the weighted average topological centrality have a minimum value of 10 in the (390,390) network and of 6 in the (710,150) one.

One of the more correlated nodes of the network centered in (710,150) is showed in figure 4.55. This node can't be classified as a supernode if we compare it with other nodes of the domain, because it has a degree centrality value of 0.04 and a number of active links equal to 159. These values, despite being the highest in this network, are small in comparison with other network's ones.

As we did for the $z = 212$ grid, we provide also in this case an example of a highly correlated network that is the one centered in the node (630x70), that has a number of nodes N=4462 and 416573 links. Figure 4.56 represents the degree centrality, which shows a structure with degree centrality values of ~ 0.2, while figure 4.57 depicts the weighted average topological distance. The range of values of the weighted average topological distance is small, and that's due to the high degree centrality of the network: as already seen for other networks the nodes that have higher values of the degree centrality tend to assume small values of the weighted average topological distance. For the sake of completeness the graphs for the betweenness centrality and local clustering coefficient are reported, too (figures 4.58 and 4.59). Taking a closer look at the figures, we may observe that the nodes with an high degree centrality value tend to show higher values of the betweenness centrality and local clustering coefficient. Even though the major part of the supernodes show high values of both

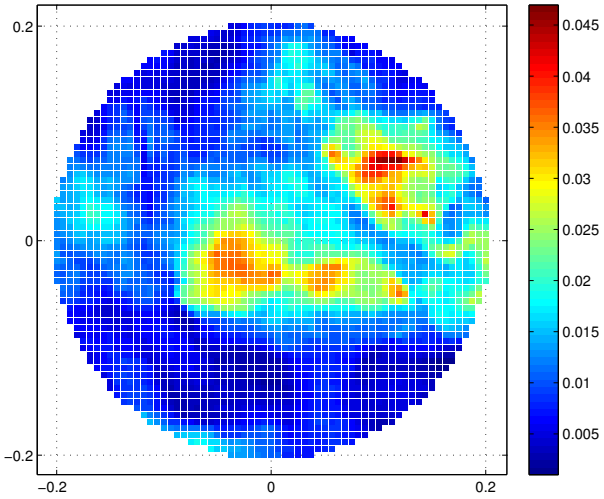

Figure 4.53: Degree centrality for the circumference centered in (710,150) at $z = 512$, $\tau = 0.9$.

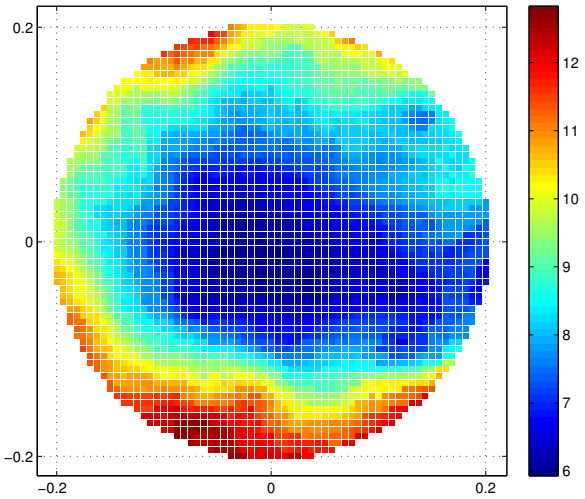

Figure 4.54: Weighted average topological distance for the circumference centered in (710,150) at $z = 512$, $\tau = 0.9$.

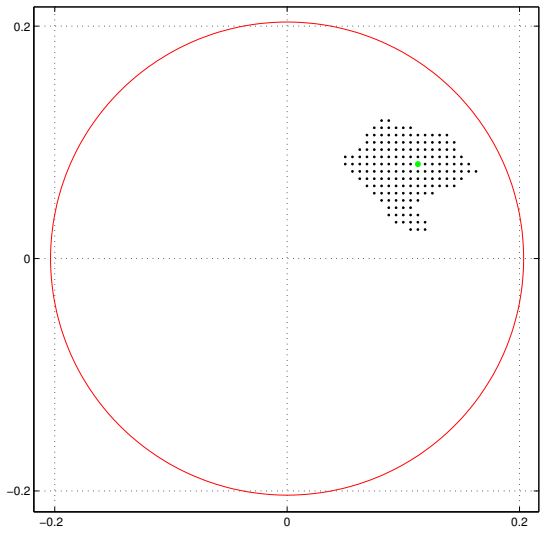

Figure 4.55: Node (728,163) and its 159 active links. $z = 512$, $\tau = 0.9$.

the betweenness centrality and local clustering coefficient, a small degree centrality value doesn't exclude a priori a high value of the two parameters.
Figure 4.60 shows the active links for the node (638,53): the number of links are 911 while the value of the degree centrality is 0.2042. Once again we observe how links spread out differently in every direction.

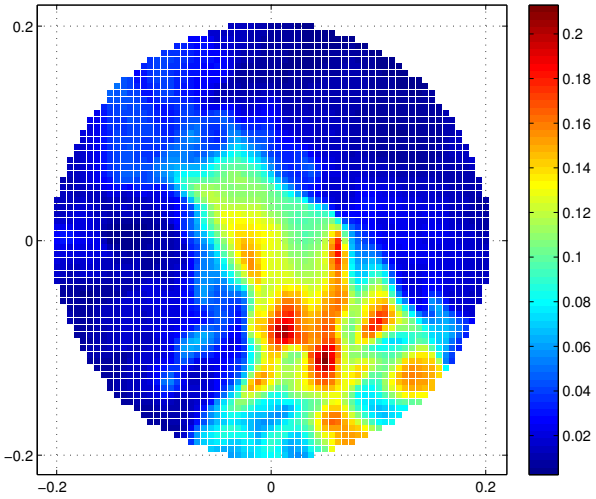

Figure 4.56: Degree centrality for the circumference centered in (630,70) at $z = 512$, $\tau = 0.9$.

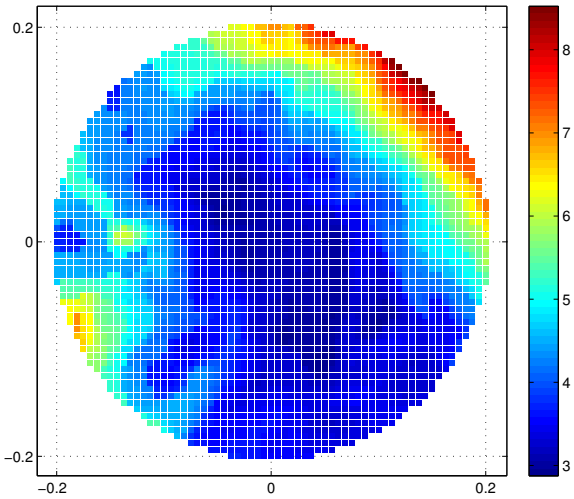

Figure 4.57: Weighted average topological distance for the circumference centered in (630,70) at $z = 512$, $\tau = 0.9$.

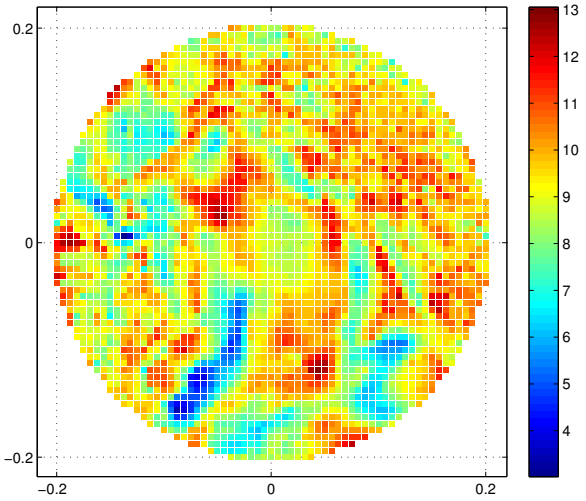

Figure 4.58: Betweenness centrality for the circumference centered in (630,70) at $z = 512$, $\tau = 0.9$.

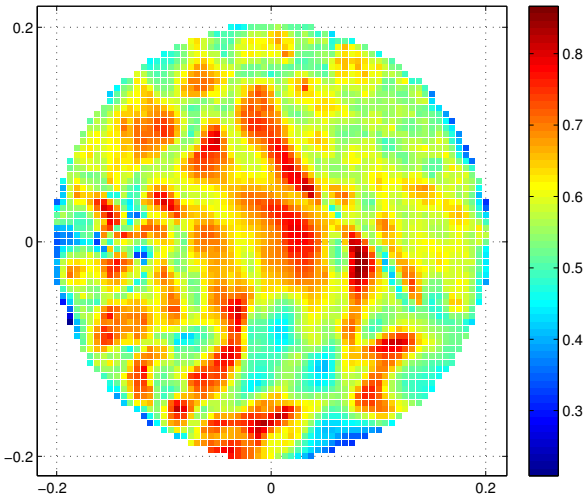

Figure 4.59: Local clustering coefficient for the circumference centered in (630,70) at $z = 512$, $\tau = 0.9$.

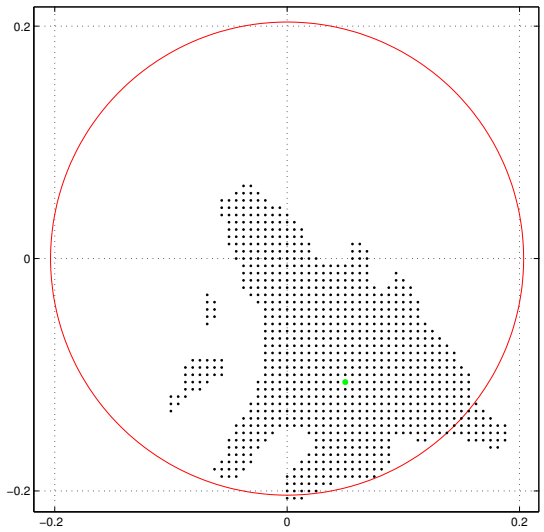

Figure 4.60: Node (638,53) and its 911 active links. $z = 512$, $\tau = 0.9$.

4.2.4 A deeper look at the circumference centered in (280,280) at $z = 512$

In this section a closer look at one of the most interesting networks that we found in our work will be given. Different results will be provided: beyond all the parameters that we introduced in the previous chapters a different analysis will be done, including several cuts at different sections and networks for the three components of velocity.
The circumference centered in (280,280) has already been introduced in section 3.4, where it was taken as an example for the process of building the network. Figures 3.3 and 3.4 showed the network for both the two values of the threshold τ: the first network with $\tau = 0.5$ has $N = 10451$ nodes and $n = 5688943$ links while the one with $\tau = 0.9$ consists of $N = 4848$ nodes and $n = 379581$ links. The same circumference was also showed in figures 2.10, 2.11, 2.12, 2.13 and 2.14 where the time evolution of the kinetic energy was plotted.

The graphs for the degree centrality are showed in figures 4.61 and 4.62: the first one shows the degree centrality for the threshold value $\tau = 0.5$, while the second one is for $\tau = 0.9$. Comparing the two figures we observe that the values of the degree centrality are of course smaller in the second network; the pattern is different too, the threshold $\tau = 0.9$ cuts a huge part of the correlated nodes, hence the main structure in the center of the network is less extended in space. Figures 4.63 and

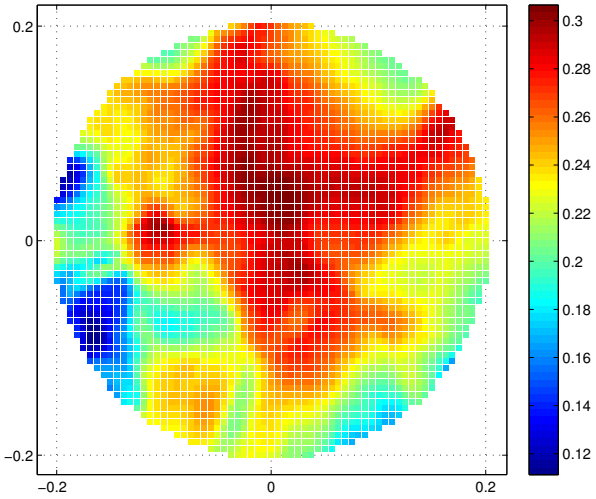

Figure 4.61: Degree centrality for the circumference centered in (280,280) at $z = 512$, $\tau = 0.5$.

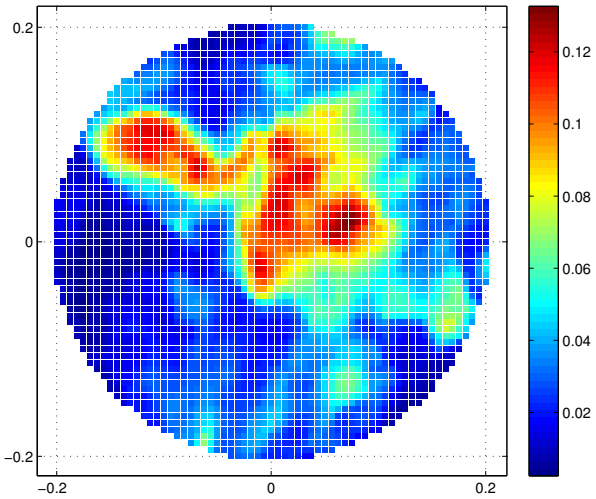

Figure 4.62: Degree centrality for the circumference centered in (280,280) at $z = 512$, $\tau = 0.9$.

4.64 show the links of the central node of the network. In case of threshold $\tau = 0.5$ the central node has a degree centrality value of 0.28736 with 3003 active links, while with $\tau = 0.9$ the degree centrality value is 0.10583 and the number of active links is 513. Furthermore, we observe how the links around the node (280,280) for the threshold value $\tau = 0.9$ are located in a way that resembles the streak already seen for the degree centrality plot, that is the one in figure 4.62.

From now on, the analysis of this circumference will be done assuming a value of

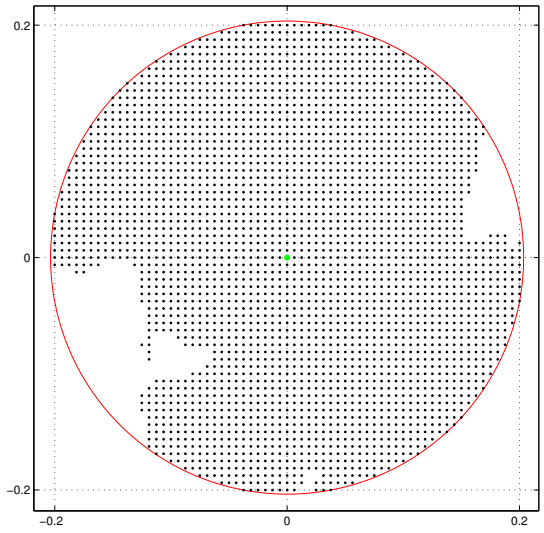

Figure 4.63: Node (280,280) and its 3003 active links. $z = 512$, $\tau = 0.5$.

the threshold $\tau = 0.9$ because we are interested in highlighting the stronger correlations between nodes. Taking a look at figure 4.61 in fact we observe how the greatest part of the nodes of the network has high and similar values of the degree centrality, hence we are not able to capture any well-defined structure.
Figure 4.65 shows the weighted average topological distance, the trend of which is similar to the ones seen in precedent chapter: the nodes with high degree centrality tend to show smaller values of the weighted average topological distance (dark blue regions). Figures 4.66 and 4.67 represent the betweenness centrality and the local clustering coefficient, respectively: these measures don't show a particular trend even if we expect having higher values of betweenness centrality and local clustering coefficient where we are in presence of supernodes.

As previously anticipated, a different analysis may be done in order to overcome the limitation that comes from taking into account only two-dimensional grids. We

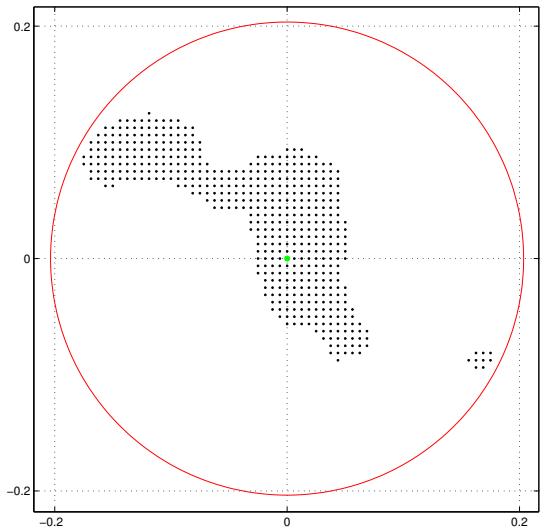

Figure 4.64: Node (280,280) and its 513 active links. $z = 512$, $\tau = 0.9$.

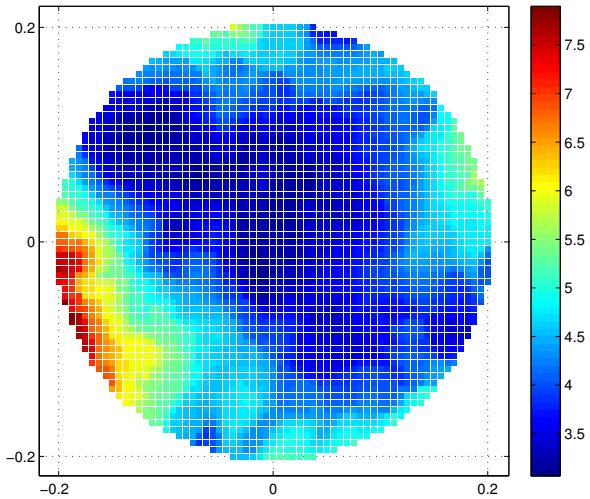

Figure 4.65: Weighted average topological distance for the circumference centered in (280,280) at $z = 512$, $\tau = 0.9$.

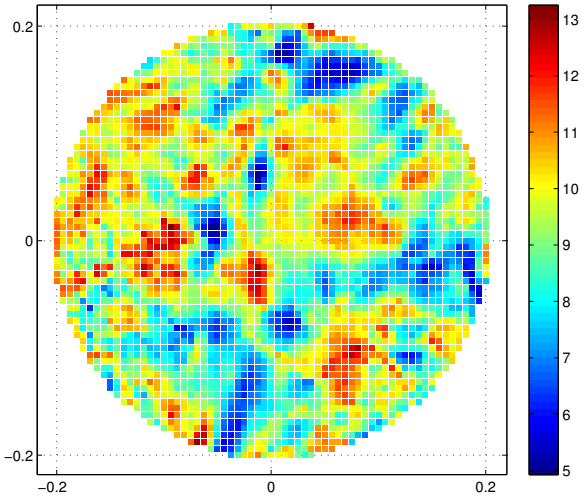

Figure 4.66: Betweenness centrality for the circumference centered in (280,280) at $z = 512$, $\tau = 0.9$.

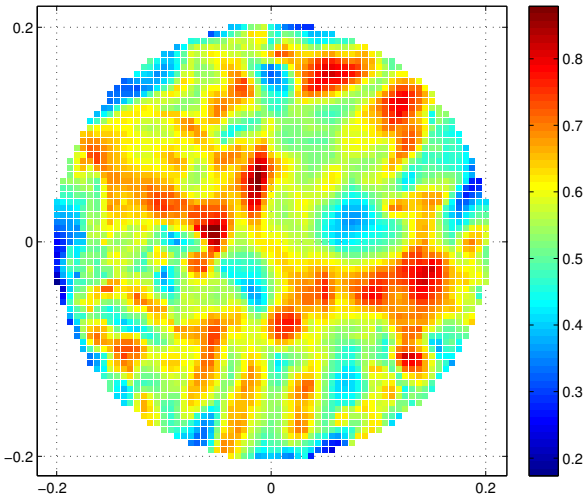

Figure 4.67: Local clustering coefficient for the circumference centered in (280,280) at $z = 512$, $\tau = 0.9$.

downloaded 8 different 400x400 grids, distanced of 5 nodes along the z direction: the cuts were done at z = 492,497,502,507,512,517,522,527,532. For each of these grids a network centered in the (280,280) node was built, and the degree centrality was computed in order to follow the evolution of the structure with high correlated nodes in the z direction.
Figures from 4.68 to 4.76 show the evolution of the structure in space along the z direction; the figures are scaled with the same values of the degree centrality found in these networks, in order to capture in the best way the evolution of the pattern of interest. We observe that the structure extends in the z direction for a number of nodes similar to the ones in the x-y plane, while maintaining the same values of the degree centrality throughout the z cuts. Starting from the cut at z = 527 in figure 4.75 the structure disappears, while another big and correlated structure rises in the lower part of the network. Even though the field is isotropic, the presence of these patterns located at different sections may be an indication of the existence of eddies which have a 'lifetime' bigger, or at least equal, than the integral scale one, that is comparable to the duration of the stored data of the database.

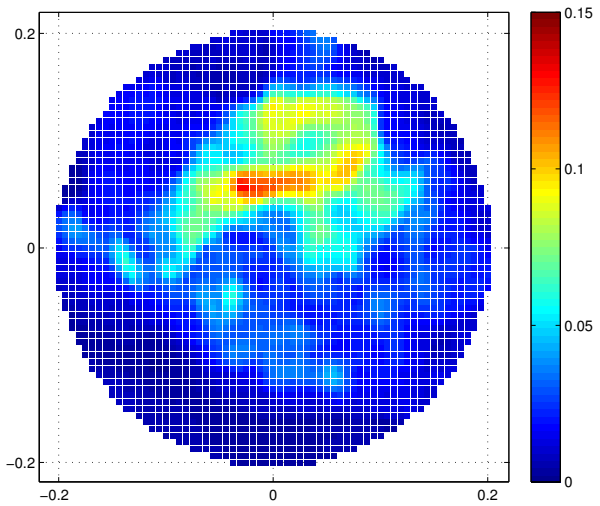

Figure 4.68: Degree centrality for the circumference centered in (280,280) at z = 492, $\tau = 0.9$.

Up to now we analyzed networks based on the time evolution of the kinetic energy value; in order to achieve a better description of the phenomenology, the same analysis may be pursued for all the three components of the velocity. We

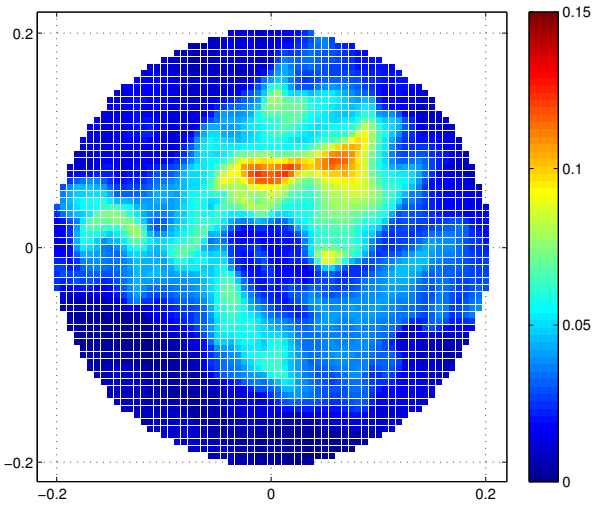

Figure 4.69: Degree centrality for the circumference centered in (280,280) at $z = 497$, $\tau = 0.9$.

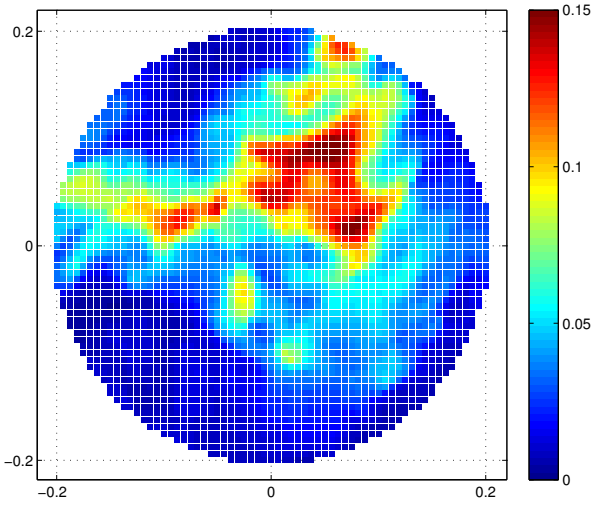

Figure 4.70: Degree centrality for the circumference centered in (280,280) at $z = 502$, $\tau = 0.9$.

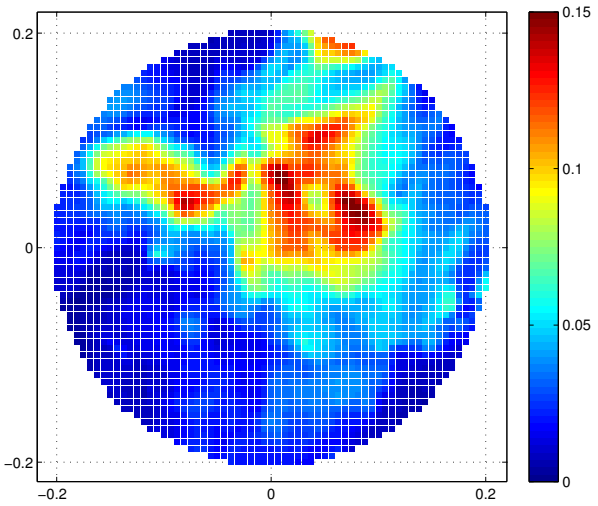

Figure 4.71: Degree centrality for the circumference centered in (280,280) at $z = 507$, $\tau = 0.9$.

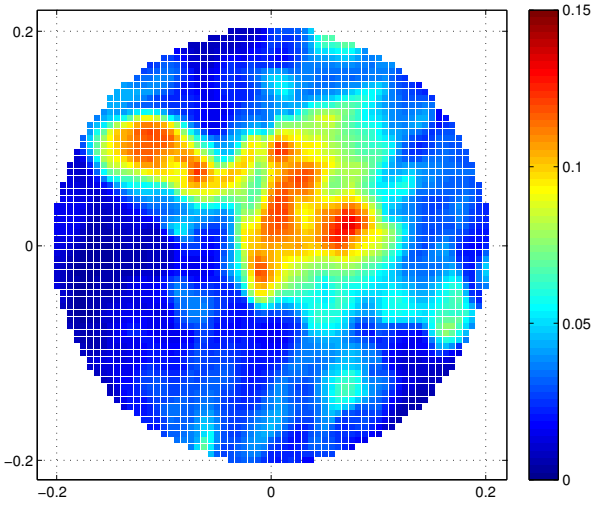

Figure 4.72: Degree centrality for the circumference centered in (280,280) at $z = 512$, $\tau = 0.9$.

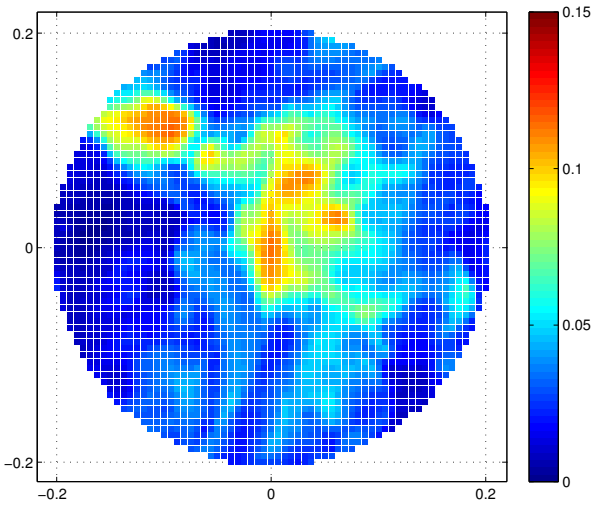

Figure 4.73: Degree centrality for the circumference centered in (280,280) at $z = 517$, $\tau = 0.9$.

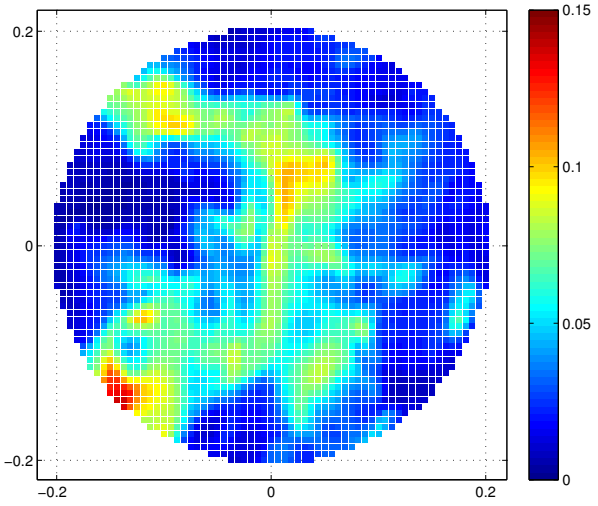

Figure 4.74: Degree centrality for the circumference centered in (280,280) at $z = 522$, $\tau = 0.9$.

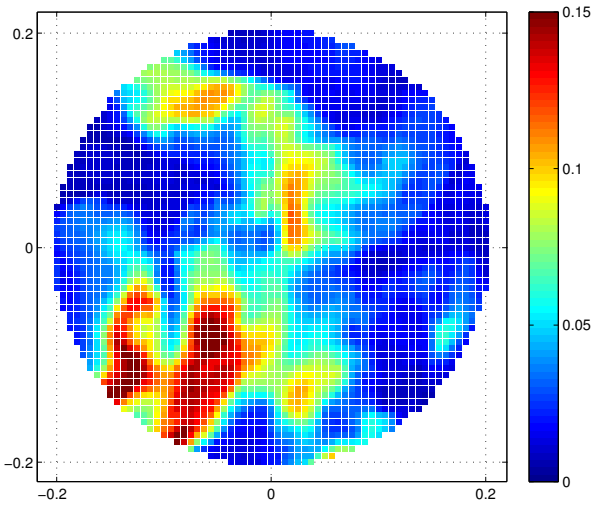

Figure 4.75: Degree centrality for the circumference centered in (280,280) at $z = 527$, $\tau = 0.9$.

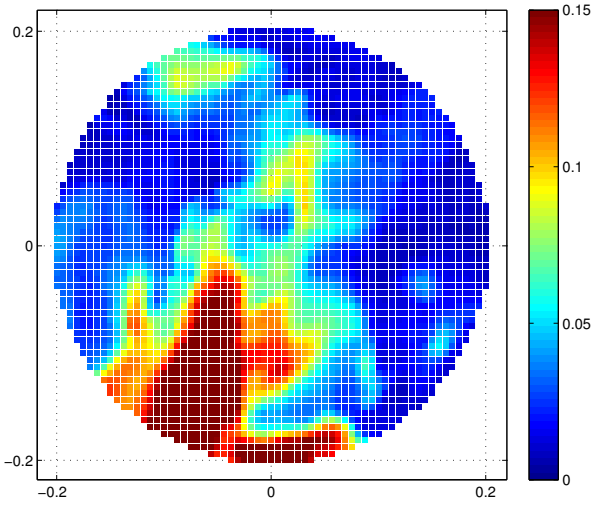

Figure 4.76: Degree centrality for the circumference centered in (280,280) at $z = 532$, $\tau = 0.9$.

built these types of network for several circumferences that we found interesting when analyzing the energy correlations, and we didn't find a particular connection between the networks for the energy and the ones for the three velocity components: here only the results for the circumference centered in (280,280) at $z = 512$ are showed (figures 4.77, 4.78 and 4.79). We scaled the figure with the same values of the degree centrality, in order to have a better understanding of the evolution. In this case it may be observed that the component which seems to resemble the morphology of the kinetic energy network in figure 4.62 is the third one, w (figure 4.79).

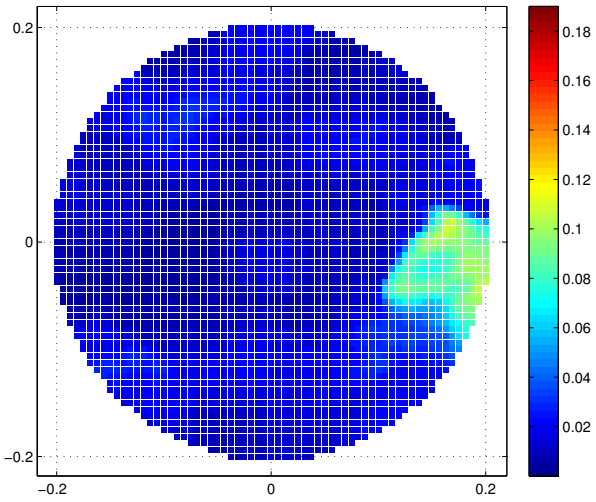

Figure 4.77: Degree centrality of the u component of velocity for the circumference centered in (280,280) at $z = 512$, $\tau = 0.9$.

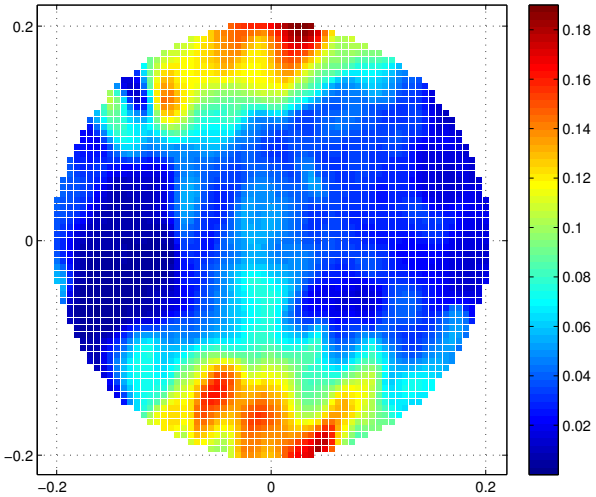

Figure 4.78: Degree centrality of the v component of velocity for the circumference centered in (280,280) at $z = 512$, $\tau = 0.9$.

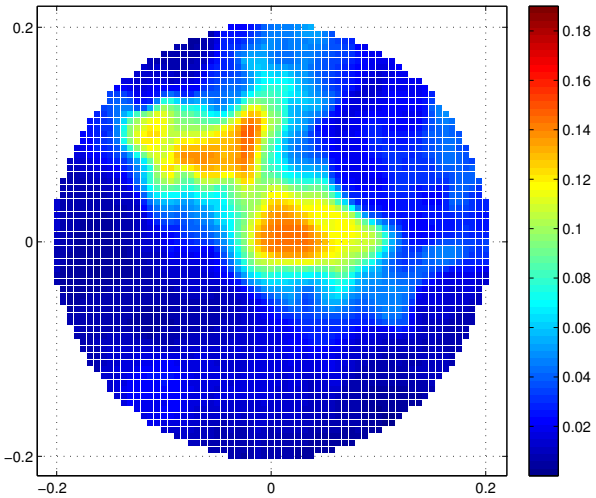

Figure 4.79: Degree centrality of the w component of velocity for the circumference centered in (280,280) at $z = 512$, $\tau = 0.9$.

4.2.5 Power-law distribution of the degree centrality

In order to conclude our analysis some graphs showing the power-law distribution of the degree centrality will be provided. A network is called *scale-free* when power-laws of degree distribution have the same functional form at all scales. Real networks are often scale-free and have exponents ranging between -2 and -3 ([19], [40]). These networks have a typical behavior, that is few of the nodes are highly connected to the others while a great amount of nodes are barely connected to each other. However, because of the finite size of the network, data can have a rather strong intrinsic noise. To smooth the fluctuations generally present in the tails of the distribution, it is often verified if the cumulative distribution function, $P_k(k)$, presents a power-law behavior.
Here we will show some graphs containing the exceedance probability of the node degree, that is $1 - P_k(k)$, along with a scaling having exponent equal to -2 observable in the intermediate range of degree centrality value, where the greatest part of the nodes is located. These graphs are referred to several networks with different patterns and different values of the degree centrality: for a better comparison, the results the degree centrality of each of the chosen networks will be showed as well.
Figure 4.80 shows the degree distribution for the main network that we analyzed in our work, that is the (280,280) one located at the grid $z = 512$. The power-law scaling with exponent -2 is observed for a restricted range of k values. A different scenario appears in figure 4.81 in which another circumference with different pattern and different values of the degree centrality is analyzed. Here the power-law scaling (-2) involves about a decade of degree centrality values.

In figures 4.84 and 4.86 two networks of the $z = 212$ grid with quite different characteristics are shown, while in figures 4.83 and 4.85 their degree distributions are plotted. It may be observed that for the circumference centered in (730,410) the scaling is not fully applied, but for the (110,350) circumference the power law is confirmed.
By summarizing, a clear power-law scaling is observed when the network has few potential supernodes and a lot of moderately connected nodes, as shown with evidence in figure 4.81. On the contrary, when the degree centrality is high and the number of supernodes is huge, the power-law scaling is almost absent, as reported in figure 4.85. We recall that the presence of a power-law scaling of the degree centrality is a further demonstration that the spatial regions individuated by the different circumferences analyzed have all the features of real networks.

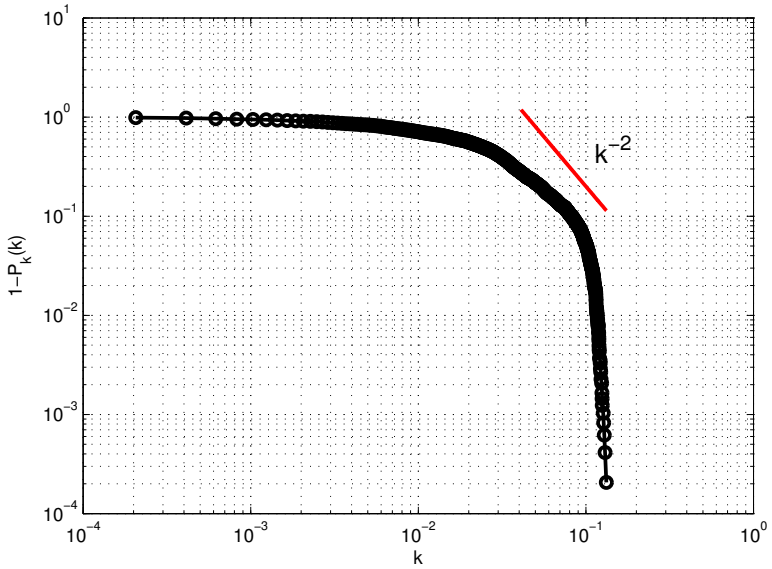

Figure 4.80: Degree centrality distribution for the circumference centered in (280,280) at $z = 512$, $\tau = 0.9$

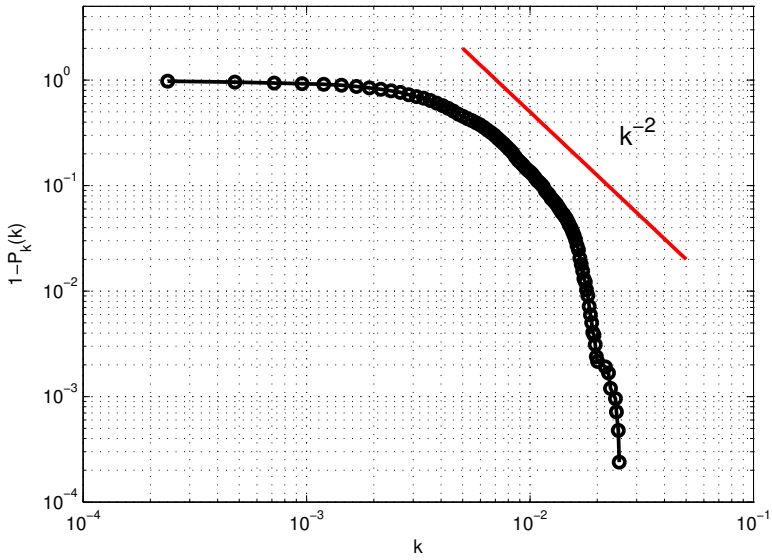

Figure 4.81: Degree centrality distribution for the circumference centered in (150,230) at $z = 512$, $\tau = 0.9$

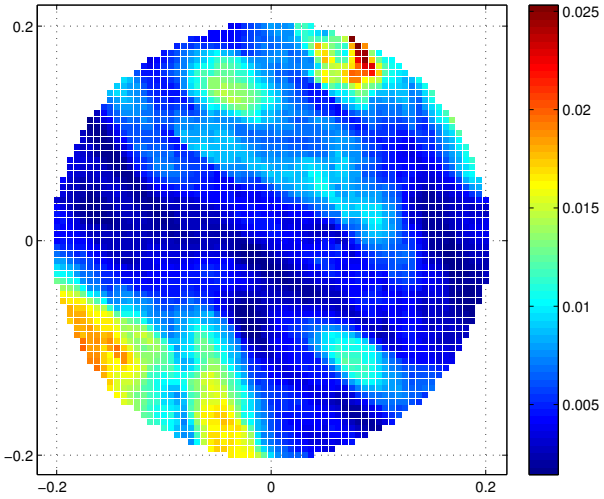

Figure 4.82: Degree centrality of the circumference centered in (150,230) at $z = 512$, $\tau = 0.9$.

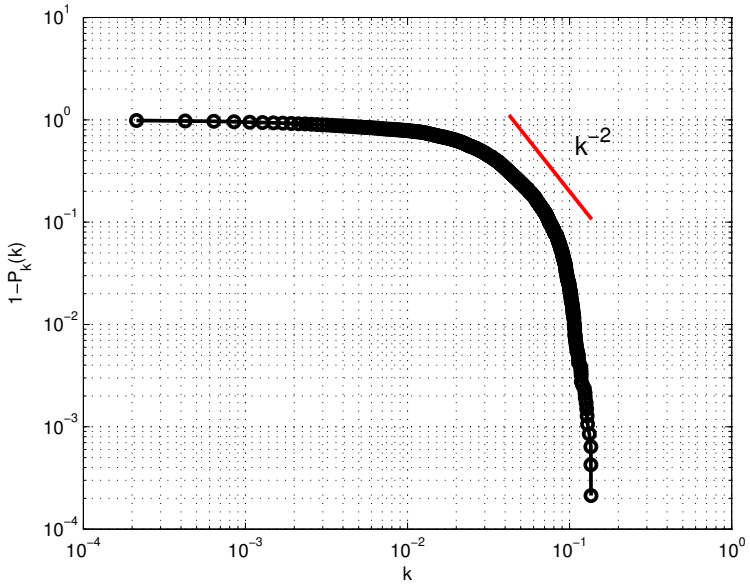

Figure 4.83: Degree centrality distribution for the circumference centered in (110,350) at $z = 212$, $\tau = 0.9$

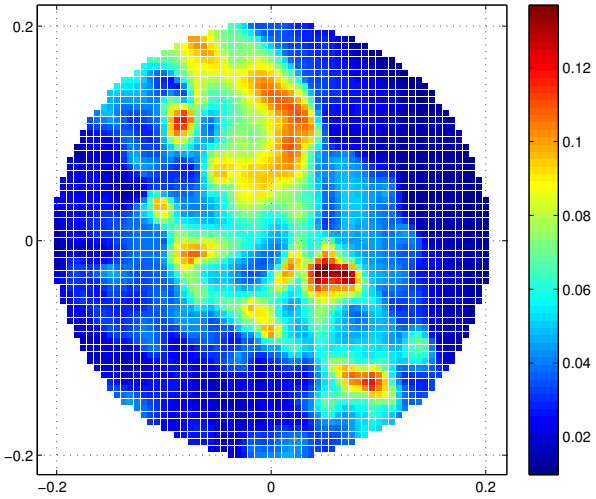

Figure 4.84: Degree centrality of the circumference centered in (110,350) at $z = 212$, $\tau = 0.9$.

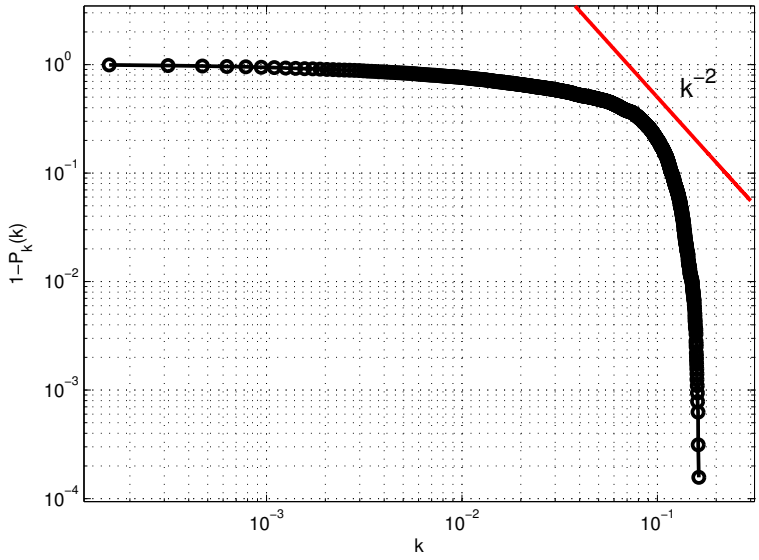

Figure 4.85: Degree centrality distribution for the circumference centered in (730,410) at $z = 212$, $\tau = 0.9$

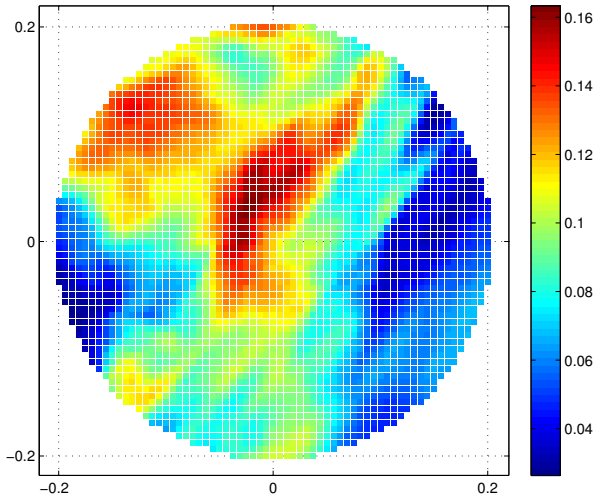

Figure 4.86: Degree centrality of the circumference centered in (730,410) at $z = 212$, $\tau = 0.9$.

Chapter 5

Conclusions

This work was divided into two parts; the first one, useful to test the consistency of the chosen database with the Kolmogorov hypotheses, confirmed the isotropic behavior of the field while providing also a good validation of the chosen dataset. Thanks to the tools of the standard dynamics of turbulence, we gained a statistical description of the flow typical of the classical approach to the problem. The second part, that was the major and the main one, helped us drawing some conclusions about the preliminary approach used in the analysis of the turbulent field. The main features achieved in this work are listed below.

First of all, part of the complex network theory's parameters chosen to analyze the behavior of the field demonstrated itself as suitable for a turbulent flow analysis: degree centrality and weighted average topological distance, in fact, may be considered as interesting means to understand the behavior of a turbulent flow and helped us in achieving a spatial characterization of the problem. On the contrary, probably due to the network extension, betweenness centrality and local clustering coefficient didn't provide as much information as thought.

We focused our analysis mainly on the degree centrality evolution, highlighting the level of correlation that a node has with its neighbors. We found several structures in the domain, different in size, shape and magnitude of the values. These structures, especially if composed of an ensemble of highly correlated nodes (i.e. supernodes), may be linked with the existence of energetic eddies: one of the main results of the theory is, in fact, the likely existence of eddies which have a lifetime longer or at least equal to the integral time-scale (which was comparable to the duration of the stored data of the DNS). In our analysis, out of circa 160 networks located in two different grids, we found at least 15-20 structures with degree centrality values ranging from 0.10 to 0.22. Every network's pattern was different from each other, hence another bright (and not expected) result of our project was that there isn't local isotropy or homogeneity, even though the flow was an isotropic and homogeneous one. Moreover, these patterns are not influenced by the forcing that acts instead on the bigger

scales. Homogeneity and isotropy were found in less correlated networks, where the range of the degree centrality values goes from 0 to 0.02. We recall, in fact, that the greater part of the analyzed networks consists of nodes which are poorly correlated to each other.
In the last part of the work we confirmed, through the power-law distribution scaling, that a turbulent field may be considered as a complex network and, legitimately, may be analyzed with the method of the complex network theory because it has all the characteristics of real networks. Eventually complex network theory can be applied to this kind of problem, because it may help to understand in a better way the complex spatial interaction between different scales (Kolmogorov's and Taylor's ones above all) in a turbulent flow, being at the same time a complementary tool of the statistical approach.
By building a network and by describing it with the complex network theory's parameters, we were able to observe the spatio-temporal characterization of emerging patterns, hence providing a richer view of what happens around a particular region. The autocorrelation and structure functions, in fact, are two-point statistics (in space, in time or both), while the complex network approach is richer because it is a multi-point statistical tool: with this study we are able to look simultaneously at the correlations between a huge number of nodes. Furthermore, thanks to the informations provided by this approach, we are able to understand phenomenologies (like the formation of spatial patterns) that the standard and simpler tools didn't provide.
We already explained how the complex network theory is still developing at fast pace, gaining (and at the same time exchanging) contributions from several fields of study. This preliminary work, due to its originality, demonstrated how a turbulence study may gain advantage from the usage of this theory. Of course, some adjustments and improvements may be done in order to fulfill a better description of a turbulent flow.
Turbulence is intrinsically three-dimensional, hence the first improvement that may be pursued is to consider a sphere instead of a circumference: a 3D network may describe in a better way what happens locally, whereas requesting more computing power.
Due to the huge number of nodes that may be contained in a turbulent network, *community structure* may be taken into account, too: a network is said to have a community structure if its nodes are grouped into subnetworks such that each set is densely connected internally (overlapping may be taken into account) [41]. The dishomogeneity of connections in a network, in fact, may suggest that there may be certain natural divisions within it.
Moreover, different types of flow may be legitimately explored thanks to the complex network theory: flows with strong dishomogeneity such as channel flow (spatial

dishomogeneity) or the Rayleigh-Bernard flow (thermal dishomogeneity) or compressible mixing layer flow (density dishomogeneity) may be taken into account, and their study may gain advantage from the field of the complex networks.

Appendix A

Codes: Pre-processing

Listing A.1 : Pre-processing

```
clc
clear all
close all

U1=zeros(800,200,1024);
V1=zeros(800,200,1024);
W1=zeros(800,200,1024);


hinfo1= hdf5info('1024timesteps/y112.h5')

for i=5:1028
a112=hdf5read(hinfo1.GroupHierarchy.Datasets(i));
for x=1:800
U1(x,1:20,i-4)=a112(1,x,:);
V1(x,1:20,i-4)=a112(2,x,:);
W1(x,1:20,i-4)=a112(3,x,:);
end
end

hinfo2= hdf5info('1024timesteps/y132.h5')
for i=5:1028
a132=hdf5read(hinfo2.GroupHierarchy.Datasets(i));
for x=1:800
U1(x,21:40,i-4)=a132(1,x,:);
V1(x,21:40,i-4)=a132(2,x,:);
W1(x,21:40,i-4)=a132(3,x,:);
end
end

```

```
hinfo3= hdf5info('1024timesteps/y152.h5')
for i=5:1028
a152=hdf5read(hinfo3.GroupHierarchy.Datasets(i));
for x=1:800
U1(x,41:60,i-4)=a152(1,x,:);
V1(x,41:60,i-4)=a152(2,x,:);
W1(x,41:60,i-4)=a152(3,x,:);
end
end

hinfo4= hdf5info('1024timesteps/y172.h5')
for i=5:1028
a172=hdf5read(hinfo4.GroupHierarchy.Datasets(i));
for x=1:800
U1(x,61:80,i-4)=a172(1,x,:);
V1(x,61:80,i-4)=a172(2,x,:);
W1(x,61:80,i-4)=a172(3,x,:);
end
end

hinfo5=hdf5info('1024timesteps/y192.h5')
for i=5:1028
a192=hdf5read(hinfo5.GroupHierarchy.Datasets(i));
for x=1:800
U1(x,81:100,i-4)=a192(1,x,:);
V1(x,81:100,i-4)=a192(2,x,:);
W1(x,81:100,i-4)=a192(3,x,:);
end
end

hinfo6=hdf5info('1024timesteps/y212.h5')
for i=5:1028
a212=hdf5read(hinfo6.GroupHierarchy.Datasets(i));
for x=1:800
U1(x,101:120,i-4)=a212(1,x,:);
V1(x,101:120,i-4)=a212(2,x,:);
W1(x,101:120,i-4)=a212(3,x,:);
end
end

hinfo7= hdf5info('1024timesteps/y232.h5')
for i=5:1028
a232=hdf5read(hinfo7.GroupHierarchy.Datasets(i));
for x=1:800
U1(x,121:140,i-4)=a232(1,x,:);
V1(x,121:140,i-4)=a232(2,x,:);
W1(x,121:140,i-4)=a232(3,x,:);
end
end
```

```
80
81 hinfo8= hdf5info('1024timesteps/y252.h5')
82 for i=5:1028
83 a252=hdf5read(hinfo8.GroupHierarchy.Datasets(i));
84 for x=1:800
85 U1(x,141:160,i-4)=a252(1,x,:);
86 V1(x,141:160,i-4)=a252(2,x,:);
87 W1(x,141:160,i-4)=a252(3,x,:);
88 end
89 end
90
91 %272-292
92 hinfo9= hdf5info('1024timesteps/y272.h5')
93 for i=5:1028
94 a272=hdf5read(hinfo9.GroupHierarchy.Datasets(i));
95 for x=1:800
96 U1(x,161:180,i-4)=a272(1,x,:);
97 V1(x,161:180,i-4)=a272(2,x,:);
98 W1(x,161:180,i-4)=a272(3,x,:);
99 end
100 end
101
102 hinfo10= hdf5info('1024timesteps/y292.h5')
103 for i=5:1028
104 a292=hdf5read(hinfo10.GroupHierarchy.Datasets(i));
105 for x=1:800
106 U1(x,181:200,i-4)=a292(1,x,:);
107 V1(x,181:200,i-4)=a292(2,x,:);
108 W1(x,181:200,i-4)=a292(3,x,:);
109 end
110 end
111
112
113 E1=0.5*U1.^2+0.5*V1.^2+0.5*W1.^2;
114 save U1_212.mat U1 -v7.3
115 save V1_212.mat V1 -v7.3
116 save W1_212.mat W1 -v7.3
117 save E1_212.mat E1 -v7.3
```

Appendix B

Codes: Network building

Listing B.1 : Correlations

```
clc
clear all
close all


load E.mat %or U.mat, V.mat, W.mat
%E.mat contains 1024 timesteps of a 200x200 grid centered around the
   point
%of interest


r_circ=0.4;
x_1=[30:170];
y_1=[30:170];
x=x_1*(2*pi/1023);
y=y_1*(2*pi/1023);
N_lato=length(x);
x0=100*(2*pi/1023);
y0=100*(2*pi/1023);
cont=0;

x_new=zeros(1,13333);
y_new=zeros(1,13333);
E_new=zeros(13333,1024);

for i=1:N_lato
   for j=1:N_lato
       if sqrt((x(i)-x0)^2 + (y(j)-y0)^2) <= r_circ
          cont=cont+1;
          x_new(cont)=x(i);
```

```
30            y_new(cont)=y(j);
31            E_new(cont,1:1024)=squeeze(E(x_1(i),y_1(j),1:1024));
32        end
33    end
34 end
35
36 R=corrcoef(E_new');
37 save R_coord.mat R x_new y_new
```

Listing B.2 : Adjacency matrix

```
1  clc
2  clear all
3  close all
4
5  load R_coord.mat
6
7  x_new
8  %%
9  M=size(R,1);
10 A=zeros(M,M);
11 %%
12 tau=0.9; %or tau=0.5
13 for i=1:M
14     for j=1:M
15         if R(i,j)>tau && i~=j && sqrt((x_new(i)-x_new(j))^2 + (y_new(i)
               -y_new(j))^2) <= 0.2
16             if  sqrt((x_new(i)-100*(2*pi/1023))^2 + (y_new(i)-100*(2*pi
                   /1023))^2) <= 0.2 | sqrt((x_new(j)-100*(2*pi/1023))^2 +
                    (y_new(j)-100*(2*pi/1023))^2) <= 0.2
17             A(i,j)=1;
18             end
19         else
20              A(i,j)=0;
21         end
22
23        end
24 end
25 %%
26 N=0;
27 for i=1:M
28     if sum(A(i,:))>0
29         N=N+1;
30         xi_new(N)=x_new(i);
31
32         yi_new(N)=y_new(i);
33     end
34 end
```

```
35
36 A(:,all(A==0,2))=[];
37 A(all(A==0,2),:)=[];
38
39 fid_x=fopen('x_new_tau_09.txt','wt');
40 fid_y=fopen('y_new_tau_09.txt','wt');
41 fid_A=fopen('A_tau_09.txt','wt');
42 for i=1:length(xi_new)
43 fprintf(fid_x,'%3.0f\n',xi_new(i)/(2*pi/1023));
44 fprintf(fid_y,'%3.0f\n',yi_new(i)/(2*pi/1023));
45 fprintf(fid_A,'%2.0f\t',A(i,:));
46 fprintf(fid_A,'\n');
47 end
48 fclose(fid_x);
49 fclose(fid_y);
50 fclose(fid_A);
```

Appendix C

Codes: Statistical tools for turbulent analysis

Listing C.1 : Second-order structure functions

```
clc
close all
clear all
load U1.mat %or V1,W1


cont=0;
for i=1:5:200
    cont=cont+1;
    for k=1:1024
        for j=1:800

            D_LL(j,cont,k)=(U1(j,i,k)-U1(1,i,k))*(U1(j,i,k)-U1(1,i,k));


        end
    end
end



load U2.mat %or V2,W2


cont=0;
for i=1:5:200
    cont=cont+1;
```

```
28      for k=1:1024
29          for j=1:800
30              D_LL(j,40+cont,k)=(U2(j,i,k)-U2(1,i,k))*(U2(j,i,k)-U2(1,i,k
                    ));
31          end
32      end
33  end
34
35
36
37  load U3.mat %or V3,W4
38
39
40  cont=0;
41  for i=1:5:200
42      cont=cont+1;
43      for k=1:1024
44          for j=1:800
45               D_LL(j,80+cont,k)=(U3(j,i,k)-U3(1,i,k))*(U3(j,i,k)-U3(1,i,
                     k));
46          end
47      end
48  end
49
50
51  load U4.mat %or V4,W4
52
53
54
55  cont=0;
56  for i=1:5:200
57      cont=cont+1;
58      for k=1:1024
59          for j=1:800
60               D_LL(j,120+cont,k)=(U4(j,i,k)-U4(1,i,k))*(U4(j,i,k)-U4(1,i
                     ,k));
61          end
62      end
63  end
64
65  D_LL_cont=mean(D_LL,2);
66  D_LL_nuova=squeeze(D_LL_cont);
67  D_LL_mediata=mean(D_LL_nuova,2);
```

Listing C.2 : Third-order structure functions

```
1  clc
2  close all
```

```
clear all
load U1.mat


cont=0;
for i=1:5:200
    cont=cont+1;
    for k=1:1024
        for j=1:800

            D_LLL(j,cont,k)=(abs(U1(j,i,k)-U1(1,i,k)))^3;


        end
    end
end

load U2.mat


cont=0;
for i=1:5:200
    cont=cont+1;
    for k=1:1024
        for j=1:800
            D_LLL(j,40+cont,k)=(abs(U2(j,i,k)-U2(1,i,k)))^3;
        end
    end
end

load U3.mat


cont=0;
for i=1:5:200
    cont=cont+1;
    for k=1:1024
        for j=1:800
             D_LLL(j,80+cont,k)=(abs(U3(j,i,k)-U3(1,i,k)))^3;
        end
    end
end


load U4.mat


cont=0;
for i=1:5:200
```

```
52      cont=cont+1;
53      for k=1:1024
54          for j=1:800
55              D_LLL(j,120+cont,k)=(abs(U4(j,i,k)-U4(1,i,k)))^3;
56          end
57      end
58  end
59
60
61  D_LLL_cont=mean(D_LLL,2);
62  D_LLL_nuova=squeeze(D_LLL_cont);
63  D_LLL_mediata=mean(D_LLL_nuova,2);
```

Listing C.3 : Transversal autocorrelation function $f(u)$ and two-point correlation function R_{11}

```
1   clc
2   close all
3   clear all
4   load U1.mat
5
6   U_U=zeros(160,800,1024);
7   U_2=zeros(160,800,1024);
8
9   cont=0;
10  for i=1:5:200
11      cont=cont+1;
12      for k=1:1024
13          for j=1:800
14
15              U_U(cont,j,k)=(U1(1,i,k)*U1(j,i,k));
16              U_2(cont,j,k)=(U1(1,i,k)^2);
17          end
18      end
19  end
20
21
22  load U2.mat
23
24
25  cont=0;
26  for i=1:5:200
27      cont=cont+1;
28      for k=1:1024
29          for j=1:800
30              U_U(40+cont,j,k)=(U2(1,i,k)*U2(j,i,k));
31              U_2(40+cont,j,k)=(U2(1,i,k)^2);
32          end
```

```
    end
end


load U3.mat

cont=0;
for i=1:5:200
    cont=cont+1;
    for k=1:1024
        for j=1:800
             U_U(80+cont,j,k)=(U3(1,i,k)*U3(j,i,k));
            U_2(80+cont,j,k)=(U3(1,i,k)^2);
        end
    end
end


load U4.mat


cont=0;
for i=1:5:200
    cont=cont+1;
    for k=1:1024
        for j=1:800
             U_U(120+cont,j,k)=(U4(1,i,k)*U4(j,i,k));
            U_2(120+cont,j,k)=(U4(1,i,k)^2);
        end
    end
end


R=mean(U_U,1);
U=mean(U_2,1);
RR=squeeze(R);
UU=squeeze(U);
f=RR./UU;
f_mediata=mean(f,2);
```

Listing C.4 : Longitudinal autocorrelation function $g(v)$

```
clc
close all
clear all
load V1.mat

U_U=zeros(160,800,1024);
```

```
7  U_2=zeros(160,800,1024);
8
9  cont=0;
10 for i=1:5:200
11     cont=cont+1;
12     for k=1:1024
13         for j=1:800
14
15             U_U(cont,j,k)=(V1(1,i,k)*V1(j,i,k));
16             U_2(cont,j,k)=(V1(1,i,k)^2);
17         end
18     end
19 end
20
21
22 load V2.mat
23
24
25 cont=0;
26 for i=1:5:200
27     cont=cont+1;
28     for k=1:1024
29         for j=1:800
30             U_U(40+cont,j,k)=(V2(1,i,k)*V2(j,i,k));
31             U_2(40+cont,j,k)=(V2(1,i,k)^2);
32         end
33     end
34 end
35
36
37 load V3.mat
38
39 cont=0;
40 for i=1:5:200
41     cont=cont+1;
42     for k=1:1024
43         for j=1:800
44              U_U(80+cont,j,k)=(V3(1,i,k)*V3(j,i,k));
45             U_2(80+cont,j,k)=(V3(1,i,k)^2);
46         end
47     end
48 end
49
50
51
52 load V4.mat
53
54
55 cont=0;
```

```
for i=1:5:200
    cont=cont+1;
    for k=1:1024
        for j=1:800
             U_U(120+cont,j,k)=(V4(1,i,k)*V4(j,i,k));
            U_2(120+cont,j,k)=(V4(1,i,k)^2);
        end
    end
end


R=mean(U_U,1);
U=mean(U_2,1);
RR=squeeze(R);
UU=squeeze(U);
f=RR./UU;
g_mediata=mean(f,2);
```

Listing C.5 : Longitudinal autocorrelation function $f(v)$

```
clc
close all
clear all
load V1.mat

U_U=zeros(160,800,1024);
U_2=zeros(160,800,1024);

cont=0;
for j=1:5:800
    cont=cont+1;
    for k=1:1024
        for i=1:200

            U_U(cont,i,k)=(V1(j,1,k)*V1(j,i,k));
            U_2(cont,i,k)=(V1(j,1,k)^2);
        end
    end
end


load V2.mat


cont=0;
for j=1:5:800
    cont=cont+1;
    for k=1:1024
```

```
29          for i=1:200
30              U_U(cont,200+i,k)=(V1(j,1,k)*V2(j,i,k));
31              U_2(cont,200+i,k)=(V1(j,1,k)^2);
32          end
33      end
34  end
35
36
37  load V3.mat
38
39
40  cont=0;
41  for j=1:5:800
42      cont=cont+1;
43      for k=1:1024
44          for i=1:200
45               U_U(cont,400+i,k)=(V1(j,1,k)*V3(j,i,k));
46              U_2(cont,400+i,k)=(V1(j,1,k)^2);
47          end
48      end
49  end
50
51
52  load V4.mat
53
54
55
56  cont=0;
57  for j=1:5:800
58      cont=cont+1;
59      for k=1:1024
60          for i=1:200
61               U_U(cont,600+i,k)=(V1(j,1,k)*V4(j,i,k));
62              U_2(cont,600+i,k)=(V1(j,1,k)^2);
63          end
64      end
65  end
66
67
68  R=mean(U_U,1);
69  U=mean(U_2,1);
70  RR=squeeze(R);
71  UU=squeeze(U);
72  f=RR./UU;
73  f_mediata=mean(f,2);
```

Listing C.6 : Transversal autocorrelation function $g(u)$

```
clc
close all
clear all
load U1.mat

U_U=zeros(160,800,1024);
U_2=zeros(160,800,1024);

cont=0;
for j=1:5:800
    cont=cont+1;
    for k=1:1024
        for i=1:200

            U_U(cont,i,k)=(U1(j,1,k)*U1(j,i,k));
            U_2(cont,i,k)=(U1(j,1,k)^2);
        end
    end
end


load U2.mat


cont=0;
for j=1:5:800
    cont=cont+1;
    for k=1:1024
        for i=1:200
            U_U(cont,200+i,k)=(U1(j,1,k)*U2(j,i,k));
            U_2(cont,200+i,k)=(U1(j,1,k)^2);
        end
    end
end


load U3.mat


cont=0;
for j=1:5:800
    cont=cont+1;
    for k=1:1024
        for i=1:200
             U_U(cont,400+i,k)=(U1(j,1,k)*U3(j,i,k));
            U_2(cont,400+i,k)=(U1(j,1,k)^2);
        end
    end
end
```

```
50
51
52 load U4.mat
53
54
55 cont=0;
56 for j=1:5:800
57     cont=cont+1;
58     for k=1:1024
59         for i=1:200
60              U_U(cont,600+i,k)=(U1(j,1,k)*U4(j,i,k));
61             U_2(cont,600+i,k)=(U1(j,1,k)^2);
62         end
63     end
64 end
65
66
67 R=mean(U_U,1);
68 U=mean(U_2,1);
69 RR=squeeze(R);
70 UU=squeeze(U);
71 f=RR./UU;
72 g_mediata=mean(f,2);
```

Listing C.7 : Transversal autocorrelation function $g(u)$ (or $g_(v)$) derived from the derivative definition in eq. 1.26

```
1 clc
2 clear all
3 close all
4
5 load f_u.mat %or f_v.mat, it contains the data from the longitudinal
     autocorrelation function.
6
7 N=[1:1:800];
8 r=N*0.00611;
9 g(1)=1;
10 for i=2:length(N)-1
11 g(i)=f_mediata(i)+0.5*r(i)*(f_mediata(i+1)-f_mediata(i-1))/(r(i+1)-r(i
     -1))
12 end
```

Listing C.8 : One-dimensional spectra

```
1 clc
2 clear all
```

```
3  close all
4
5
6  L = 800;  % Length of signal
7  dx = 0.0061;
8  r = (0:L-1)*dx; % Spatial vector
9  ks = 2*pi/dx; % Sample space
10 cont=0;
11
12 load V1.mat %or U1.mat
13
14
15 cont=0;
16 pwr = zeros(1,L);
17 der_v= zeros(1,L-2);
18
19
20 for j=1:2:200
21    for k=1:1024
22        cont=cont+1;
23        [Fou,kappa] = centeredFFT1D(V1(:,j,k).',ks);
24        power = abs(Fou.*conj(Fou)/L);
25        derivative = (power(3:end)-power(1:end-2))./(kappa(3:end)-kappa
              (1:end-2));
26        der_v = der_v + derivative;
27        pwr = pwr + abs(power);
28    end
29
30 end
31
32 load V2.mat  %or U2.mat
33
34
35
36 for j=1:2:200
37    for k=1:1024
38        cont=cont+1;
39        [Fou,kappa] = centeredFFT1D(V2(:,j,k).',ks);
40        power = abs(Fou.*conj(Fou)/L);
41        derivative = (power(3:end)-power(1:end-2))./(kappa(3:end)-kappa
              (1:end-2));
42        der_v = der_v + derivative;
43        pwr = pwr + abs(power);
44    end
45
46 end
47
48
49
```

```
load V3.mat  %or U3.mat


for j=1:2:200
   for k=1:1024
       cont=cont+1;
       [Fou,kappa] = centeredFFT1D(V3(:,j,k).',ks);
       power = abs(Fou.*conj(Fou)/L);
       derivative = (power(3:end)-power(1:end-2))./(kappa(3:end)-kappa
           (1:end-2));
       der_v = der_v + derivative;
       pwr = pwr + abs(power);
   end

end



load V4.mat  %or U4.mat


for j=1:2:200
   for k=1:1024
       cont=cont+1;
       [Fou,kappa] = centeredFFT1D(V4(:,j,k).',ks);
       power = abs(Fou.*conj(Fou)/L);
       derivative = (power(3:end)-power(1:end-2))./(kappa(3:end)-kappa
           (1:end-2));
       der_v = der_v + derivative;
       pwr = pwr + abs(power);
   end

end

pwr = pwr/cont;
kappa_V=kappa;
save spectrum1D_V der_v kappa_V cont -v7.3
```

Listing C.9 : Three-dimensional spectrum

```
clc
clear all
close all

load spectrum1D_V.mat
load spectrum1D_U.mat %These files contain the 1D spectrum for  U and V
```

```
7 kappa=kappa_U;
8 E_3D = -0.5*kappa(2:end-1).*(der_u+der_v)/cont;
```

Appendix D

Codes: A complex network analysis

Listing D.1 : Degree centrality

```
clc
close all
clear all

x_new_tau_09=load('x_new_tau_09.txt');
y_new_tau_09=load('y_new_tau_09.txt');
A_tau_09=load('A_tau_09.txt');
x_09=((2*pi)/1023)*x_new_tau_09;
y_09=((2*pi)/1023)*y_new_tau_09;

p=length(x_new_tau_09)
for k=1:p
    dc(k)=sum(A_tau_09(k,:));
end
dc=dc.';
dc=dc./(p-1);
```

Listing D.2 : Weighted average topological distance

```
clc
clear all
close all

x_new_tau_09=load('x_new_tau_09.txt');
y_new_tau_09=load('y_new_tau_09.txt');
A_tau_09=load('A_tau_09.txt');
```

```
p09=size(A_tau_09,1);
A09=sparse(A_tau_09);

for i=1:p09
    d(:,i)=shortest_paths(A09,i); %this is a customed function for the
        computation of the shortest paths
end
d=d.';
cont=zeros(1,p09);
for i=1:p09
    for j=1:p09
        if isinf(d(i,j))==0 && i~=j
            d_new(i,j)=d(i,j);
            cont(i)=cont(i)+1;
        end
    end
    cc(i)=(sum(d_new(i,:)))/(cont(i))*(p09-1)/(cont(i));
end
cc=cc.';
```

Listing D.3 : Betweenness centrality

```
clear all
close all
x_new_tau_09=load('x_new_tau_09.txt');
y_new_tau_09=load('y_new_tau_09.txt');
A_tau_09=load('A_tau_09.txt');
p09=size(A_tau_09,1);
A09=sparse(A_tau_09);
bet_cen09 = betweenness_centrality(A09); %this is a custom function to
    calculate the betweenness centrality
z_m=bet_cen09;
c = log(z_m+1);
x_09=x_new_tau_09*(2*pi/1023);
y_09=y_new_tau_09*(2*pi/1023);
```

Listing D.4 : Local clustering coefficient

```
clc
clear all
close all

x_new_tau_09=load('x_new_tau_09.txt');
y_new_tau_09=load('y_new_tau_09.txt');
A_tau_09=load('A_tau_09.txt');
p09=size(A_tau_09,1);
```

```
9  A09=sparse(A_tau_09);
10 loc_cl_coef = clustering_coefficients(A09); %this is a custom function
       to calculate the clustering coefficient
11 glo_cl_coef=mean(loc_cl_coef);
```

Bibliography

[1] Richardson L.F. *Weather Prediction by Numerical Process*, pages 183–233. Cambridge University Press, 1922.

[2] Stephen B. Pope. *Turbulent Flows*, pages 183–233. Cambridge University Press, 2000.

[3] Romano G.P. and Antonia R.A. Longitudinal and transverse structure functions in a turbulent round jet: effect of initial conditions and reynolds number. *Journal of Fluid Mechanics*, 436:231–248, 2001.

[4] Fukayama D., Oyamada T., Nakano T., Gotoh T., and Yamamoto K. Longitudinal structure functions in decaying and forced turbulence. 2000.

[5] Saddoughi S. G. and Veeravalli S. V. Local isotropy in turbulent boundary layers at high reynolds number. *Journal of Fluid Mechanics*, 268:333–372, 1994.

[6] Comte-Bellot G. and Corrsin S. Simple eulerian time correlation of full and narrow-band velocity signals in grid-generated 'isotropic' turbulence. *Journal of Fluid Mechanics*, 48:273–337, 1971.

[7] Townsend A.A. *The structure of turbulent shear flow*, pages 1–28. Cambridge University Press, 1980.

[8] Moin P. and Mahesh K. Direct numerical simulation: a tool in turbulence research. *Annual Review of Fluid Mechanics*, 30:539–578, 1998.

[9] Ishihara T, Gotoh T., and Kaneda Y. Study of high-reynolds number isotropic turbulence by direct numerical simulation. *Annual Review of Fluid Mechanics*, 41:165–180, 2009.

[10] Orszag S. A. and Patterson Jr G. S. Numerical simulation of three-dimensional homogeneous isotropic turbulence. *Physical Review Letters*, 28, 1972.

[11] Germano M., Piomelli U., Moin P., and Cabot W. H. A dynamic subgrid scale eddy viscosity model. *Physics of Fluids A*, 3:2323–2324, 1991.

[12] Johns hopkins turbulence databases. `http://turbulence.pha.jhu.edu`. [Online; accessed 1-July-2014].

[13] Li Y., Perlman E., Wan M., Yan. Y, Meneveau C., Burns R., Chen S., Szalay A., and Eyink G. A public turbulence database cluster and applications to study lagrangian evolution of velocity increments in turbulence. *Journal of Turbulence*, 9(31), 2008.

[14] Gungor A.G. and Mengon S. A new two-scale model for large eddy simulation of wall-bounded flows. *Progress in Aerospace Sciences*, 46, 2010.

[15] Yu H. and Meneveau C. Scaling of conditional lagrangian time correlation functions of velocity and pressure gradient magnitudes in isotropic turbulence. *Flow, Turbulence and Combustion*, 85:457–472, 2010.

[16] Wu C.C. and Chang T. Rank-ordered multifractal analysis (roma) of probability distributions in fluid turbulence. *Nonlin. Processes Geophys.*, 18, 2011.

[17] Strogatz S. H. Exploring complex networks. *Nature*, 410(6825):268–276.

[18] Albert R and Barabási A.-L. Statistical mechanics of complex networks. *Reviews of Modern Physics*, 74:47–97.

[19] Boccaletti S., Latora V., Moreno Y., Chavez M., and Hwang D.-U. Complex networks: Structure and dynamics. *Physics Reports*, 424:175–308, 2006.

[20] Costa L. da F., Rodrigues F. A., Travieso G., and Villas Boas P. R. Characterization of complex networks: A survey of measurements. *Advances in Physics*, 56(1):167–242, 2007.

[21] Costa L. da F., Oliveira Jr. O. N., Travieso G., Rodrigues F. A., Villas Boas P. R., Antiqueira L., Viana M. P., and Correa Rocha L. E. Analyzing and modeling real-world phenomena with complex networks: a survey of applications. *Advances in Physics*, 60(3):329–412, 2011.

[22] Milgram S. The small world problem. *Psychology Today*, 2, 1967.

[23] Park J. and Newman M. E. J. A network-based ranking system for american college football. *Journal of Statistical Mechanics*, 10, 2005.

[24] Davis K.F., D'Odorico P., Laio F., and Ridolfi L. Global spatio-temporal patterns in human migration: a complex network perspective. *Plos One*, 8(1), 2013.

[25] Will U.K., Nemon N., and Karampelas P. Detecting new trends in terrorist networks. *International Conference on Advances in Social Network Analysis, Odense*, 2010.

[26] Zou C. C. and Gong D. W. In *Proceedings of the 13th International Conference on Computer Communications and Networks*, pages 409–414, 2004.

[27] Berners-Lee T., Hall W., Hendler J., Shadbolt N., and Weitzner D. Creating a science of the web. *Science*, 312, 2006.

[28] Barabási A.L. and Oltvai Z. N. Network biology: understanding the cell's functional organization. *Nature Reviews Genetics*, 5, 2004.

[29] Lee D. S., Park J., Kay K. A., Christakis N. A., Oltvai Z. N., and Barabási A. L. The implications of human metabolic network topology for disease comorbidity. *Proceedings of the National Academy of Sciences*, 105, 2008.

[30] Chen L. L., Blumm N., Christakis N. A., Barabási A. L., and Deisboeck T. S. Cancer metastasis networks and the prediction of progression patterns. *Brit J Cancer*, 2009.

[31] Souma W., Fujiwara Y., and Aoyama H. Small-world effects in wealth distribution. *Preprint arXiv:cond-mat/0108482*, 2001.

[32] Serrano M.A. and Boguná M. Topology of the world trade web. *Physical Review*, 68(1), 2003.

[33] Onnela J. P., Chakraborti A., Kaski K., Kertesx J, and Kanto A. Dynamics of market correlations: Taxonomy and portfolio analysis. *Physical Review*, 68(5), 2003.

[34] Abe S. and Suzuki N. Complex-network description of seismicity. *Nonlin. Processes Geophys.*, 13:145–150, 2006.

[35] Scarsoglio S., Laio F., and Ridolfi L. Climate dynamics: A network-based approach for the analysis of global precipitation. *Plos One*, 8(8), 2013.

[36] Donges J. F., Zou Y., Marwan N., and Kurths J. Complex networks in climate dynamics. *European Physical Journal, Special Topics*, 174:157–179, 2009.

[37] Kim D.-H. and Motter A. E. Fluctuation-driven capacity distribution in complex networks. *New Journal of Physics*, 10, 2008.

[38] Donges J.J., Zou Y., Marwan N., and Kurths J. Complex networks in climate dynamics. *Eur Physics Journal Special Topics*, 174:157–179, 2009.

[39] Donges J.J., Zou Y., Marwan N., and Kurths J. The backbone of the climate network. *Europhysics Lettures*, 87, 2009.

[40] Albert R and Barabási A.-L. Emergence of scaling in random networks. *Science*, 286:509–512, 1999.

[41] Girvan M. and Newman M. E. J. Community structure in social and biological networks. *Proc. Natl. Acad. Sci. USA*, 99(12):7821–7826, 2002.